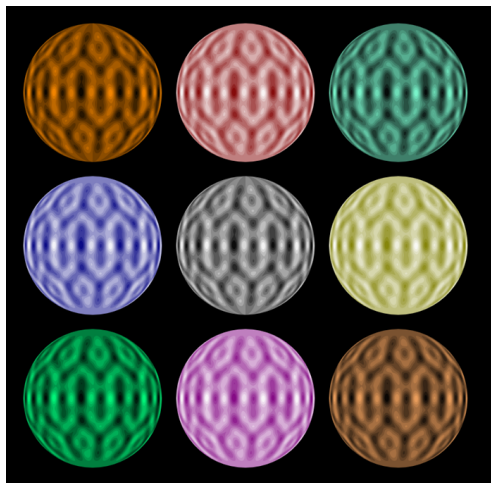


# Explaining mixed Rossby-gravity wave generation in the tropical atmosphere

Dissertation

with the aim of achieving a doctoral degree  
at the Faculty of Mathematics, Informatics and Natural Sciences  
Department of Earth System Sciences  
at University of Hamburg



submitted by

Sándor István Mahó  
*from Budapest*

Hamburg, 2024

## Department of Earth Sciences

Date of Oral Defense: 30.01.2025

Reviewers: Prof. Dr. Nedjeljka Žagar

Dr. Sergiy Vasylkevych

Members of the examination commission: Prof. Dr. Nedjeljka Žagar

Dr. Sergiy Vasylkevych

Prof. Dr. Eleanor Frajka-Williams

Prof. Dr. Riwal Plougonven

Prof. Dr. Jörn Behrens

Chair of the Subject Doctoral Committee  
Earth System Sciences:

Prof. Dr. Hermann Held

Dean of Faculty MIN:

Prof. Dr.-Ing. Norbert Ritter

## **Eidesstattliche Versicherung | Declaration on oath**

Hiermit erkläre ich an Eides statt, dass ich die vorliegende Dissertationsschrift selbst verfasst und keine anderen als die angegebenen Quellen und Hilfsmittel benutzt habe. Sofern im Zuge der Erstellung der vorliegenden Dissertationsschrift generative Künstliche Intelligenz (gKI) basierte elektronische Hilfsmittel verwendet wurden, versichere ich, dass meine eigene Leistung im Vordergrund stand und dass eine vollständige Dokumentation aller verwendeten Hilfsmittel gemäß der Guten wissenschaftlichen Praxis vorliegt. Ich trage die Verantwortung für eventuell durch die gKI generierte fehlerhafte oder verzerrte Inhalte, fehlerhafte Referenzen, Verstöße gegen das Datenschutz- und Urheberrecht oder Plagiate. Ich versichere, dass dieses gebundene Exemplar der Dissertation und das in elektronischer Form eingereichte Dissertationsexemplar (über den Docata-Upload) und das bei der Fakultät (zuständiges Studienbüro bzw. Promotionsbüro Physik) zur Archivierung eingereichte gedruckte gebundene Exemplar der Dissertationsschrift identisch sind.

I hereby declare and affirm that this doctoral dissertation is my own work and that I have not used any aids and sources other than those indicated. If electronic resources based on generative artificial intelligence (gAI) were used in the course of writing this dissertation, I confirm that my own work was the main and value-adding contribution and that complete documentation of all resources used is available in accordance with good scientific practice. I am responsible for any erroneous or distorted content, incorrect references, violations of data protection and copyright law or plagiarism that may have been generated by the gAI. I, the undersigned, declare that this bound copy of the dissertation and the dissertation submitted in electronic form (via the Docata upload) and the printed bound copy of the dissertation submitted to the faculty (responsible Academic Office or the Doctoral Office Physics) for archiving are identical.

Ort, den | City, date                      Unterschrift | Signature

## ABSTRACT

The tropics play an important role in the atmospheric general circulation and predictability. Equatorial waves, including mixed Rossby-gravity (MRG) waves contribute to the day-to-day variability of the tropical atmosphere, thereby influencing the weather both within the tropics, and in the extratropics through atmospheric teleconnections. Several observational studies provide evidence about the role of MRG waves in tropospheric and middle atmospheric variability.

Although the effect of asymmetric convection is well-known for generating MRG waves, it does not explain the observed MRG waves in the troposphere. Other excitation mechanisms also fail to adequately explain the synoptic-scale and the planetary-scale MRG waves in the upper troposphere and the upper stratosphere, respectively. Therefore, this thesis proposes a new excitation mechanism for MRG waves: wave-mean flow interactions.

This mechanism is detected by idealised simulations with a simple atmospheric model, TIGAR, which solves the nonlinear rotating shallow water equations on the sphere by a spectral method that uses Hough harmonics as spectral basis functions. This modelling framework allows the direct diagnosis of MRG waves from the model output and has an advantage over  $\beta$ -plane shallow water models because, on the sphere, MRG waves are global and their meridional e-folding scale depends on the zonal wavenumber, which is crucial for the proposed MRG wave generation process.

The wave-mean flow interactions require an asymmetric background flow, which determines the amplitude of the excited MRG waves. Specifically, the greater the asymmetry of the background state (i.e., the energy in asymmetric Hough mean state modes), the more energetic the excited MRG waves become. It is also shown that wave-wave interactions are irrelevant for the MRG wave excitation relative to wave-mean flow interactions and direct wave excitation by a tropical heat source. The wave-mean flow interactions are hypothesized to involve waves generated locally by tropical heating perturbations in the upper troposphere, while in the upper stratosphere, vertically propagating internal waves or waves generated by shear instabilities may be important contributors. The scale selection of MRG waves through wave-mean flow interactions is driven by the jet location: the closer the jet to the equator, the smaller the MRG waves. This means that hemispheric jets in the middle atmosphere excite large-scale MRG waves, whereas upper tropospheric subtropical jets support the generation of synoptic-scale MRG waves. This theory is supported by jet positions derived from ERA5 data. The decisive role of the jet location in the scale selection arises from the meridional extent of spherical MRG waves, which depend on both the zonal wavenumber and the shallow water mean depth. As small-scale (i.e. large zonal wavenumber) spherical MRG waves are meridionally more bounded to the equator, they cannot be excited by the middle atmospheric jets embedded in the extratropics, since these

waves would be “invisible” to the interactions. This behaviour is completely missing for  $\beta$ -plane MRG waves. Since most studies on MRG wave excitation have used  $\beta$ -plane solutions, this explains why the scale selection process has remained elusive in the literature for so long.

As an additional factor in the MRG wave generation, this thesis examines wave growth induced by barotropic instability in the region of the quasi-biennial oscillation (QBO). While previous studies suggest a connection between the barotropic instability of the QBO and MRG waves, a long-term analysis of this process using real data is lacking. This thesis proposes that MRG wave energy greatly intensify following barotropic instability development of equatorial jets, mimicking the QBO-related circulation. Furthermore, it is also shown that MRG wave growth is enhanced during the westerly phase of the QBO, driven by two factors. First, the potential for barotropic instability in the westerly QBO phase is twice as large as in the easterly phase. Second, the unstable background eigenmodes of the westerly phase contain significantly more MRG waves. This likely leads to stronger MRG wave growth at synoptic and subsynoptic scales during the westerly phase, which aligns with observations of MRG wave kinetic energy in the QBO region.

Overall, this thesis proposes that wave-mean flow interactions and barotropic instability-induced wave growth play a significant role in MRG wave generation in the real atmosphere, with important implications for atmospheric predictability.

## ZUSAMMENFASSUNG

Die Tropen spielen eine wichtige Rolle in der allgemeinen atmosphärischen Zirkulation und der Vorhersagbarkeit. Äquatoriale Wellen, einschließlich gemischter Rossby-Schwere (MRG) Wellen, tragen zur täglichen Variabilität der tropischen Atmosphäre bei und beeinflussen dadurch sowohl das Wetter in den Tropen als auch in den Extratropen durch atmosphärische Telekonnektionen. Mehrere Beobachtungsstudien liefern Hinweise auf die Rolle von MRG-Wellen in der Variabilität der Troposphäre und der mittleren Atmosphäre.

Obwohl der Einfluss asymmetrischer Konvektion auf die Erzeugung von MRG-Wellen bekannt ist, erklärt er nicht die beobachteten MRG-Wellen in der Troposphäre. Andere Anregungsmechanismen erklären ebenfalls nicht ausreichend die synoptischen und planetaren MRG-Wellen in der oberen Troposphäre bzw. der oberen Stratosphäre. Daher schlägt diese Arbeit einen neuen Anregungsmechanismus für MRG-Wellen vor: Wellen-Grundstrom-Wechselwirkungen.

Dieser Mechanismus wird durch idealisierte Simulationen mit einem einfachen atmosphärischen Modell, TIGAR, nachgewiesen, das die nichtlinearen, rotierenden Flachwasser-Gleichungen auf der Kugel durch ein Spektralverfahren löst, das Hough-harmonics als spektrale Basisfunktionen verwendet. Dieses Modellierungsframework ermöglicht die Diagnose von MRG-Wellen direkt aus den Modellergebnissen und hat einen Vorteil gegenüber Flachwasser-Modellen auf der  $\beta$ -Ebene, da MRG-Wellen auf der Kugel global sind und ihre meridionale Ausdehnung von der zonalen Wellenzahl abhängt, was für den vorgeschlagenen Erzeugungsprozess der MRG-Wellen entscheidend ist.

Die Wellen-Grundstrom-Wechselwirkungen erfordern einen asymmetrischen Grundstrom, der die Amplitude der angeregten MRG-Wellen bestimmt. Konkret gilt: Je größer die Asymmetrie des Grundzustands (d.h. die Energie in asymmetrischen Hough-Grundstrommoden), desto energiereicher werden die angeregten MRG-Wellen. Es wird auch gezeigt, dass Wellen-Wellen-Wechselwirkungen im Vergleich zu Wellen-Grundstrom-Wechselwirkungen und direkter Wellenanregung durch eine tropische Wärmequelle irrelevant für die Anregung von MRG-Wellen sind. Es wird angenommen, dass die Wellen-Grundstrom-Wechselwirkungen Wellen umfassen, die lokal durch tropische Wärmestörungen in der oberen Troposphäre erzeugt werden, während in der oberen Stratosphäre vertikal propagierende interne Wellen oder Wellen, die durch Scherinstabilitäten erzeugt werden, wichtige Beiträge leisten könnten. Die Skalenauswahl der MRG-Wellen durch Wellen-Grundstrom-Wechselwirkungen wird durch die Lage des Jets bestimmt: Je näher der Jet am Äquator liegt, desto kleiner werden die MRG-Wellen. Dies bedeutet, dass Jets auf einer Halbkugel in der mittleren Atmosphäre großskalige MRG-Wellen anregen, während subtropische Jets in der oberen Troposphäre die Erzeugung von MRG-Wellen auf der synoptischen Skala unterstützen. Diese Theorie wird durch Jet-Positionen gestützt, die aus

ERA5-Daten abgeleitet wurden. Die entscheidende Rolle der Jet-Position bei der Skalenauswahl ergibt sich aus der meridionalen Ausdehnung sphärischer MRG-Wellen, die sowohl von der zonalen Wellenzahl als auch von der mittleren Flachwassertiefe abhängen. Da kleinskalige (d.h. große zonale Wellenzahl) sphärische MRG-Wellen meridional stärker an den Äquator gebunden sind, können sie nicht von den Jets der mittleren Atmosphäre, die sich in den Extratropen befinden, angeregt werden, da diese Wellen für die Interaktionen “unsichtbar” wären. Dieses Verhalten fehlt vollständig bei MRG-Wellen auf der  $\beta$ -Ebene. Da die meisten Studien zur Anregung von MRG-Wellen  $\beta$ -Ebenen-Lösungen verwendet haben, erklärt dies, warum der Skalenauswahlprozess in der Literatur so lange unklar geblieben ist.

Als zusätzlicher Faktor für die MRG-Wellen-Erzeugung untersucht diese Arbeit das Wellenwachstum, das durch barotrope Instabilität in der Region der quasi-biennalen Oszillation (QBO) induziert wird. Während frühere Studien eine Verbindung zwischen der barotropen Instabilität der QBO und MRG-Wellen vermuten, fehlt eine langfristige Analyse dieses Prozesses unter Verwendung von Realdaten. Diese Arbeit schlägt vor, dass die Energie der MRG-Wellen nach der Entwicklung der barotropen Instabilität der äquatorialen Jets, die die QBO-bezogene Zirkulation nachahmen, stark zunimmt. Es wird auch gezeigt, dass das MRG-Wellenwachstum während der Westwindphase der QBO durch zwei Faktoren verstärkt wird. Erstens ist das Potenzial für barotrope Instabilität in der Westwindphase der QBO doppelt so groß wie in der Ostwindphase. Zweitens enthalten die instabilen Grundstrom-Eigenmoden der Westwindphase signifikant mehr MRG-Wellen. Dies führt wahrscheinlich zu einem stärkeren MRG-Wellenwachstum auf der synoptischen und subsynoptischen Skala während der Westwindphase, was mit Beobachtungen der kinetischen Energie von MRG-Wellen in der QBO-Region übereinstimmt.

Insgesamt schlägt diese Arbeit vor, dass Wellen-Grundstrom-Wechselwirkungen und durch barotrope Instabilität induziertes Wellenwachstum eine bedeutende Rolle bei der MRG-Wellen-Erzeugung in der realen Atmosphäre spielen, mit wichtigen Auswirkungen auf die atmosphärische Vorhersagbarkeit.

## DECLARATION OF AUTHORSHIP

### Publications and pre-publications related to the present dissertation

Mahó, S.I., Vasylykevych, S. & Žagar, N. (2024) Excitation of mixed Rossby–gravity waves by wave–mean flow interactions on the sphere. *Quarterly Journal of the Royal Meteorological Society*, 150(762), 2920–2936. Available from: <https://doi.org/10.1002/qj.4742>

Mahó, S.I., Žagar, N., Lunkeit, F. & Vasylykevych, S. (2024) The mechanism of scale selection for mixed Rossby-gravity waves in the upper troposphere and the upper stratosphere. *Geophysical Research Letters*, under revision.

Mahó, S.I., Lunkeit, F., Žagar, N. & Vasylykevych, S. (2024) The effect of barotropic instability on mixed Rossby-gravity wave variability during the QBO phases. *To be submitted to Weather and Climate Dynamics*.

Title page graphics by Sándor István Mahó:  
*Harmonic waves generated by the TIGAR model*

## EPIGRAPH

I would like to tell the youth about the beauty of becoming researchers. I find myself now in spotlight, but if you like limelight, you should rather become actors because a research career probably won't offer that. And if you want to become rich and make a lot of money, I do not know what you should do. But if you want your life to be delightful and a feeling that you did something for others, then you should become researchers. People may not know you by name, but you will always know that you did something good for the others.

*Katalin Karikó, 21st century Nobel laureate*

## TABLE OF CONTENTS

Abstract .....	iv
Zusammenfassung .....	vi
Declaration of authorship .....	viii
Epigraph .....	ix
Table of Contents .....	x
Acknowledgements .....	xii
Chapter 1 Introduction .....	1
1.1 Fundamentals of the tropical atmospheric circulation .....	1
1.2 Theory and identification of equatorial waves .....	2
1.3 Role of mixed Rossby-gravity waves in shaping tropical dynamics .....	6
1.4 Observations of MRG waves in the equatorial atmosphere .....	7
1.5 Generation theories for MRG waves .....	10
1.6 On the connection between barotropic instability and MRG wave growth in the QBO region .....	12
Chapter 2 Numerical modelling of MRG wave generation .....	15
Chapter 3 Generation and growth of MRG waves in the equatorial troposphere and stratosphere .....	18
3.1 Excitation of MRG waves by wave-mean flow interactions .....	19
3.1.1 Numerical simulations for detecting MRG wave generation .....	19
3.1.2 Wave-mean flow interactions as MRG wave generation .....	21
3.2 Scale separation of upper tropospheric and upper stratospheric MRG waves by wave-mean flow interactions .....	29
3.2.1 MRG wave scale selection in simulations representative of the upper troposphere and the upper stratosphere .....	29
3.2.2 The flow parameter driving the MRG wave scale selection .....	32
3.3 Role of barotropic instability in the growth of mixed Rossby-gravity waves in the stratosphere .....	35
3.3.1 Barotropic instability potential during the QBO phases .....	35
3.3.2 Sensitivity of MRG wave growth to barotropic instability in idealised simulations .....	37
3.3.3 Unstable modes and MRG wave growth in the QBO region .....	39
Chapter 4 Conclusions and outlook .....	43

Appendix A: Excitation of mixed Rossby-gravity waves by wave - mean flow interactions on the sphere .....	46
A1 Introduction .....	48
A2 Numerical model formulation and setup .....	49
A2.1 The non-linear TIGAR model .....	49
A2.2 The linearized model .....	52
A2.3 Energy diagnostics in modal space .....	53
A2.4 Setup of numerical experiments .....	55
A2.5 Sensitivity of MRGWs excited by external forcing to modelling setup ..	58
A3 Excitation of MRGWs by wave-mean flow interactions .....	59
A4 Excitation of MRGWs in simulations with realistic background flow .....	64
A5 Discussion and Conclusions .....	67
A6 Acknowledgements .....	70
A7 Conflict of interest .....	70
A8 Supplements .....	70
A8.1 Numerical aspects of TIGAR .....	70
A8.2 Formulation of geostrophic zonal steady states on the sphere .....	72
 Appendix B: The mechanism of scale selection for mixed Rossby-gravity waves in the upper troposphere and the upper stratosphere .....	 74
B9 Introduction .....	76
B10 MRG wave scale selection in simulations with realistic zonal wind profiles ....	78
B11 Sensitivity of the MRG scale selection to the jet central latitude .....	80
B12 Discussion and Conclusions .....	81
B13 Open research .....	83
B14 Acknowledgements .....	83
B15 Supplements .....	83
B15.1 Computation of the seasonal climatology of the mixed Rossby-gravity wave energy spectra .....	83
B15.2 Details of the experimental setup .....	85
B15.3 MRG wave energy tendencies in the TROPO and STRATO simulations	88
B15.4 Further aspects of the MRG wave scale selection in relation to the zonal jet position .....	89
B15.5 Determination of the jet position from zonally-averaged zonal wind data	90
 Appendix C: The effect of barotropic instability on mixed Rossby-gravity wave variability during the QBO phases .....	 92
C16 Introduction .....	94
C17 Data and numerical modelling .....	96
C17.1 Idealised barotropic instability simulations .....	96
C17.2 ERA5 zonal wind data .....	98
C17.3 Determining unstable background eigenmodes .....	99
C18 Results .....	101

C18.1	MRG wave intensification by barotropic instability in idealised simulations	101
C18.2	Instability of the QBO region .....	102
C18.3	Barotropically unstable modes of the system linearized around the 30 hPa zonal mean flow .....	103
C19	Discussion and summary .....	107
C20	Supplement.....	111
C21	Acknowledgements .....	112
Bibliography .....		113

## ACKNOWLEDGEMENTS

In life gratitude exists in several forms. To be honest and emotional, which I let myself to be for the duration of this section, I cannot really list all the people for who I owe gratitude. Thus, this sentence is dedicated to the people who, though not named, have undoubtedly contributed to my successful PhD journey. To give the first names, I would like thank for my parents, Mahó Sándor and Szabó Zsuzsanna, who raised me in a supportive, intellectual family, who always believed in me, who always backed me up, even in the most forlorn times. I am also deeply grateful for the love of my life, my Zsolt, who supported me during the PhD studies, who always cheered me up, even in my grumpy moments. For my brother, Sebi, I am also very thankful, without him, I wouldn't be the person, who I am. To continue with the series of the important names, I have to mention my supervisor, Nedjeljka Žagar, who supported me right from the start of my PhD project. Without her profound knowledge in meteorology and her guidance in the Labyrinth of Tropical Dynamics I would not have reached this far. Thank you for considering me for offering this PhD position in December 2020, which was a fantastic Christmas gift for me. Sergiy Vasylykevych, who co-supervised me has also a huge part in guiding me during my PhD studies, especially when I needed technical support or some encouraging words. Thank you Sergiy for answering all my questions, which sometimes were trivial. I am more than grateful for Frank Lunkeit for his warm-hearted support during my PhD, who never hesitated to provide data for my research or to read some of my texts. Among the fellow PhD students in the university, I would like to highlight Valentino Neduhal, my office room mate, in whom I found a wonderful friend, who supported me in critical moments, who brought joy into the office, who was always eager to debug my code. I would also like to thank to my other PhD fellow, Katharina Holube for the great discussions, oftentimes in German too, and for carefully checking the content, the grammar, the spelling of my papers and this present dissertation. Without other group members, life in Grindelberg would have been much different. Thank you Chen, Iana, Yuan-Bing, Robin, Qijun, Peishan and Paolo for being around for a discussion, a lunch or a technical question. I also owe gratitude to Lea from TRR, who kept an eye on us, students over the years within the research project, who tirelessly organized schools, workshops, courses and German Café. From TRR, I am also grateful to my mentor, Florian, who always provided me with advice during my PhD. It was also a pleasure to meet other people from different scientific backgrounds from the guesthouse in Rentzelstraße, where I spent my first year in Hamburg. Simone, Bharat, Maria, Arim, Mahesh, you brought joy in my life in Hamburg, thank you for the amazing and sometimes surreal moments we spent together! I cannot submit my thesis without mentioning two great friends from Helsinki from my Master's studies: Alex and Marcel. Thank you guys, for staying in touch and for the online meetings over the years where we could lighten our

minds a little. From Helsinki, I must also mention two other important friends with whom I studied meteorology: Thomas and Johannes. Thank you guys for the discussions, for sharing our research with each other, it meant a lot to me! Last but not least, I would like to thank those people who played an immense role in preparing me for becoming a scientist: Victoria Sinclair, Gál Tamás, Heikki Järvinen, Jouni Räisänen, Zsebeházi Gabriella, M. Tóth Tivadar, Sümegi Pál, Leelőssy Ádám and Vlasits Géza. Thank you all!

# 1 Introduction

The tropics have a prominent role in the general circulation of the atmosphere. As the tropical region is dynamically coupled to the midlatitudes by atmospheric teleconnections (e.g., Sardeshmukh and Hoskins, 1988; Grimm and Dias, 1995), the circulation in the tropics has a profound impact on the weather in Europe, for instance. Thus, gaining knowledge in tropical atmospheric dynamics is not only key to understanding tropical phenomena such as equatorial waves, but also to improving complex atmospheric models, better understanding the ongoing climate change, and, last but not least, providing more skillful extended range weather forecasts. For example, Žagar (2017) shows that the largest initial uncertainties in NWP (Numerical Weather Prediction) models and the largest initial growth of forecast errors are related to the tropics. Since forecast errors can propagate from the tropics to higher latitudes in long-range forecasts, it is crucial to understand tropical variability, a goal to which this thesis seeks to contribute. Since variability in the tropics is connected to a wide range of spatial and temporal scales, there is a multitude of dynamical phenomena that are widely studied in this context such as equatorial waves, the Madden-Julian oscillation, tropical cyclones, African easterly waves, mesoscale disturbances, cumulus convection, etc. This thesis focuses on equatorial waves, particularly the mixed Rossby-gravity wave, a fundamental component of tropical circulation. In the following, I give a succinct introduction to tropical atmospheric dynamics in order to understand the role of the mixed Rossby-gravity wave in the context of circulation, meteorological phenomena and variability of the tropical region, which is followed by posing the research questions of this dissertation.

## 1.1 Fundamentals of the tropical atmospheric circulation

Compared to the midlatitudes, where the quasi-geostrophic theory is applied to explain the basic features of large-scale circulation, the tropics obtain a rather complex dynamics. Due to the smallness of the Coriolis parameter, horizontal temperature gradients are weak in the tropics resulting in a nearly non-divergent barotropic flow, which means that the flow cannot store large amounts of potential energy, which would be required for baroclinic energy transfer and the

emergence of baroclinic waves (Holton, 2004; Stephan et al., 2021). However, this reasoning is not valid for convective regions, which have particular importance in the tropics. These areas are associated with large diabatic heating rates, which provide the most important energy source in the tropics (Webster, 2020b). Tropical convection also excites a broad spectrum of equatorial waves responsible for driving the 2-10 day variability in the tropics (Webster, 2020a). Equatorial waves can interact with each other (Raupp and Silva Dias, 2005) and with the mean flow (Zhang and Webster, 1992; Holube et al., 2024), which can have remote effects (Sardeshmukh and Hoskins, 1988; Jin and Hoskins, 1995). In return, extratropical disturbances and the subtropical jet (Webster and Holton, 1982; Barpanda et al., 2023) can also impact equatorial waves and thus tropical weather.

In tropical dynamics research, several studies involving low-complexity models have been found useful for explaining basic dynamical phenomena. One of the most important of these conceptual models is the study by Gill (1980), who examined the response of the tropical atmosphere to stationary diabatic heating on the equatorial  $\beta$ -plane. In deriving the analytical response, Gill (1980) assumed the longwave approximation, which omits the local time derivative of the meridional wind. The analytical solution involves an eastward propagating divergent wave (the Kelvin wave) and two westward propagating vortices north and south of the equator (equatorial Rossby waves), which is often referred to as Matsuno-Gill pattern. Such a model describes well the observed structure of the planetary-scale Walker circulation (Maher et al., 2019). The shallow water system has also been useful to derive equatorial waves (Matsuno, 1966), to describe tropical-extratropical interactions (Webster and Holton, 1982; Barpanda et al., 2023), and has also a great potential to study and evaluate individual wave-wave and wave-mean flow interactions (Vasylkevych and Žagar, 2021), which are proposed to be important mechanisms for energy transfers in the tropics (Stephan et al., 2021). One of the objectives of this thesis is to study such interactions in terms of the mixed Rossby-gravity wave, which is of primary importance among the equatorial waves in the tropics as the subsequent sections argue.

## 1.2 Theory and identification of equatorial waves

Large-scale eastward and westward propagating disturbances trapped at the equator are often referred to as equatorial waves (EW), which play a fundamental role in tropical variability (e.g., Žagar et al., 2009; Dias and Kiladis, 2016; Yang et al., 2023). Satellite irradiance and tropical precipitation data showed that EWs can be coupled to convection, thereby gaining the name of convectively coupled equatorial waves (CCEWs) (Chang, 1970; Wheeler and Kiladis, 1999). Although in the recent decades the representation of EWs has improved both in NWP

systems (Bechtold et al., 2008) as well as in coupled climate models (Hung et al., 2013), there still remain model errors related to EW variability (Žagar, 2017; Jung and Knippertz, 2023), which underscores the need to better understand EW dynamics in the tropics.

The first theory on EWs originates from the study of Matsuno (1966), who derived solutions to the rotating shallow water equations on the equatorial  $\beta$ -plane linearized around a motionless mean state. The solutions include a fast and a slow-moving regime, inertia-gravity and Rossby waves respectively, as well as two special wave solutions existing only at the equator, the Kelvin wave and the mixed Rossby-gravity (MRG) wave. The latter one is also often referred to as Yanai wave thanks to its discoverer (Yanai and Maruyama, 1966). Longuet-Higgins (1968) showed numerically that the wave solutions obtained by Matsuno (1966) exist for the horizontal components of the linearized Laplace tidal equations, i.e., the spherical rotating shallow water equations. These solutions are also known as Hough harmonics.

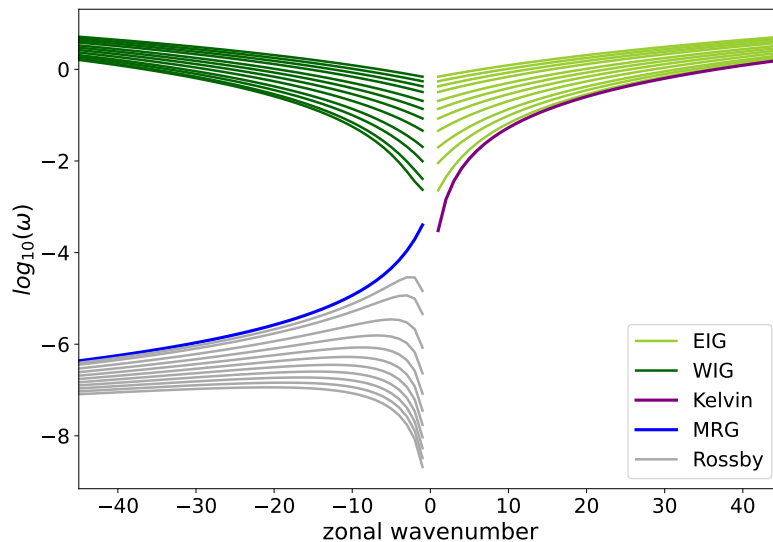


**Figure 1.1.** Dispersion curves of the linear wave solutions of the linearized spherical rotating shallow water equations for equivalent depth  $D = 10$  km. Eastward and westward inertia-gravity waves (EIG and WIG respectively) are shown by green curves. Rossby, MRG and Kelvin waves are shown by grey, blue and purple curves respectively. The frequency ( $\omega$ ) is normalized by  $2\Omega$ .

As the dispersion diagram of the linear wave solutions demonstrates (Figure 1.1), the Kelvin and the MRG waves make the fast and slow dynamical regimes inseparable in wavenumber-frequency space in contrast to midlatitudes, where these waves do not exist. Figure 1.1 also illustrates that MRG waves propagate to the west with increasing absolute phase velocity towards larger scales (i.e. towards smaller  $|k|$ ). It is important to note that the MRG and

the Kelvin mode obtain the meridional mode index  $n = 0$  in the solution of Longuet-Higgins (1968). Note as well that the eastward moving MRG mode described by Matsuno (1966) appears as the eastward moving IG mode with meridional index  $n = 1$  in the derivation of Longuet-Higgins (1968), therefore in this thesis the MRG wave or mode is only referred to the westward propagating MRG wave.

The shallow water mean depth ( $D$ , or the equivalent depth) is a critical parameter for EWs, since it affects inter alia the trapping scale (i.e. the meridional e-folding scale) and the frequency of EWs. In linear wave theory  $D$  appears as a separation constant for coupling the horizontal and vertical structure equations, thereby  $D$  is connected to a certain vertical mode. Typical equivalent depths considered for tropospheric dry EWs range from 250 and 400 m (e.g., Kasahara and da Silva Dias, 1986; Žagar et al., 2022), whereas for CCEWs  $D$  is an order of magnitude smaller due to convection that reduces stability and slows down wave propagation (Dias et al., 2013). In linear wave theory, vertical stability affects horizontal dispersion, thereby having a great influence on vertical modes (Knippertz et al., 2022).

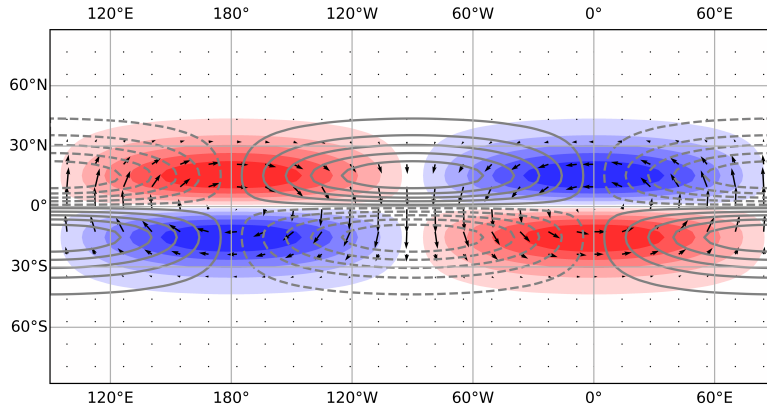


**Figure 1.2.** Theoretical MRG wave field with  $D = 400$  m and  $k = 1$ . Arrows and shaded contours denote the horizontal wind and geopotential height perturbation field. Grey contours stand for the divergence field.

Generally, the Kelvin, the MRG, and the Rossby and IG waves of the lowest meridional modes belong to the species of EWs, although most of them have a large non-equatorial wave component when a large  $D$  is considered. The horizontal structure of spherical MRG waves of zonal wavenumber ( $k$ ) 1 can be followed in Figure 1.2. MRG waves are divergent and they are associated with asymmetric height and zonal wind field, and symmetric meridional wind field with large cross-equatorial flow. When a non-zero background flow is considered (i.e. the effect of Doppler shift), Zhang and Webster (1989) showed in a westerly mean flow the frequency and the meridional extent of MRG waves increase, whereas their phase speed decreases, which is

only apparent towards low-frequency solutions (i.e. towards large  $|k|$ ). In an easterly mean state, the opposite was found.

Multiple methods have been proposed to diagnose EWs from real data, which diverge into two directions: space-time and spatial filtering (Knippertz et al., 2022). As one of the first attempts Hayashi (1971) introduced space-time power spectral analysis, which was utilized by Takayabu (1994) to isolate CCEWs from satellite infrared data. Wheeler and Kiladis (1999) extended this approach by considering outgoing longwave radiation (OLR) as a proxy for tropical convection. This method considers narrow filter windows for individual EWs that are defined based on peaks in wavenumber-frequency spectra. These peaks are associated with different EWs provided that they are significantly larger than a red background spectrum. In the method of Wheeler and Kiladis (1999) the wavenumber-frequency filtering is done by Fast Fourier Transform (FFT), which can be replaced by wavelet transform that allows localization in longitudinal direction and time (Wong, 2009). As Gehne and Kleeman (2012) show, wavenumber-frequency filtering can be performed on coefficients of parabolic cylinder functions (PCF) that describe the meridional structure of  $\beta$ -plane EWs. Since PCFs form a basis in the meridional direction, the meteorological data considered for EW filtering is projected onto PCFs at every longitudinal grid, which is followed by computing the wavenumber-frequency spectra for PCF coefficients.

Apart from space-time filtering, spatial projection methods are also common to identify EWs. Žagar et al. (2015) developed an algorithm based on Kasahara and Puri (1981), which projects instantaneous 3D global zonal wind, meridional wind and geopotential height fields onto 3D normal modes of the adiabatic frictionless primitive equations on the sphere, whose horizontal components are composed of the Hough harmonics. In contrast to space-time filtering, 3D normal mode decomposition is independent of time and no parameter related to convection enters into the computations meaning that convectively coupled and dry EWs are also filtered simultaneously. Note that time information can also be filtered if time series of Hough spectral coefficients are decomposed via FFT, however, as Žagar et al. (2022) demonstrated, this approach is sensitive to the fluctuations of wave amplitudes and phases, which is more relevant in the troposphere than in the stratosphere where EWs behave more like free dry waves. Other spatial projecting methods involve 2D projection of univariate fields onto PCFs (Yang et al., 2003) or onto EOFs derived by convection-related fields (Roundy et al., 2009). As PCFs are  $\beta$ -plane solutions, they are not global, thus the method of Yang et al. (2003) can be applied only to the tropical belt. Furthermore, since no vertical structure functions are involved, an optimal equivalent depth needs to be assumed, which then gives the trapping scale of EWs.

All the listed methods rely on various assumptions and are sensitive to several dynamical

phenomena such as Doppler shift of the mean flow, vertical and horizontal shear, static stability variations with height, off-equatorial disturbances, non-Gaussian nature of tropical convection, which is highlighted by Knippertz et al. (2022) in their intercomparison study of EW diagnostics.

In this thesis MRG waves were studied by idealised model simulations with a shallow water model (TIGAR) (Vasylykevych and Žagar, 2021), therefore a similar method of Žagar et al. (2015) relying on Hough harmonics was applied for MRG wave diagnostics. Using Hough harmonics as basis functions enables MRG waves to be prognostic variables of shallow water models, thus the MRG wave tendencies modified by various dynamical processes can be quantified straightforwardly from the model output, which is a distinct advantage over other EW filtering methods.

### **1.3 Role of mixed Rossby-gravity waves in shaping tropical dynamics**

MRG waves contribute substantially to large-scale tropical circulation variability, which was proved by several EW filtering methods (Hendon and Liebmann, 1991; Wheeler et al., 2000; Žagar et al., 2009; Yang et al., 2023). For example, Stephan et al. (2021) showed that tropospheric MRG waves, as part of the unbalanced circulation, exert the largest impact on tropical subseasonal variability in synoptic scales (Figure 6b therein). Regarding the stratosphere, free MRG wave signals are also found by spectral analysis of observations (e.g. Yanai and Maruyama, 1966; Randel et al., 1990; Ern et al., 2008; Alexander and Ortland, 2010).

In terms of predictability, the role of MRG waves is also critical. For instance, by studying global forecast uncertainties, Žagar (2017) demonstrated that there is significant ensemble spread associated with MRG waves at synoptic scales, which is comparable with spreads associated with individual balanced Rossby modes.

The role of MRG waves in affecting tropical convection is also well-documented. Here it is important to mention convectively coupled MRG waves, which are prominent features of the asymmetric space-time OLR spectrum (Wheeler and Kiladis, 1999). There is also numerical evidence suggesting that MRG waves interacting with an MJO-like heat source excites off-equatorial vortical disturbances that resemble tropical depression-type waves (Aiyyer and Molinari, 2003), which can serve as a precursor for tropical cyclones (Feng et al., 2023). MRG waves can also influence convection over the Pacific thereby impacting tropical rainfall variability as shown by e.g., Zangvil and Yanai (1980); Magaña and Yanai (1995); Yokoyama and Takayabu (2012). Their role in the MJO initiation as well as the termination has been a focus of recent studies (Takasuka and Satoh, 2020; Chrisler and Stachnik, 2023). Regarding the MJO

initiation, Takasuka and Satoh (2020) showed through a statistical analysis that MRG waves play a significant role in mid-troposphere moistening in the Indian Ocean.

There are other phenomena of the tropical atmosphere in which MRG waves are proposed to play a role, although it is often subject of debate. For example, Hoskins and Yang (2021) suggested that MRG waves influence the Hadley cell dynamics in the upper troposphere in the equatorial east Pacific and Atlantic, however, Pikovnik et al. (2022) showed that the inclusion of MRG waves into their Hough function-based Hadley cell metric has a negligible impact. In a traditional view, MRG waves are important for the forcing of the easterly phase of the quasi-biennial oscillation (QBO) in the stratosphere (Holton and Lindzen, 1972), nevertheless recent modelling and observation-based studies suggest little influence (Alexander and Ortland, 2010; Kawatani et al., 2010; Holt et al., 2016) in contrast to Kelvin waves, which are important for forcing the westerly phase (Garcia and Richter, 2019).

Overall, MRG waves are vital ingredients for the spatio-temporal spectrum of tropical variability, therefore they are required for establishing any conceptual models for the tropics (Stephan et al., 2021).

## **1.4 Observations of MRG waves in the equatorial atmosphere**

MRG waves are observed throughout the troposphere and the stratosphere with varying spatial scales. Observational studies agree on the prevalence of synoptic-scale (zonal wavenumbers 4-5) MRG waves in the upper troposphere (e.g., Stephan et al., 2021) with periods of about 5 days (e.g., Yanai and Hayashi, 1969; Zangvil and Yanai, 1980). MRG waves with similar properties have been detected in the lower stratosphere implying that tropospheric MRG waves may propagate vertically (Yanai and Hayashi, 1969; Ricciardulli and Garcia, 2000; Alexander et al., 2008). There is also evidence that upper tropospheric MRG waves can transition into the lower troposphere, which was shown by Zhou and Wang (2007). The strongest MRG wave signal, on the other hand, is associated with the upper stratosphere, where MRG waves obtain planetary scales (zonal wavenumbers 1-3) and have a somewhat shorter period (2-3 days) compared to the troposphere (Randel et al., 1990; Hayashi, 1994).

The different zonal scales of the upper tropospheric and upper stratospheric transient MRG waves are illustrated in Figure 1.3 that shows climatological kinetic energy (KE) spectra of MRG waves derived from ERA5 reanalysis data (Hersbach et al., 2020) at 1 hPa and 200 hPa. The KE spectra are computed by the 3-dimensional wave filtering by the MODES software package (Žagar et al., 2015) followed by the level-by-level computation of the MRG wave KE.

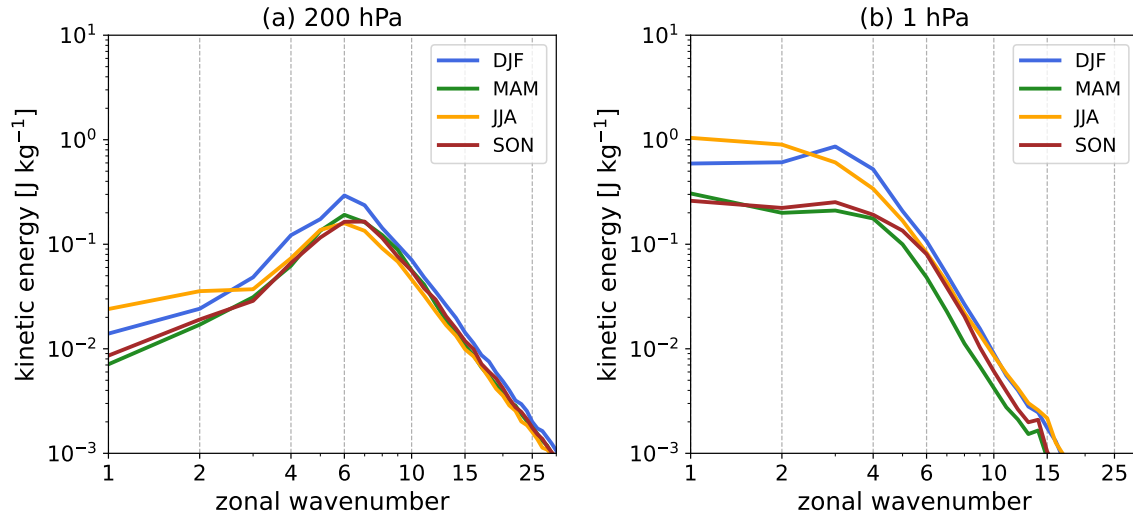


**Figure 1.3.** MRG wave filtering of ERA5 data (2005-2019) in different seasons. Mean kinetic energy spectra of MRG wave variability of 200 hPa (a) and 1 hPa (b) levels.

Details of the computation can be found in Section B15.1 of Appendix B. The upper tropospheric spectra have a distinct energy maximum at  $k = 6$  in all seasons with the peak amplitude in boreal winter (DJF) (Figure 1.3a). This is a new finding, since most observational studies agree on the MRG wave maximum in boreal summer and early autumn (Hendon and Liebmann, 1991; Magaña and Yanai, 1995; Roundy and Frank, 2004; Suhas et al., 2020). In boreal summer, the KE spectra at planetary scales are enhanced compared to other seasons. The upper stratospheric spectra are characterised by a much greater difference between the seasons with 4-5 times more energetic solstice seasons (DJF and JJA) than the transitional seasons (MAM and SON) (Figure 1.3b). In DJF, the MRG wave KE has a distinct maximum at zonal wavenumber  $k = 3$ , whereas in other seasons the planetary-scale KE spectra are more flat, with less pronounced maxima at  $k = 1 - 2$  (JJA) and  $k = 1$  and  $k = 3$  (MAM and SON).

Horizontal maps (Figure 1.4 and 1.5) representing the MRG wave variability across different seasons reveal the more equatorially bounded upper tropospheric MRG waves, which is consistent with linear wave theory, since tropospheric MRG waves obtain smaller mean depths than their stratospheric counterparts. The level of equatorial trapping shows a strong seasonality in the troposphere, where the average trapping scale is  $\sim 30-35^\circ$  with more meridionally extended MRG waves (up to  $50^\circ$ ) during the solstice seasons (JJA and DJF). The stratospheric MRG waves extend in the meridional up to approximately  $55-60^\circ$  with less pronounced seasonality in equatorial trapping compared to the upper troposphere.

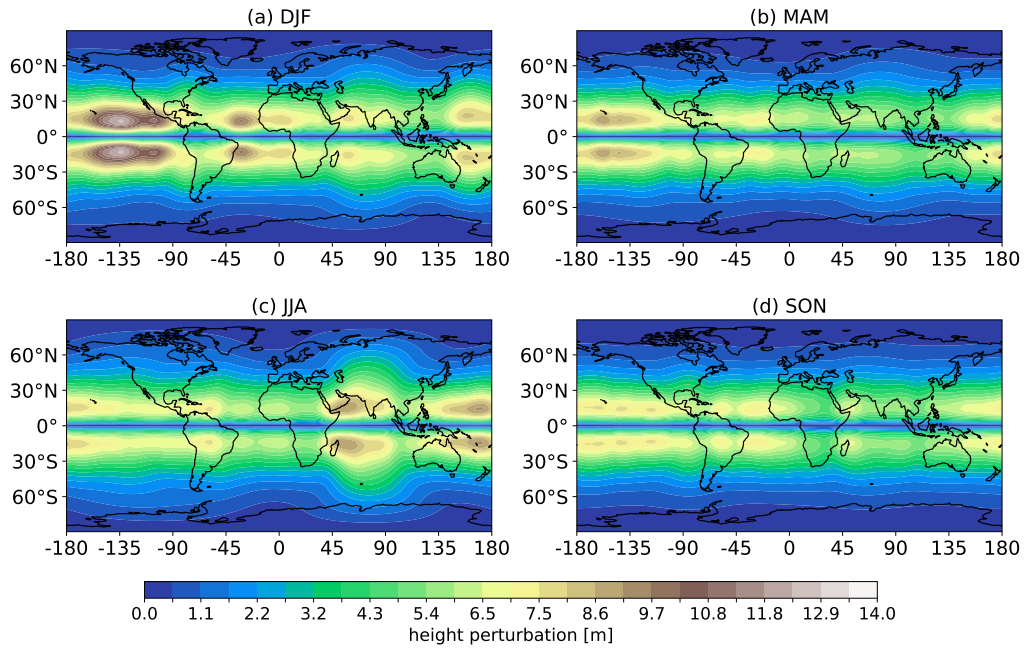


**Figure 1.4.** Horizontal maps of MRG wave variability in different seasons at 200 hPa. The contours show the absolute MRG wave height perturbation averaged in 2015-2019.

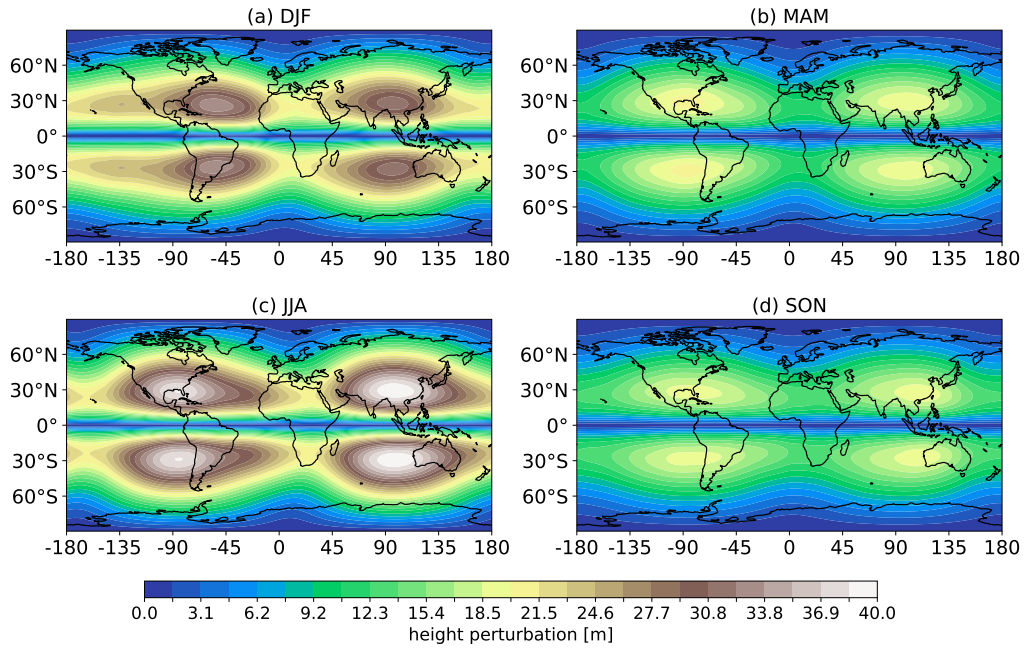


**Figure 1.5.** As in Figure 1.4, but for 1 hPa MRG waves.

## 1.5 Generation theories for MRG waves

Since the discovery of equatorial waves both in theory and in tropical observations, there has been many theories for the emergence of tropospheric MRG waves. A proper excitation theory should explain the observed features of the MRG waves, such as their frequency and their dominant zonal wavenumber. Typically, MRG waves obtain synoptic scales (zonal wavenumber 4-5) and a period of 5 days in the tropical troposphere (Zangvil and Yanai, 1980). Satellite data also suggests that MRG waves can be coupled to convection (Chang, 1970; Hendon and Liebmann, 1991; Wheeler and Kiladis, 1999), therefore any proposed excitation theory for tropospheric MRG waves should also clarify this connection.

Early studies showed that MRG waves can be generated by long-period, large-scale stationary tropospheric heating perturbations asymmetric about the equator (Holton, 1972; Silva Dias et al., 1983). In the study of Holton (1972) a standing oscillation of diabatic heating, which is explained by the influence of the Asian monsoon, generates MRG waves in the upper troposphere, which also propagate into the lower stratosphere. The downside of this theory is that the zonal scale selection of wavenumber 4-5 tropospheric MRG waves is missing.

The so-called lateral boundary forcing mechanism, which is analogous to midlatitude wave forcing, has also emerged in different forms in literature. This process originates from Mak (1969), who used stationary stochastic forcing at the lateral boundaries of the applied two-layer dry adiabatic model and showed that MRG waves are excited with a scale that is determined by the forcing wave through linear resonance. Wilson and Mak (1984) also demonstrated that it is possible to excite MRG waves by lateral boundary forcing, but in their model the interactions between a steady planetary tropical wave and forced synoptic-scale waves penetrating into the tropics generated the MRG waves. While there is some evidence that MRG wave activity is connected to extratropical wave disturbances in the Western Hemisphere (e.g. Yang et al., 2023), it is unlikely that midlatitude forcing is alone responsible for the observed MRG waves, since this theory does not explain the convective coupling and it is sensitive to the variations of the mean flow (Wilson and Mak, 1984; Zhang, 1993).

Other important mechanism proposed for MRG wave excitation is the linear wave - convective instability of the second kind (CISK) originating from Hayashi (1970). According to the wave-CISK process, MRG waves appear as unstable modes as a consequence of the interaction of circulation and cumulus convection. This interaction is often provided by the thermodynamic equation, which is forced by the convective parameterization. In wave-CISK, the MRG wave's vertical scale is determined by the convection, whereas the zonal wavenumber and the frequency is decided by the growth exponent, which is proportional to the frequency (Itoh

and Ghil, 1988). In wave-CISK the zonal scale selection fails, since IG waves are also produced by convection, which have much higher frequencies meaning that they overgrow the MRG mode (Itoh and Ghil, 1988). In a modified version of the theory, Itoh and Ghil (1988) suggested nonlinear wave-CISK process responsible for MRG wave generation with zonal wavenumber 4, which is the smallest MRG wave with a period long enough for receiving sufficient moisture during convection. Itoh and Ghil (1988) also added that during wave-CISK symmetric modes overgrow asymmetric modes including the MRG wave, thus asymmetric lateral boundary forcing is required to reinforce MRG waves. Another important aspect to mention is that the wave-CISK mechanism and the associated waves are sensitive to the convection parameterization, which was shown by Starx (1976) and Hess et al. (1993).

Raupp and Silva Dias (2005) proposed wave-wave interactions as an excitation for MRG waves. They utilized the nonlinear shallow-water equations on the equatorial  $\beta$ -plane solved by a spectral method that applied the eigensolutions of the linear problem as the spectral basis. The results of Raupp and Silva Dias (2005) indicate that MRG waves are excited by a nonlinear mechanism in which the slow Rossby modes excited by the asymmetric heat source generate a quasigeostrophic basic state that supplies energy especially to the MRG waves with zonal wavenumbers 4 and 5. They also show that the unstable MRG waves are strongly suppressed by the inclusion of fast IG modes in the integration. Nevertheless, there is no observational evidence for this nonlinear mechanism (Dias and Kiladis, 2016).

Despite the various mechanisms suggested for MRG wave excitation, it is still a topic of debate, since none of the listed generation theories could fully explain the origin of synoptic-scale MRG waves in the upper troposphere. Furthermore, no theory was proposed to explain the planetary-scale MRG waves in the upper stratosphere. Therefore, in the subsequent chapters I will propose interactions between wave perturbations and the asymmetric mean flow, i.e., wave-mean flow interactions, as a new generation theory for MRG waves, which explains the different scale selection in the upper troposphere and the upper stratosphere. Thus, this thesis will answer the following research questions:

1. How do wave-mean flow interactions initiate MRG wave excitation in the troposphere?
2. What is the relevance of wave-wave interactions and direct excitation by tropical convection compared to wave-mean flow interactions in the MRG wave generation?
3. Can the observed scales of upper tropospheric and upper stratospheric MRG waves be explained by wave-mean flow interactions?
4. Which property of the mean flow is responsible for the scale selection of MRG waves when they are generated by wave-mean flow interactions?

## 1.6 On the connection between barotropic instability and MRG wave growth in the QBO region

Dynamical instabilities facilitate rapid growth of small amplitude perturbations, thereby acting as wave sources in the atmosphere. Barotropic instability, which is related to the reversal of the meridional gradient of the absolute vorticity of the mean flow, can also lead to the growth of MRG wave-like disturbances (Winter and Schmitz, 1998), which may be an acting source in the region of the QBO in the stratosphere.

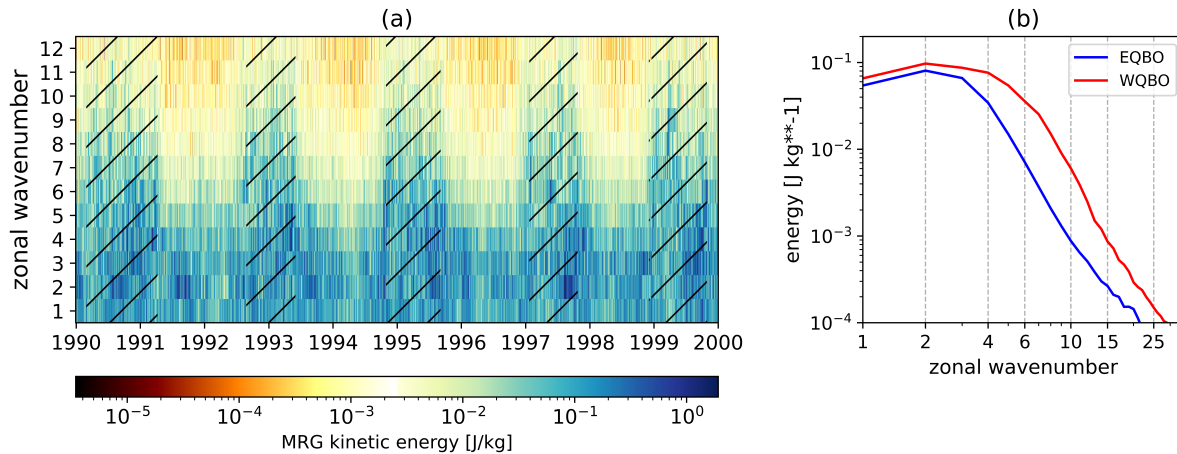


**Figure 1.6.** (a) 30 hPa MRG wave kinetic energy with respect to time and zonal wavenumber in the period of 1990-1999. The hatches denote the timesteps during the WQBO phase. (b) 30 hPa MRG wave kinetic energy spectra for the easterly and westerly QBO phase (blue and red respectively) averaged for 1990-1999.

Even though the peak MRG wave activity is observed in the upper troposphere (200 hPa) and the upper stratosphere (1 hPa) (see Section 1.4), the MRG wave amplitudes are non-negligible in the QBO region (at 10-70 hPa), which reach about 10-30% of the MRG waves present in the upper troposphere. Another important feature of instantaneous MRG waves is the lack of vertical wave propagation between the troposphere and the stratosphere (Žagar, 2015) implying local wave generation in the stratosphere.

The observed MRG wave kinetic energy (KE) at 30 hPa (Figure 1.6), where the QBO has strong amplitudes, indeed implies that MRG waves are related to the QBO, since MRG waves of zonal wavenumbers  $k > 5$  correlate well with the QBO phases (Figure 1.6a). The derivation of the KE data is discussed in Section C20 of Appendix C. Regarding the KE spectra, notice that there is excess of MRG wave activity during the westerly QBO phase across all zonal wavenumbers (Figure 1.6b), which is consistent with satellite observations (e.g., Ern et al., 2008).

Note also that the largest difference between the QBO phases are found in range of synoptic and subsynoptic scales (i.e.  $k = 5 - 15$ ).

I speculate that the MRG wave variability in the QBO region is driven by local MRG wave generation by barotropic instability of the QBO-related circulation. The QBO is the dominant mode of variability of the equatorial stratosphere at 10-70 hPa with alternating downward propagating easterly and westerly zonal wind regimes with an average period of 28 months (Baldwin et al., 2001). As part of the early theories for the existence of the QBO, Holton and Lindzen (1972) hypothesised that upward propagating Kelvin and MRG waves contribute to the westerly and the easterly acceleration of the QBO, respectively. However, observations (Alexander and Ortland, 2010; Ern et al., 2014), laboratory-based experiments (Plumb et al., 1978) and QBO-resolving numerical model simulations (Kawatani et al., 2010; Holt et al., 2022; Lee et al., 2024) indicate that a broad spectrum of waves, including equatorially trapped large-scale waves and small-scale gravity waves can provide sufficient forcing for the QBO (Butchart, 2022). Some studies also point out the minor role of MRG waves in forcing the QBO (Kawatani et al., 2010; Holt et al., 2016) and even suggest that these waves may be locally generated by flow instabilities in the stratosphere (Garcia and Richter, 2019).

The barotropic instability of the QBO has been first raised by Andrews and McIntyre (1976) who revealed that the meridional profile of the easterly acceleration of the QBO flow can become inflected, thereby the resulting mean flow can become barotropically unstable. Hamilton (1984) who utilized wind observations from 30 and 50 hPa from the tropical region also reported reversal of the absolute vorticity gradient both during the easterly and the westerly QBO phase. By studying ECMWF wind analysis Shuckburgh et al. (2001) argued that eddies centred at  $10^\circ$  with zonal wavenumbers 6-10 are products of barotropic instability development of the westerly QBO jet. Garcia and Richter (2019) simulated the QBO with the Whole Atmosphere Community Climate model and showed that the MRG wave signal is robust where the curvature of the westerly QBO jet is strong arguing that MRG waves are produced by barotropic instability development of the westerly QBO jet. Garcia and Richter (2019) also implied that MRG waves can have an important role in mixing (i.e., redistribution of vorticity) in the equatorial stratosphere, which was also raised by Shuckburgh et al. (2001). Yao and Jablonowski (2015) reported occurrence of barotropic instability in QBO simulations with an ensemble of dry GCM dynamical cores, and find increased MRG wave activity in models with strong instability indicators.

Despite the evidence of barotropic instability of the QBO circulation in observations and models, there has been no study analysing barotropic instability on longer periods. There is also lack of evidence for barotropic instability induced wave growth in the QBO region, which could explain MRG wave variability across the different QBO phases. Therefore, this thesis addresses

the following research questions:

1. Can the differences between MRG wave kinetic energy of the stratospheric easterly and westerly QBO phase be explained by barotropic instability?
2. What is the occurrence of barotropic instability in the QBO region over a 10-year period? Is there a difference between the easterly and the westerly QBO phase?
3. How relevant is barotropic instability-initiated growth for MRG waves in the QBO region? Which zonal wavenumbers are sensitive to instability growth?

## 2 Numerical modelling of MRG wave generation

To study processes contributing to MRG wave generation, I used the TIGAR model (i.e., Transient Inertia-Gravity And Rossby wave dynamics, Vasylyevych and Žagar (2021)), which is a spectral nonlinear spherical rotating shallow water model. The model equations in spherical coordinates  $(\lambda, \varphi) \in [0, 2\pi) \times (-\pi/2, \pi/2)$ , in the absence of bottom topography, are as follows:

$$\frac{du}{dt} - v \left( 2\Omega \sin \varphi + \frac{u}{a} \tan \varphi \right) + \frac{g}{a \cos \varphi} \frac{\partial h}{\partial \lambda} = -\frac{1}{\tau_R} u, \quad (2.1a)$$

$$\frac{dv}{dt} + u \left( 2\Omega \sin \varphi + \frac{u}{a} \tan \varphi \right) + \frac{g}{a} \frac{\partial h}{\partial \varphi} = -\frac{1}{\tau_R} v, \quad (2.1b)$$

$$\frac{dh}{dt} + h \nabla \cdot \mathbf{V} = Q - \frac{1}{\tau_N} (h - D), \quad (2.1c)$$

where  $d/dt$  is the material derivative,  $\mathbf{V} = [u, v]$  denotes the horizontal velocity vector composed of the zonal ( $u$ ) and the meridional component ( $v$ ),  $h$  is the total fluid depth,  $D$  is the mean depth,  $g$  and  $\Omega$  are the gravity constant and the rotation rate of the Earth respectively,  $a$  is the radius of the Earth.  $Q$  represents the forcing term, which is modelled as a Gaussian heat source (see Equation A2.12 in Appendix A). The two dissipative terms, namely the so-called Rayleigh friction in the momentum equations and the Newtonian cooling in the continuity equation, are defined by their characteristic time scales  $\tau_R$  and  $\tau_N$ , respectively. Additionally, spectral viscosity is applied similarly as in Gelb and Gleeson (2001) to guarantee realistic energy distribution at the smallest scales while minimally influencing the model physics, which is discussed in Section A8.1 of Appendix A.

TIGAR uses Hough harmonics as spectral expansion basis to solve Equation 2.1 meaning that the MRG wave spectral coefficient appears as a subset of the model prognostic variables. This modelling framework allows studying the generation of MRG waves directly from the model output, and dynamical processes contributing to the MRG wave tendencies are quantifiable, which is a major asset that the model possesses over other EW filtering methods as highlighted

at the end of Section 1.2. Moreover, TIGAR also allows separating the dynamical contributions of forcing if applicable, linear dynamics, and interactions between different sets of modes during the model integration. All sorts of interactions involving the mean state ( $k = 0$  modes), and waves ( $k > 0$  modes) including Rossby, IG, Kelvin and MRG waves can be quantified, which are computed with high precision, meaning that the sole source of numerical errors in the evaluation of spectral tendencies comes from the spectral truncation.

For this thesis three versions of the TIGAR model were applied to isolate the effect of wave-mean flow interactions: the full nonlinear model (i.e. Equation 2.1), the linearized model and the resting state linear model. The linearized version solves the rotating shallow water equations linearized about a prescribed geostrophically balanced zonal flow. Separating the model prognostic variables into the zonal mean part (denoted by an overbar) and a perturbation (denoted by  $'$ ),

$$u = \bar{u}(\varphi) + u'(\lambda, \varphi, t), \quad v = v'(\lambda, \varphi, t), \quad h = \bar{h}(\varphi) + h'(\lambda, \varphi, t),$$

the linearized model equations read

$$\frac{\partial u'}{\partial t} - v' 2\Omega \sin \varphi + \frac{g}{a \cos \varphi} \frac{\partial h'}{\partial \lambda} = -\frac{\bar{u}}{a \cos \varphi} \frac{\partial u'}{\partial \lambda} - \frac{v'}{a} \frac{\partial \bar{u}}{\partial \varphi} + \frac{\bar{u}v'}{a} \tan \varphi - \frac{1}{\tau_R} u', \quad (2.2a)$$

$$\frac{\partial v'}{\partial t} + u' 2\Omega \sin \varphi + \frac{g}{a} \frac{\partial h'}{\partial \varphi} = -\frac{\bar{u}}{a \cos \varphi} \frac{\partial v'}{\partial \lambda} - 2\frac{\bar{u}u'}{a} \tan \varphi - \frac{1}{\tau_R} v', \quad (2.2b)$$

$$\frac{\partial h'}{\partial t} = -\frac{\bar{u}}{a \cos \varphi} \frac{\partial h'}{\partial \lambda} - \frac{v'}{a} \frac{\partial \bar{h}}{\partial \varphi} - \frac{\bar{h}}{a \cos \varphi} \frac{\partial u'}{\partial \lambda} + \frac{\bar{h}}{a} \frac{\partial v'}{\partial \varphi} + Q - \frac{1}{\tau_N} (h' - D). \quad (2.2c)$$

The linearized model allows interactions only between the mean state and the wave modes (i.e. wave-mean flow interactions), whereas wave-wave interactions are not permitted. The resting state linear model considers no mean flow. The corresponding model equation is obtained by setting  $\bar{u} = 0$  and  $\bar{h} = D$  in Equation 2.2. In such a model, neither wave-mean flow nor wave-wave interactions are supported.

Overall, the resting state linear model isolates the effect of the forcing, whereas the linearized model is designed to study the effect of wave-mean flow interactions. The full nonlinear model contains all sorts of interactions between the wave and the mean state modes, which is used to study the importance of wave-wave interactions. More details of the TIGAR versions including the solution methods are given in Section A2 of Appendix A. Furthermore, from now the nonlinear, the resting state linear and the linearized TIGAR model will be referred to as NL, LI, and LZ, respectively.

By using the concept of the linearized TIGAR model (Equation 2.2) without forcing

and dissipation, one can compute eigenmodes of the shallow water system linearized around an arbitrary geostrophically balanced zonal mean state, and determine whether these background eigenmodes are barotropically unstable. I used such a method to conduct a long-term analysis of unstable background eigenmodes of the 30 hPa zonal mean flow to investigate the barotropic instability of the equatorial region (where the QBO is active), and to study the relation between unstable modes and MRG wave growth.

The computation of the unstable background eigenmodes is done by the BGHough software (Holube et al., 2024) that is based on the algorithm proposed by Kasahara (1980). First, the spherical shallow water equations are linearized around the arbitrary balanced mean state by assuming a specific equivalent depth  $D$ . This is followed by substituting the wave ansatz

$$\mathbf{W} = [u', v', h']^T = \hat{\mathbf{W}}(\varphi) e^{i(k\lambda - \sigma t)} \quad (2.3)$$

into the linearized equations, where  $\sigma$  is the non-dimensional complex eigenfrequency. The meridional structure of the wave ansatz ( $\hat{\mathbf{W}}$ ) can be expressed by a series of Hough meridional functions for a specific zonal wavenumber ( $k$ ). This reduces the linearized equations into a solvable eigenvalue problem. Thus, the background eigenmodes are computed for individual zonal wavenumbers in range of  $k = 1, 2, \dots, K$ , which can be repeated for several timesteps in case of a long-term analysis. The analysed outputs of BGHough consist of the background eigenmodes' horizontal structures (i.e., the global fields  $u', v', h'$ ) and the associated eigenfrequency  $\sigma$ , whose imaginary part gives the modal growth exponent by barotropic instability provided that  $\Im[\sigma] > 0$ . In each timestep BGHough computes  $25 \times 3$  background eigenmodes classified into westward IG, eastward IG or the Rossby category, therefore for each timestep  $75 \times K$  modes are analysed. Further details of the BGHough software can be found in Section C17.3 of Appendix C.

### **3 Generation and growth of MRG waves in the equatorial troposphere and stratosphere**

This chapter presents the main results of the present dissertation focusing on the mechanisms that contribute to the growth of MRG waves (or the MRG mode) in the equatorial troposphere and stratosphere. These results are also presented extensively in research papers that are included in the Appendices. First, I present the new mechanism proposed for the excitation of MRG waves, i.e. wave-mean flow interactions. Subsequently, it will be shown how important such process can be compared to wave-wave interactions and direct wave generation by a tropical heat source. This will be followed by demonstrating how the zonal scale of MRG waves is selected by wave-mean flow interactions and how this scale selection process can explain the upper tropospheric and upper stratospheric MRG wave scales. Last, I present barotropic instability as an important factor for MRG wave growth in the QBO region in the stratosphere.

## 3.1 Excitation of MRG waves by wave-mean flow interactions

### 3.1.1 Numerical simulations for detecting MRG wave generation

To answer research questions 1-2 posed in Section 1.5, numerical simulations were performed with the TIGAR model, including the NL, the LZ and the LI version. Such simulations helped to detect the processes causing MRG wave generation.

The experiments consider a steady Gaussian heat source mimicking large-scale convection (Equation A2.12 of Appendix A), and geostrophically balanced background zonal flows that are either analytical jet profiles or derived from reanalyses. Additional simulations used the background state of rest.

The background flows are zonal steady states of the nonlinear rotating shallow water equations without damping (Equation A8.19a in Appendix A). The balanced background geopotential height field was generated by projecting the prescribed zonal wind field onto  $k = 0$  Rossby modes as described in Section A8.2 of Appendix A.

The analytical jet profiles (see Figure A2 in Appendix A) consist of symmetric and asymmetric subtropical jets (SYMJET and ASYJET). The ASYJET zonal wind profile has a weaker jet in the Southern Hemisphere that is shifted further away from the equator compared to the jet north of the equator. The SYMJET profile includes two identical subtropical jets in the Northern and the Southern Hemisphere. The motionless initial state is denoted NOF. Further simulations were run with background zonal wind profiles derived from ERA5 reanalysis (Hersbach et al., 2020). I used seasonal zonally-averaged zonal wind from 200 hPa in years 1993, 1999, 2009, 2012 and 2016 from the boreal summer and spring seasons (JJA and MAM, respectively). By studying the energetics of the ERA5 mean states, it was found that during JJA the flow contains significantly more energy in asymmetric (i.e.  $n = 2, 4, 6, \dots$ )  $k = 0$  Rossby modes compared to the MAM basic states. Similar arguments were found in between the SON and DJF seasons, but the differences were the largest between JJA and MAM, thus the simulations were limited to these two seasons.

Numerical simulations were run with two shallow water mean depths:  $D = 250$  m and  $D = 400$  m, which correspond to characteristic values of the equivalent depth of the tropical atmosphere as demonstrated by e.g., Kasahara and da Silva Dias (1986); Žagar et al. (2022).

To quantify the importance of wave-wave and wave-mean flow interactions, location and symmetry of the heat source, the shallow water mean depth and symmetry of the mean state, a number of sensitivity experiments were carried out, which are summarized in Table 3.1. Note that the Gaussian forcing is called symmetric/asymmetric whenever  $Q$  is centred at the

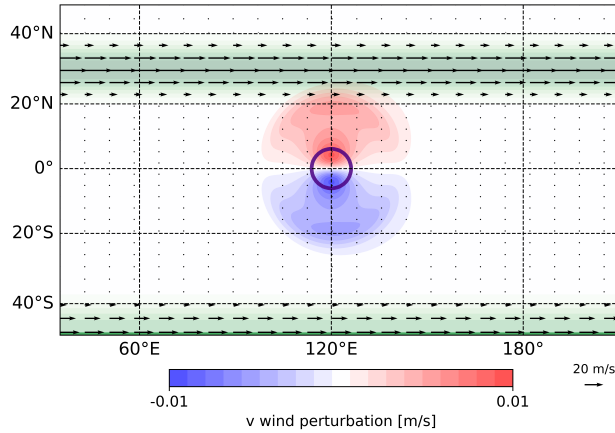


**Figure 3.1.** Snapshot of the nonlinear SYMFOR-ASYJET global TIGAR simulation (shown in a limited area). Blue and red shading denotes the waves produced by the forcing that is represented by the purple contour. The mean flow is shown by the green shades and the arrows.

equator/away from the equator. As an example, Figure 3.1 depicts an early stage of the nonlinear SYMFOR-ASYJET simulation demonstrating the IG waves generated by the symmetric forcing reach and potentially interact with the zonally asymmetric subtropical zonal jets. More details about the setup of the numerical experiments are given in Section A2 of Appendix A.

**Table 3.1.** Summary of the TIGAR numerical experiments defined by the symmetry of the forcing, the shape of the background zonal wind, the TIGAR version and the applied shallow water mean depth  $D$ .

Exp label	Forcing symmetry	Background flow	TIGAR version	$D$
ASYMFOR-NOF	asymmetric	state of rest	NL, LI	400 m, 250 m
SYMFOR-NOF	symmetric		NL	
SYMFOR-SYMJET		symmetric jet	NL	
SYMFOR-ASYJET		asymmetric jet	NL, LZ	
ASYMFOR-ASYJET	asymmetric	asymmetric jet	NL	400 m
SYMFOR-MAM SYMFOR-JJA	symmetric	ERA5 mean flows of MAM or JJA	NL	400 m
ASYMFOR-MAM ASYMFOR-JJA	asymmetric			

### 3.1.2 Wave-mean flow interactions as MRG wave generation

An asymmetric heat source in the tropics leads to direct excitation of MRG waves as shown by Holton (1972), since the forcing directly projects onto the asymmetric MRG mode. In the ASYMFOR-NOF experiments performed with the LI and NL model versions, the MRG waves are excited instantaneously reaching a quasi-equilibrium state determined by the damping timescale. No qualitative difference was found between the LI and NL simulations indicating that wave-wave interactions are irrelevant as an excitation mechanism in this setup. It was also found that the MRG wave energy and the ratio of energies in the MRG and Rossby modes is sensitive to the model setup and forcing parameters, which was also demonstrated by Silva Dias et al. (1983). For instance, the largest MRG wave growth was found when the heat source is placed at the scale of the equatorial deformation radius (i.e. around  $10^\circ$  in case of  $D = 400$  m).

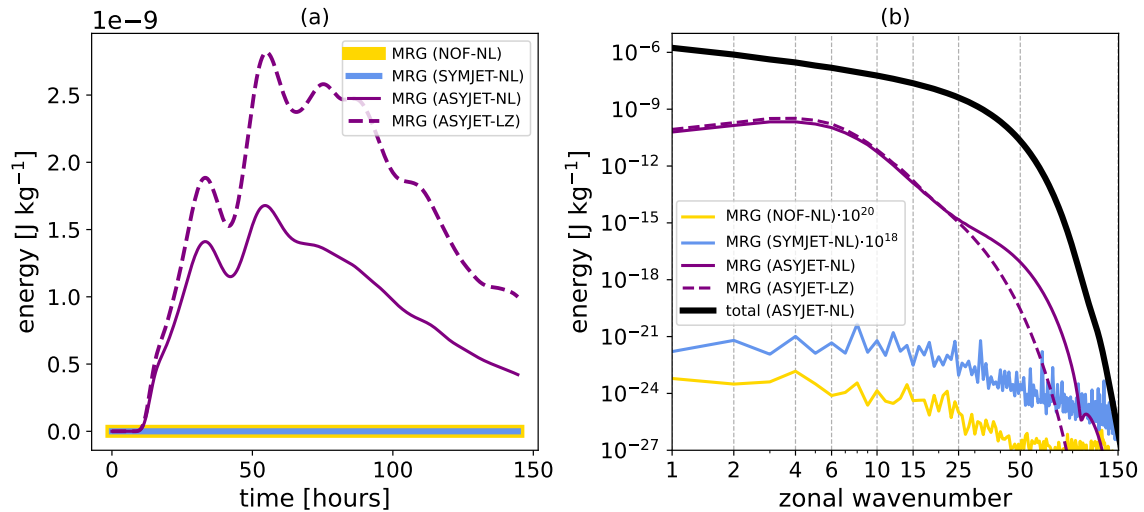


**Figure 3.2.** (a) Evolution of the MRG wave energy in SYMFOR-NOF, SYMFOR-SYMJET and SYMFOR-ASYJET simulations with  $D = 400$  m. (b) MRG wave energy spectra of the same simulations as in (a) and the total wave energy in the SYMFOR-ASYJET NL simulation (black).

In simulations where the heat source is symmetric, the MRG waves could not be initiated by the forcing. However, MRG wave growth was still experienced, which was influenced by the background flow. Figure 3.2a compares the time evolution of MRG wave energy in between four simulations run with symmetric forcing: SYMFOR-NOF, SYMFOR-SYMJET and SYMFOR-ASYJET. All simulations are run with the full NL model, except SYMFOR-ASYJET, which is also run with the LZ model. The striking feature of Figure 3.2a is that MRG waves are excited only in simulations using an asymmetric background state (i.e. ASYJET profile), meaning that interactions between the waves generated by the symmetric heat source and the asymmetric subtropical jet, i.e., wave-mean flow interactions, are the cause of the MRG wave growth. At the

start of the ASYJET NL simulation only symmetric modes are present among the waves in the system, which rules out the possibility that triad interactions produce asymmetric  $k > 0$  modes. Thus wave-wave interactions could not initiate the observed MRG wave growth. The excitation timescale in Figure 3.2a, which is about 9 hours, matches the time required for the IG waves excited by the heat source to reach the jet region. This timescale depends on the mean depth  $D$  and it can be estimated by knowing the location of the jet flanks and the gravity wave speed  $\sqrt{gD}$ . Another feature of Figure 3.2a is a significant difference in energy levels between the ASYJET NL and LZ simulations after the first  $\sim 24$  hours, which is due to the linear damping. In the NL simulation, the damping acts on both the zonal mean flow and the waves whereas only waves are damped in the LZ experiment resulting in a decreased energy extraction from the system.

Time-averaged MRG wave energy spectra for the same simulations are demonstrated by Figure 3.2b. The averaging time (3 days) covers the period of the MRG wave development and is within the typical lifetime of MRG waves observed in the troposphere (Zangvil and Yanai, 1980). The total energy spectrum of the ASYJET NL simulation shows a typical red spectrum with the total energy continuously decreasing with the zonal wavenumber. In contrast, the MRG wave energy spectra of the ASYJET simulations obtain a peak at zonal wavenumber  $k = 4$ . Since the energy spectrum is similar in between the ASYJET NL and LZ simulations at large scales, wave-wave interactions are irrelevant for the MRG wave generation process. The differences between NL and LZ beyond  $k \approx 25$  are caused by the interactions between  $k = 0$  IG and  $k > 0$  modes, which are absent in the linearized system. It is also important to highlight that no significant difference was found between the simulations run with the two equivalent depths. The spectral peak of MRG waves at  $k = 4$  found in the idealised TIGAR simulations is consistent with observations, in which MRG waves also obtain synoptic scales, i.e.  $k = 4 - 5$  (Yanai and Maruyama, 1966; Zangvil and Yanai, 1980; Stephan et al., 2021).

Analysis of the MRG wave tendencies in physical space (Figure 3.3) revealed that the advection of mean momentum by the forced gravity waves (i.e., term  $-v' \partial \bar{u} / \partial \varphi$ ) drives the MRG wave excitation, however, other terms also show positive contributions succeeding the excitation. Overall, the advective terms in the momentum equations contribute the most to the MRG wave growth in the first 24 hours of simulation time. The advection and the divergence term in the continuity equation have only slight contributions. In addition, the terms involving  $\tan \varphi$ , i.e., the metric terms are practically negligible.

A favorable condition for the MRG wave generation is when the westerly jet is located relatively close the equator, i.e. within the meridional length scale of the MRG waves for a given  $D$ . This is verified by carrying out simulations in which the jets are moved further away from the tropics (not shown). This also means that interactions of the balanced mean state with

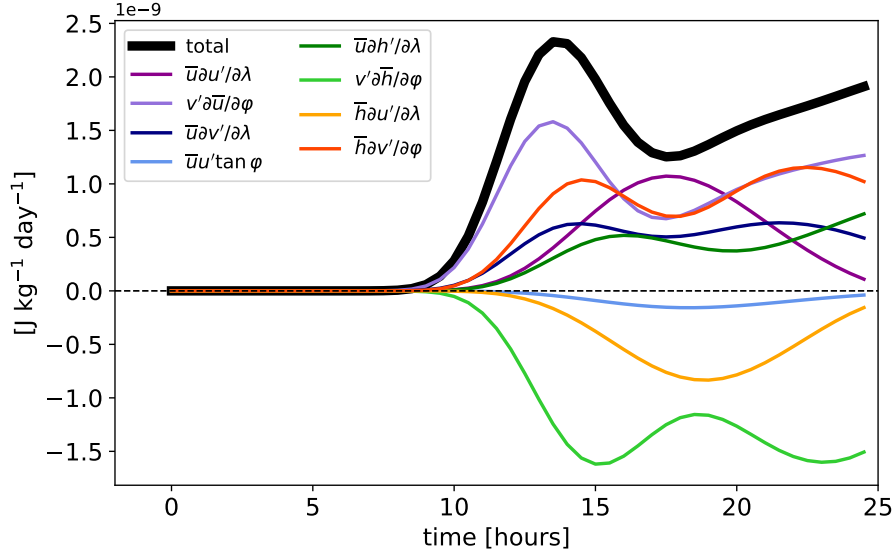


**Figure 3.3.** MRG wave energy tendency separated to contributions by different terms in physical space in the first day of simulation. All tendencies involving first order interactions from Equation 2.2 are shown by coloured curves. The thick black curve shows the MRG wave energy tendency due to all sorts of interactions. The simulation analysed is that of SYMFOR-ASYJET NL ( $D = 400$  m).

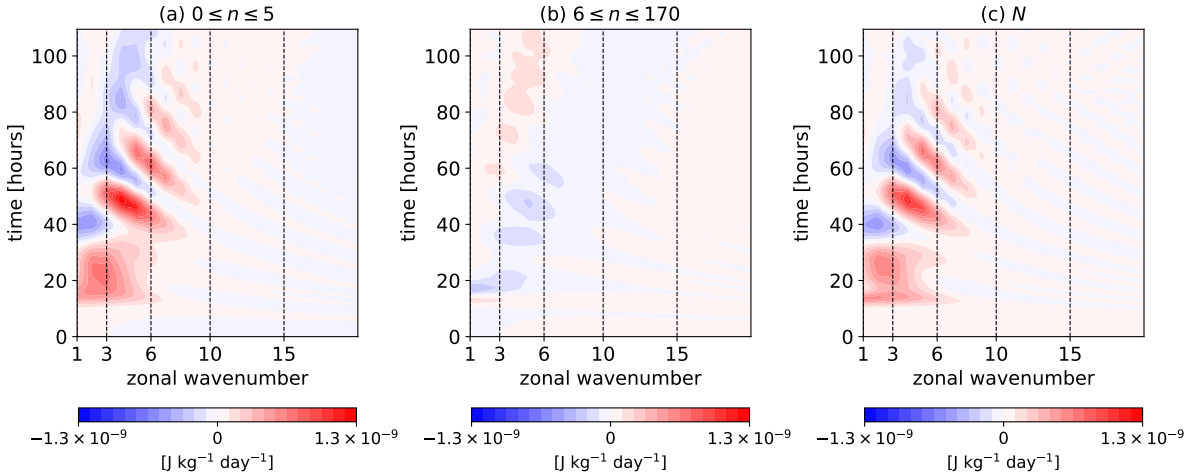


**Figure 3.4.** Evolution of spectral energy tendencies of the MRG wave as a function of zonal wavenumber in the NL SYMFOR-ASYJET experiment with  $D = 400$  m. The MRG wave energy tendency is partitioned into the contributions by (a) low meridional modes - mean state interactions and (b) high meridional modes - mean state interactions, (c) tendencies due to all interactions including wave-mean flow and wave-wave interactions. For every  $n$ , all  $k > 0$  are included in the summation.

waves with low meridional wave indices have a crucial role in the MRG wave excitation process. This is further confirmed by Figure 3.4 for the nonlinear SYMFOR-ASYJET simulation with  $D = 400$  m, which shows separately the MRG wave spectral energy tendencies (Equation A2.8 in Appendix A) due to wave-mean flow interactions involving low meridional modes  $0 \leq n \leq 5$  and modes with high meridional indices  $6 \leq n \leq 170$ . While IG modes are the first to reach the jet, thus initiating the interactions, the Rossby mode - mean flow interactions become more relevant after about 40 hrs of simulation in case of  $D = 400$  m. Similarly, perturbations from midlatitudes or locally imposed perturbations on the jet can excite an MRG wave signal depending on the choice of  $D$ , but the amplitudes of the excited waves are much smaller than in the case of perturbations emanating from tropical heating. This is due to the fact that interactions involving low meridional modes (e.g., the  $n = 1$  Rossby mode) project the strongest onto MRG waves.

### **MRG wave scale selection due to different mechanisms**

The results presented so far show that the generated MRG waves have the peak signal at large synoptic scales. Now I investigate which processes contributing to the MRG energy growth are responsible for the scale selection. For this, I analyse the energy tendency equation (Equation A2.8 in Appendix A) in the nonlinear ASYMFOR-ASYJET simulation. The tendency is partitioned into the contribution by the external forcing, wave-mean flow and wave-wave interactions. The results are shown in Figure 3.5 as absolute MRG energy tendency spectra, which confirms that wave-mean flow interactions play a dominant role in the MRG wave scale selection as they are characterized by a well-defined spectral peak that is located at  $k = 3 - 5$ . The forcing, which is Gaussian, makes the total spectrum more flat at scales  $k < 15$  and its amplitude for the selected model setup exceeds that of the wave-mean flow interactions. The contribution of wave-wave interactions is approximately 3 orders of magnitude smaller than that of the other two mechanisms. However, tendencies due to wave-wave interactions exceed the wave-mean flow interactions' tendencies at small scales. This happens only for  $k > 70$  scales, which are energetically unimportant compared to large and synoptic scales.

Sensitivity of the results to the amplitude and scale of the forcing and to the timescale of the damping was addressed by performing series of simulations varying various model and forcing parameters. Figure 3.6 illustrates that wave-wave interactions do not play a significant role, even when the forcing is 10 and 100 times stronger (i.e., equivalent to 25 and 250 K/day heating rate, respectively) compared to the setup of SYMFOR-ASYJET NL simulation in which the heating rate was only 2.5 K/day. Although the importance of wave-wave interactions increases with the forcing strength, their amplitude at large scales is two orders of magnitude smaller than the amplitude of wave-mean flow interactions even for 100 times stronger forcing.

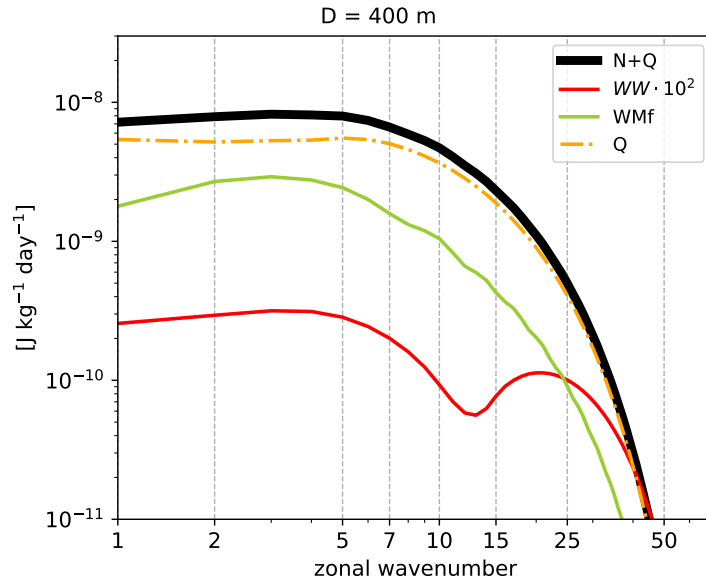


**Figure 3.5.** Spectra of absolute tendency of MRG waves decomposed into contribution by the forcing (Q), wave-mean flow (WMf) and wave-wave (WW) interactions from the nonlinear ASYMFOR-ASYJET experiment. The black curve denotes total absolute MRG wave tendency spectrum (N+Q). In this simulation an asymmetric forcing and an asymmetric jet profile was used.

Increasing the linear damping timescale from 5 to 10 days also does not affect the MRG wave excitation and the growth process, since wave-mean flow interactions still remain 3 orders of magnitude larger even for the increased damping. Furthermore, neither the horizontal scale nor the latitude of the forcing affects the dominant MRG wave excitation mechanism, i.e. wave-mean flow interactions and scale selection. Simulations with varying zonal and meridional scales of the forcing showed that both of these scales affect the amplitude of the excited MRG wave. Only a very large zonal scale of the forcing (e-folding scale  $> 60^\circ$ ) such as the ITCZ-like forcing, was found to influence the dominant scale of the excited MRG wave by shifting it to smaller zonal wavenumbers. Last, it was also found that the observed spectral peak in the MRG wave energy spectra is somewhat sensitive to the averaging period and evolves with time. Nevertheless, the local maxima in the MRG wave energy spectra are always attributed to the wave-mean flow interactions. Furthermore, as  $D$  rises, the relative importance of these interactions increases and can even exceed the amplitude of energy tendencies due to the forcing at large scales.

Two earlier studies of nonlinear MRG wave excitation can be contrasted to the proposed new mechanism. First, Itoh and Ghil (1988) suggested the combination of nonlinear wave-CISK and lateral boundary forcing to generate MRG waves with the observed scales. In their theory wave-CISK initiates the MRG wave excitation along with other equatorial waves, however,

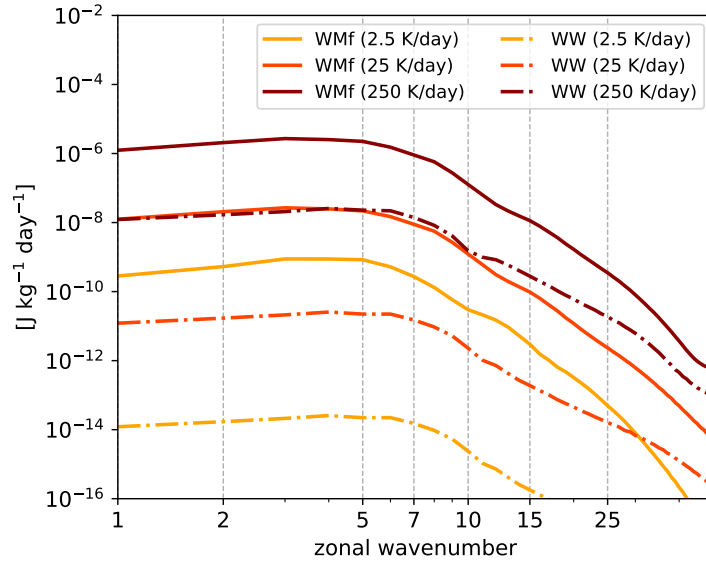


**Figure 3.6.** Absolute spectral energy tendencies of the MRG waves in the NL SYMFOR-ASYJET simulation with  $D = 400$  m and forcing amplitude equivalent to 2.5, 25 and 250 K/day heating rate (dark yellow, orange and dark red curve, respectively). The contributions by wave-wave and wave-mean flow interactions are denoted WW and WMf, respectively. Energy tendencies are averaged over three days.

asymmetry through boundary forcing is needed to reinforce the MRG wave signal. They also suggested that there may be enhanced MRG wave activity in the summer and winter season when the midlatitude westerlies in the winter hemisphere are intensified. Due to inclusion of lateral boundary forcing, their mechanism requires certain properties of extratropical flows to maintain. Here a different mechanism is demonstrated, where MRG wave growth is promoted by wave-mean flow interactions that are local to the tropics and do not require any extratropical input. The presented new mechanism is also coupled to tropical convection, since strong convective signal is needed to maintain wave-mean flow interactions. The second study, which is relevant to discuss is by Raupp and Silva Dias (2005) who showed MRG wave excitation by wave-wave interactions in a similar model setup as considered here. In their simulations with an equatorial  $\beta$ -plane shallow water model, the initial state was prepared using an off-equatorial stationary heat source and they observed strong MRG wave development, provided IG waves were suppressed in the model. In the TIGAR experiments, an asymmetric heat source leads to the growth of MRG waves directly regardless of the presence of the IG waves. Moreover, suppressing IG modes in TIGAR does not significantly alter the contribution of wave-wave interactions to MRG wave tendencies (not shown); i.e. wave-wave interactions are negligible compared to the wave-mean flow interactions and the excitation process by the external forcing.

As a final aspect of MRG wave excitation, I present the results of the TIGAR simulations applying the background zonal mean zonal winds derived from ERA5 for the boreal spring and summer seasons, as listed in Table 3.1. The first goal is to verify the conclusions based on the idealised background jets in a more realistic setting. The second goal is to quantify to what extent the observed asymmetry affects the MRG wave excitation process. As discussed in Section 3.1.1, the JJA season has a higher asymmetry than the MAM season, which is based on the energy in asymmetric  $k = 0$  balanced Rossby modes.

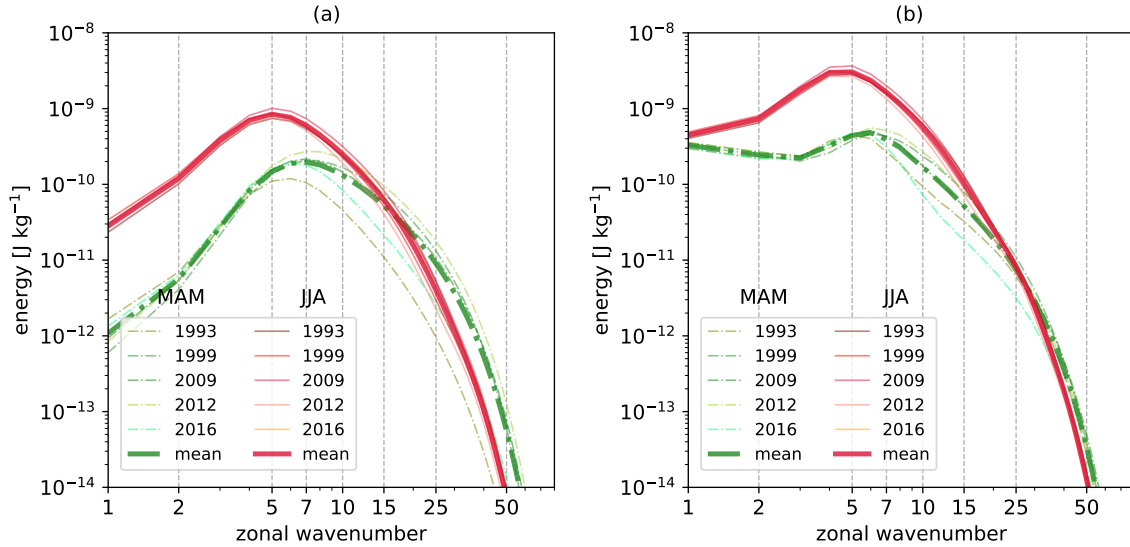


**Figure 3.7.** Energy spectra of the MRG waves in simulations with realistic (i.e. ERA5) background zonal wind and a) symmetric and b) asymmetric forcing. The averaging period is 3 days. Thin and thick curves denote the individual simulations and the means over JJA and MAM cases, respectively.

The results are summarised in Figure 3.7 showing that MRG waves are generated in all simulations just like in the idealised case. As barotropic instability was not excited in any of the realistic simulations, the MRG wave excitation is only a result of wave-mean flow interactions and/or direct excitation by the asymmetric external forcing. It is important to note that there is significant difference in the evolution of the MRG wave energy depending on the asymmetry of the background zonal wind. The more asymmetric profiles produce more energetic MRG wave signals, which applies to all profiles from the JJA season and is valid for both the symmetric and asymmetric forcing cases. It is also clear from Figure 3.7b that the asymmetric forcing greatly increases the large-scale part of the MRG wave energy. In this case, the MRG wave energy at  $k = 1$  is far less sensitive to the flow asymmetry; that is, the MRG wave energy at planetary scales in JJA and MAM is more similar. Overall, there is more MRG wave energy in the simulations with asymmetric forcing at every  $k$ , and in JJA simulations compared to MAM

cases for  $k < 20$ . Another important feature is that all spectra have peak energy at synoptic scales similar to the idealised simulations. For the symmetric forcing, the dominant MRG wavenumber is  $k = 5$  in JJA and  $k = 7$  in MAM. These peak scales are little affected in the simulations with the asymmetric forcing which, as already discussed, leads to the excitation of MRG waves across large scales in both seasons. These findings are also robust to the choice of the forcing parameters (e.g., the central latitude, amplitude and the horizontal scales of the forcing), which further highlights the importance of wave-mean flow interactions in the excitation of the MRG waves.

To answer the research questions of Section 1.5, I demonstrated by idealised numerical simulations that interactions between waves emanating from a symmetric tropical heat source and an asymmetric subtropical zonal jet can excite MRG waves, which have variance spectra resembling the observed MRG waves in the tropical troposphere. By comparing MRG wave energy tendencies from different processes, it was found that wave-wave interactions have negligible impact on MRG wave growth compared to wave-mean flow interactions and direct excitation by the tropical heat source. It was also shown that the asymmetric heating contributes to the generation of large-scale MRG waves thereby causing the MRG wave energy spectrum flat, whereas wave-mean flow interactions peak at synoptic scales, thus the latter process is responsible for the MRG wave scale selection. Simulations using background states derived from ERA5 also underscore the significance of wave-mean flow interactions and reveal that the mean flow asymmetry (i.e. the energy in asymmetric mean states) is important for the amplitude of MRG waves: the larger the asymmetry is, the larger the MRG wave energy.

## **3.2 Scale separation of upper tropospheric and upper stratospheric MRG waves by wave-mean flow interactions**

This section addresses research questions 3-4 from Section 1.5. Here I argue that the origin of the different MRG wave kinetic energy spectra in the upper troposphere and upper stratosphere (Figure 1.3) can be explained by the proposed MRG wave excitation mechanism, i.e. by wave-mean flow interactions. This mechanism explored advantages of a nonlinear spherical Hough-function based shallow water model, TIGAR. The same modelling framework is applied here with no forcing and dissipation. Two sets of numerical experiments are conducted: the first set considers background flows of the upper troposphere and the upper stratosphere derived from ERA5 designed to show that wave-mean flow interactions reproduce MRG wave energy spectra with the observed scales in the two regions. Furthermore, a series of idealised simulations was conducted to elucidate how the latitudinal position of the jet relative to the equator defines the dominant MRG wave scales.

### **3.2.1 MRG wave scale selection in simulations representative of the upper troposphere and the upper stratosphere**

Here I discuss the TIGAR simulations run with realistic zonal wind profiles. The initial conditions include a geostrophically balanced zonal background flow and a Gaussian height perturbation acting as a wave source. The wave source is located at the equator and generates a red spectrum of IG and Rossby waves, but not the MRG waves. The background flow is the ERA5 zonal mean zonal wind from the DJF season at 200 hPa and 1 hPa averaged for the years 2006-2020. This defines two TIGAR simulations, TROPO and STRATO for 200 hPa and 1 hPa level, respectively. The DJF season was selected, which coincides with the MRG wave variance peak both in the upper troposphere and the stratosphere (Figure 1.3). Using the background flows from other seasons leads to essentially the same conclusions regarding the MRG wave scale selection.

The mean depths of  $D = 400$  m and  $D = 10$  km are prescribed for the TROPO and STRATO simulations respectively. The two depths correspond to vertical modes that are representative for equatorial wave dynamics in the two regions of interest.  $D = 10$  km corresponds to the barotropic vertical mode; and  $D = 400$  m is an internal baroclinic mode that is associated with deep convection, thus presumed to represent a significant portion of tropical wave variance (Žagar et al., 2022). The barotropic or the Lamb mode is relevant for planetary waves observed in the middle atmosphere as shown for example by Salby (1981) and Hirooka and Hirota (1985). In

both STRATO and TROPO experiments, the eigenfrequencies of the MRG waves are close to the observed values reported by Zangvil and Yanai (1980) and Randel et al. (1990). The Gaussian initial wave source (Equation B15.7 in Appendix B) has a zonal and meridional e-folding scale equal to the equatorial deformation radius, which is  $10.54^\circ$  and  $23.66^\circ$  for the TROPO and STRATO case respectively, and an amplitude of 5% of the applied shallow water mean depth, which guarantees that the perturbation has the same relative strength in all simulations. Such initial perturbations represent waves that are either generated in situ by e.g. a convective forcing (in the case of TROPO simulation) or propagate from lower levels (in the case of STRATO simulation).

The background profiles of TROPO and STRATO simulations are shown in Fig. 3.8a along with the balanced geopotential height profiles. Notice that the tropospheric subtropical jet in DJF is weaker and shifted poleward in the summer hemisphere compared to the winter hemisphere. In comparison, the stratosphere is characterised by much stronger circumpolar westerly and easterly jet in the winter and summer hemisphere respectively.

The MRG wave total (kinetic+potential) energy spectra are presented in Figure 3.8b showing MRG wave energy maxima at planetary scales ( $k = 3$ ) and at synoptic scales ( $k = 6$ ) in the STRATO and TROPO simulations, respectively. These wavenumbers correspond to the peak scales depicted in the ERA5 climatological spectra in Figure 1.3. Besides the peak scales, the simulated spectra are more energetic in the STRATO case than in the TROPO simulation, which is qualitatively similar to the reanalyses and primarily due to the stronger background flow. Since the kinetic energy spectra of MRG waves in STRATO and TROPO has a similar structure as the total energy spectra, they are not shown. The horizontal structure of the excited MRG waves is presented in Figure 3.8 (c)-(d), which illustrates not only the larger zonal but also the larger meridional scale, i.e., the stratospheric MRG waves extend further away from the equator compared to their tropospheric counterparts. This is because of different mean depths that define the equatorial deformation radius, thus the meridional extent of the MRG wave. It can also be noticed that the jet maxima in both simulations are located within the meridional scales of the MRG waves, which is a necessary requirement for the MRG wave growth by wave-mean flow interactions.

By diagnosing wave-mean flow and wave-wave interactions, it is found that the former is the main contributor to the MRG wave growth, similarly as in simulations with tropical heating perturbations (i.e. Section 3.1.2). The wave-mean flow interactions are most active in a relatively small range of  $k$  that is significantly different for TROPO and STRATO. During the MRG wave life cycle, energy is transferred from the symmetric (i.e.,  $n = 1, 3, 5...$ ) Rossby waves to the MRG waves. The symmetric waves mostly originate from the symmetric initial height perturbation.

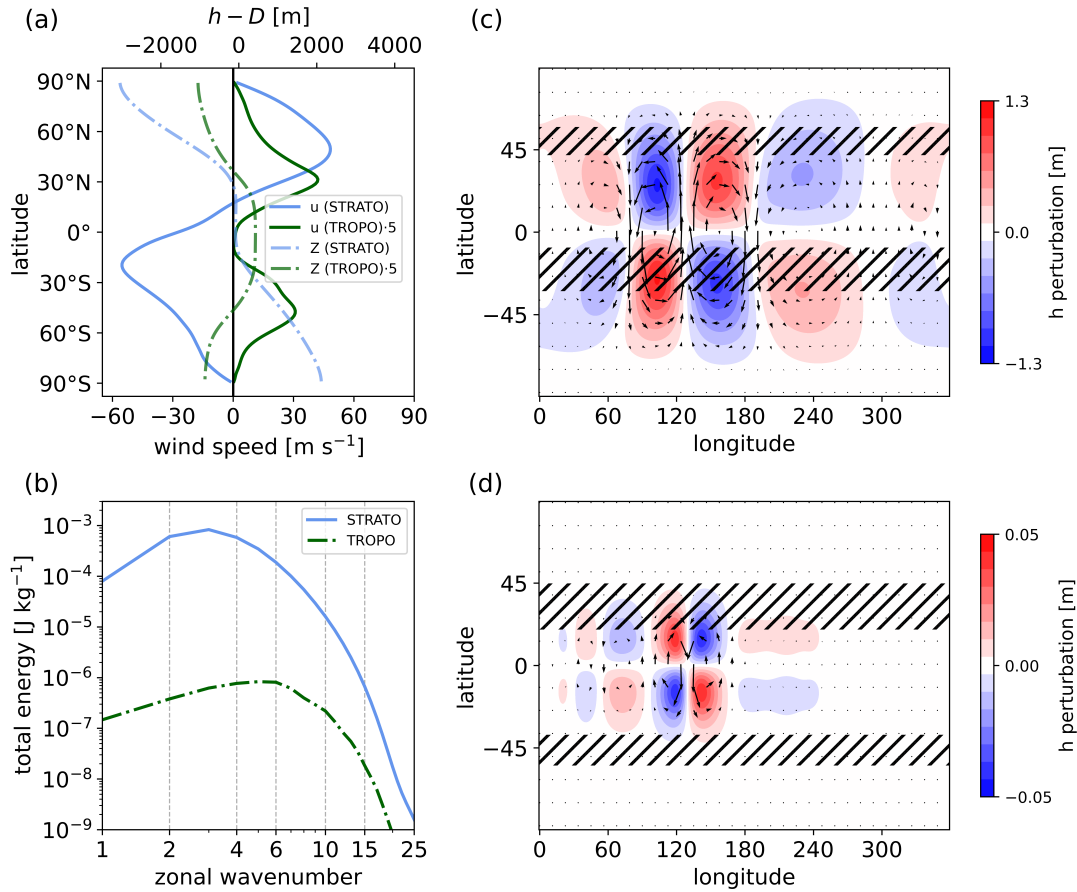


**Figure 3.8.** Setup and results of numerical simulations using the background zonal wind profiles derived from ERA5 at 200 hPa and 1 hPa, denoted TROPO and STRATO simulations, respectively. (a) Background zonal flows of TROPO and STRATO. The balanced height fields are shown (dashed curves) as fluid depth perturbation from the mean depth  $D$ . TROPO profiles are multiplied by a factor of 5. (b) MRG wave total energy spectra averaged over the first 2 days of simulation time. (c)-(d) Horizontal structure of the MRG wave geopotential height (shades) and winds (arrows) on day 2 in (c) STRATO and (d) TROPO simulations. Hatches denote the location of the zonal jet amplitude maxima.

With time, new species of symmetric and asymmetric waves are generated through triad (i.e., nonlinear wave-wave) interactions. However, their amplitudes are small within the analyzed time window (2 days), and therefore their contributions to the MRG wave growth are negligible. The mean state is quasi-steady in all simulations, meaning that there is no barotropic instability, which could influence energy flow between the waves and the mean state.

### 3.2.2 The flow parameter driving the MRG wave scale selection

Here I present how the position of the jet influences the zonal scale of MRG waves. For this purpose a series of idealised simulations was performed with the background zonal jet centred at various latitudes. The jet profile is prescribed analytically with central latitude varied between  $10^\circ\text{N}$  and  $50^\circ\text{N}$  (Figure 3.9a). Every simulation applies the same symmetric initial height perturbation as in TROPO and STRATO with the e-folding scales set to  $10^\circ$  and amplitude of 5% of the applied mean depths,  $D = 400$  m and  $D = 10$  km.

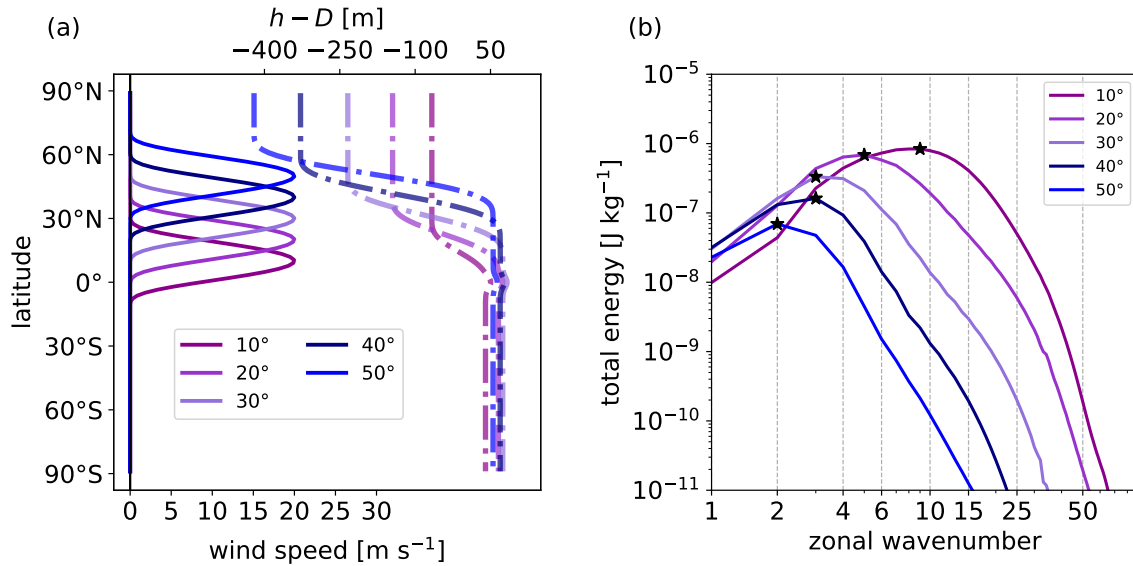


**Figure 3.9.** (a) Latitudinal profiles of the zonal jets centred at  $10^\circ$ ,  $20^\circ$ ,  $30^\circ$ ,  $40^\circ$ , and  $50^\circ\text{N}$  in the idealised TIGAR simulations with  $D = 10$  km. The balanced height fields are also shown (dashed curves) as fluid depth perturbation from the mean depth. (b) MRG wave total energy spectra in response to wave-mean flow interactions involving the idealised jets at different latitudes.

The resulting MRG wave total energy spectra for  $D = 10$  km are combined in Figure 3.9b showing that the most energetic scale of the excited MRG waves depends on the jet position such that the peak scale moves to the smaller zonal wavenumber as the jet shifts poleward. For example, the simulation with the jet centred at  $\varphi = 50^\circ\text{N}$  and at  $\varphi = 10^\circ\text{N}$  excites MRG waves with the largest energy at  $k = 2$  and  $k = 9$ , respectively.

Similar scale shifts are found in the case of  $D = 400$  m (see Figure B6 in Appendix B), except that the MRG wave energy spectra have smaller amplitudes with respect to  $D = 10$  km, especially in simulations with the jet in midlatitudes (i.e. jets centred in between  $40^\circ$  and  $50^\circ$ ). In these simulations the MRG wave energy spectra also becomes red in contrast to  $D = 10$  km. This is because the meridional MRG wave scale is more bounded to the equator as  $D$  reduces, meaning that wave-mean flow interactions in midlatitudes occur too far away with respect to the

meridional scale of the MRG wave. Furthermore, a longer time is needed for MRG waves to develop spectral peaks in simulations where the jets are located far from the equator. This time is much more shorter for  $D = 10$  km, since the IG waves reach the jet region faster due to the fact that the gravity wave propagation speed is dictated by  $D$ .

More generally, the increase in the zonal scale of the MRG waves with the poleward movement of the jet is associated with the meridional scale of the spherical MRG waves, which depends both on  $k$  and  $D$  (Boyd, 2018; Paldor et al., 2018). In the limit of small values of the Lamb parameter  $\varepsilon = (2a\Omega)^2 / (gD)$ , where  $g$ ,  $a$ , and  $\Omega$  stand for gravity, radius of the Earth and Earth’s rotation rate, the meridional scale of the MRG wave reduces with increasing zonal wavenumber (Paldor et al., 2018) implying a stronger equatorial trapping. This wavenumber effect is especially true for mean depths larger than 400 m (see Section B15.4 of Appendix B). Therefore, wave-mean flow interactions cannot project on small-scale MRG waves when the jet is located in midlatitudes, which leads to the dominance of planetary-scale MRG waves. In contrast, when the jet is closer to the equator, the interactions project stronger on smaller-scale MRG waves. The dependence of the MRG wave meridional scale on  $k$  is a crucial factor for the MRG scale selection, which is only a feature of spherical MRG waves (Boyd, 2018; Paldor et al., 2018). A relative sparseness of idealised studies of equatorial waves using a spherical approach may explain why the mechanism of the MRG wave scale selection has remained elusive for so long. Had this study been performed with an equatorial  $\beta$ -plane shallow water model, the jet position would not have been detected as an important factor for the MRG wave scale selection.

**Table 3.2.** Derived jet positions of 200 and 1 hPa for the Northern and the Southern Hemispheres (NH and SH respectively) in different seasons. The values shown with red denote the stronger jet in each season.

	200 hPa		1 hPa	
	NH	SH	NH	SH
<b>JJA</b>	42.2°	<b>30.2°</b>	29.0°	<b>49.3°</b>
<b>DJF</b>	<b>31.7°</b>	40.2°	<b>51.9°</b>	20.9°
<b>SON</b>	38.2°	<b>31.7°</b>		
<b>MAM</b>	<b>31.4°</b>	33.6°		

To further connect the results of idealised simulations with observational data, Table 3.2 shows the central latitudes of jets calculated from daily ERA5 data during 15 years by finding local maxima in the zonal mean zonal wind field in each hemisphere. The jet positions were derived in different seasons from 200 and 1 hPa for both hemispheres. Details of the computations

are given in Section B15.5 of Appendix B. According to Table 3.2 the position of the stronger jet among the two hemispheres, which controls the MRG excitation scale, is around  $31^\circ$  in the upper troposphere, whereas in the upper stratosphere it is near  $50^\circ$  in DJF and JJA. The observed MRG waves shown in Figures 1.4 and 1.5 have meridional extents that are wide enough for the onset of wave-mean flow interactions both in the upper stratosphere, and in the upper troposphere especially in the seasons of DJF and JJA. Thus, the climatological positions of the tropospheric and stratospheric jets and the observed MRG wave meridional scales support the wave-mean flow interaction mechanism as responsible for the planetary-scale ( $k = 2 - 3$ ) MRG waves in the upper stratosphere and the synoptic-scale ( $k = 5 - 6$ ) MRG waves in the upper troposphere.

As presented earlier, the idealised TIGAR simulations require a wave source to produce initial perturbations for the wave-mean flow interaction process. Such perturbations have likely different sources in the upper troposphere and stratosphere. Equatorial waves excited by convective sources in the troposphere have been well studied theoretically (e.g., Salby and Garcia, 1987; Garcia and Salby, 1987), in observations (e.g., Hayashi, 1971; Wheeler and Kiladis, 1999) and models (e.g., Kasahara, 1984; Raupp and Dias, 2009) and they may travel sufficiently far away from the equator to trigger the wave-mean flow interactions. In the upper stratosphere, initial perturbations may arrive as vertically-propagating waves from the troposphere or be generated in situ. For instance, shear instabilities in the stratosphere can lead to gravity wave generation, which can propagate upward (Bühler and McIntyre, 1999; Yasui et al., 2018). Furthermore, only the symmetric source was considered in order to exclude the direct MRG wave excitation by asymmetric forcing (Holton, 1972). As demonstrated in Figure 3.5, such a forcing leads to a nearly flat MRG wave energy spectrum across large scales and makes it more difficult to identify the part of the wave signal due to wave-mean flow interactions in reanalysis data.

In summary, I demonstrated that the position of the jet with respect to the equator controls the scale of MRG waves excited by wave-mean flow interactions. Idealised simulations with the observed zonal wind profiles of the upper troposphere and the upper stratosphere, as well as MRG wave and zonal wind observations support the synoptic and planetary scale MRG wave generation by wave-mean flow interactions in the upper troposphere and the upper stratosphere, respectively.

### 3.3 Role of barotropic instability in the growth of mixed Rossby-gravity waves in the stratosphere

This part of the thesis addresses research questions 1-3 from Section 1.6. First, I discuss the potential for barotropic instability during the westerly and the easterly QBO phases over a long analysis period. This will be followed by showing results from idealised barotropic instability simulations performed with TIGAR to demonstrate how MRG waves are intensified by barotropic instability. Last, I present unstable eigenmodes of the 30 hPa flow over a 10-year period to prove that MRG wave growth is favoured during the westerly QBO phase, which explains the observed MRG wave kinetic energy variability during the QBO phases as demonstrated by Figure 1.6.

#### 3.3.1 Barotropic instability potential during the QBO phases

Here I present statistics for the satisfaction of barotropic instability at the 30 hPa stratospheric level. To isolate the QBO phases and to test barotropic instability directly from the absolute vorticity of the zonal background flow, the 30 hPa zonally averaged zonal wind data from ERA5 (Hersbach et al., 2020) in years 1990-1999 is used.

By applying the Rayleigh-Kuo (RK) (Kuo, 1949) and Ripa's (R83) criterion (Ripa, 1983) for stability conditions of zonal barotropic flows, it is possible to determine how frequently the 30 hPa zonal mean flow favours the conditions for (barotropic) instability in years 1990-1999. According to the RK criterion, the zonal mean flow is barotropically stable when the meridional absolute vorticity gradient expressed by Equation 3.1 obtains the same sign in the whole domain.

$$\nabla Z^* = \frac{1}{2\Omega} \frac{\partial}{\partial \varphi} \left[ f - \frac{1}{a} \frac{\partial \bar{u}}{\partial \varphi} \right] \quad (3.1)$$

In Equation 3.1,  $Z^*$  is the non-dimensional absolute vorticity,  $\bar{u}$  is the zonal mean zonal wind taken from ERA5,  $\Omega$  is the rotation rate of Earth,  $f$  is the Coriolis parameter and  $a$  is the Earth radius.

The R83 stability condition, which is derived on the sphere by using the rotating shallow water equations, reads as

$$\frac{1}{a} \frac{\partial Q}{\partial \varphi} \geq 0 \text{ for all } \varphi \text{ and } \max \left( \frac{\bar{u}}{\cos \varphi} \right) \leq \min \left( \frac{\bar{u} + (g\bar{h})^{1/2}}{\cos \varphi} \right), \quad (3.2)$$

where

$$Q = (\bar{h})^{-1} \left( f - \frac{1}{a \cos \varphi} \frac{\partial \bar{u} \cos \varphi}{\partial \varphi} \right). \quad (3.3)$$

In Equations 3.2 and 3.3  $g$  is the Earth’s gravity constant and we note that the zonal mean fluid depth  $\bar{h}$  is assumed to be in geostrophic balance with  $\bar{u}$ . The R83 condition states that the meridional potential vorticity gradient of the shallow water fluid needs to be non-negative and the maximum of zonal velocity has to be smaller than the local phase speed of long gravity waves in order that the zonal flow maintains stability. Additional details about the separation of the QBO phases is given in Sections C17.2 of Appendix C.

Table 3.3 presents statistics on the violation of both stability conditions of the 30 hPa zonal mean flow in the tropical region ( $\pm 30^\circ$ ) during all timesteps, the easterly QBO (EQBO) and the westerly QBO (WQBO), and in the extratropics ( $30 - 75^\circ$ ). As the instability of the QBO-related circulation is connected to the flanks of equatorial jets, the tropical region was chosen to be wide enough to capture instability of the QBO. This is especially important for the circulation related to the easterly QBO, which often obtains a meridionally extended jet in the tropics (i.e. up to  $30^\circ$ ).

As expected, applying the two stability criteria deliver similar results. It is also noticeable that the tropics are barotropically stable in nearly 40% of the cases, whereas the extratropics are almost always barotropically unstable. There exist also a significant difference between the QBO phases with 2 times more occurrence of barotropic instability in the tropics during the westerly QBO phase. The instability of the westerly QBO jet has also been highlighted both in modelling and observational studies (Shuckburgh et al., 2001; Garcia and Richter, 2019), however, long-term analysis for the instability of the QBO phases has not been established before.

**Table 3.3.** Occurrence of barotropic instability (in %) at 30 hPa in 1990-1999 based on the RK and R83 criterion in the tropics ( $\pm 30^\circ$ ) in all analysed dates, during the EQBO and the WQBO phase, and in the extratropics (in latitude zones of  $30 - 75^\circ$ ).

	tropics	tropics EQBO	tropics WQBO	extratropics
<b>RK</b>	60.6%	36.4%	82.1%	99.2%
<b>R83</b>	62.2%	34.9%	74.5%	96.6%

### 3.3.2 Sensitivity of MRG wave growth to barotropic instability in idealised simulations

This section provides numerical evidence for the connection between MRG wave growth and barotropic instability. In particular, it will be shown how MRG waves intensify as a result of barotropic instability development of QBO-like equatorial jets in idealised numerical simulations conducted with the TIGAR model (Vasylkevych and Žagar, 2021).

The idealised simulations consider a geostrophically balanced zonal flow and an initial perturbation. The background flows include a westerly and an easterly zonal jet (Wjet and Ejet respectively) centred at  $2.5^\circ\text{N}$  with a maximum amplitude of  $23\text{ m/s}$  (see Figure 3.10a). Both the Wjet and the Ejet satisfy the RK and the R83 criterion for barotropic instability. Note that the jet profiles are designed to mimick the zonal circulation representative of the QBO phases while having the same structure. The initial perturbation acts as a wave source exciting barotropic instability development of the jets. More details of the experimental setup are given in Section C17.1 of Appendix C.

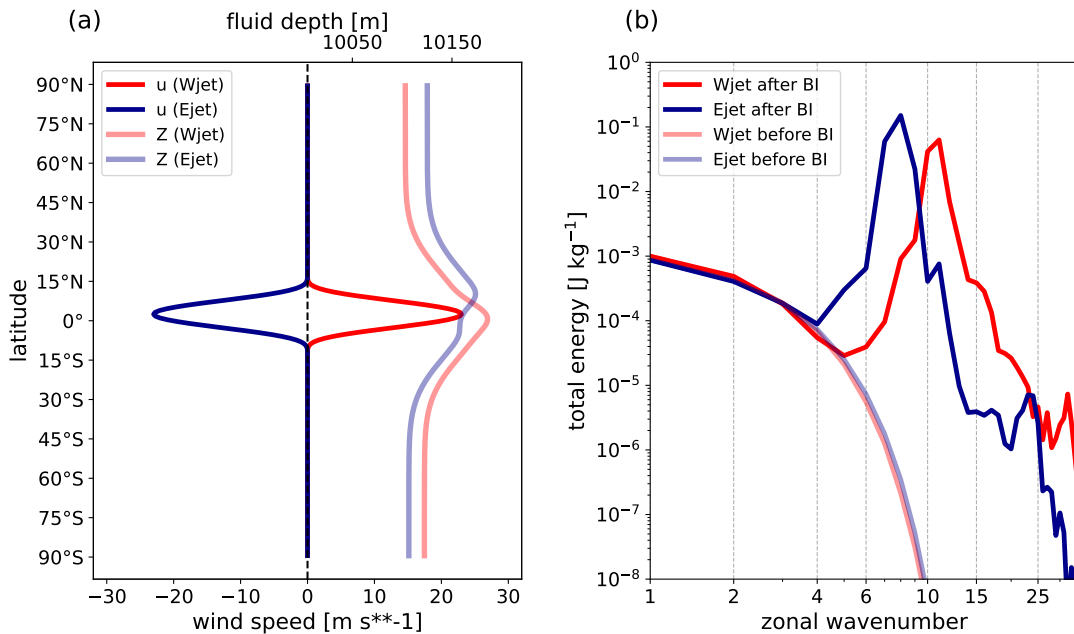


**Figure 3.10.** (a) Initial zonal wind and fluid depth field (bright and blurred curves respectively) of the idealised Ejet and Wjet simulations (blue and red, respectively). (b) MRG wave energy spectra of the Wjet and Ejet simulations. Dull and bright curves show spectra before and after the barotropic instability (BI) development of the jets, respectively.

The MRG wave energy spectra before and after the barotropic instability development of Ejet and Wjet simulations are shown by Fig. 3.10b. First of all, MRG waves are instantly

excited by the initial perturbation, which is asymmetric, however, rapid growth of MRG waves are observed following the barotropic instability development of the equatorial zonal flow. The instability development causes the initial red MRG wave energy spectrum to increase by 3-4 orders of magnitude and to develop peaks in synoptic scales. The zonal wavenumbers characteristic to the instability development are at  $k = 8 - 13$  for Wjet and at  $k = 6 - 9$  for Ejet, which are also matching with the most unstable (i.e. the fastest growing) eigenmodes of the shallow water system linearized around Wjet and Ejet (not shown).

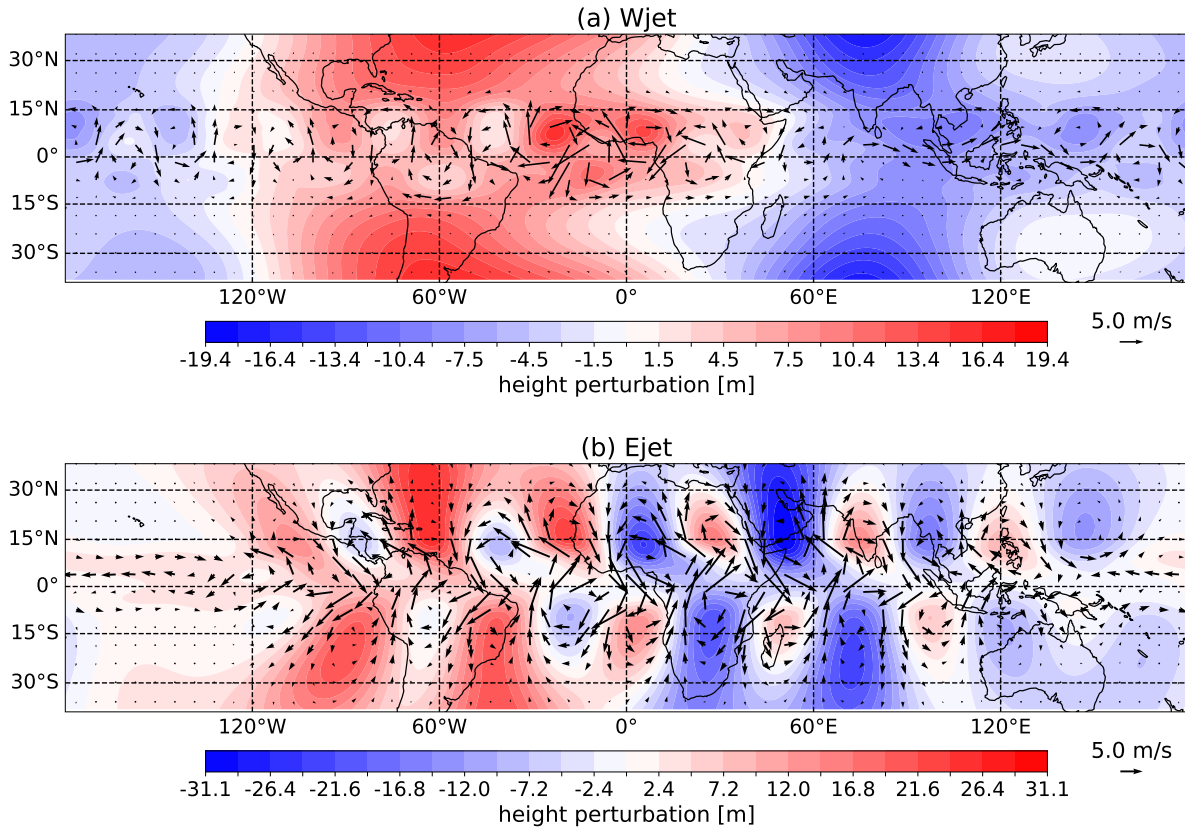


**Figure 3.11.** Rossby wave field (including MRG waves) after barotropic instability development of (a) Wjet and (b) Ejet. The shading and the arrows denote the height and the horizontal wind perturbation due to all Rossby waves.

To demonstrate the strength of the MRG wave signal caused by instability, Figure 3.11 shows the Rossby wave field including all Rossby and MRG modes with  $k > 0$  succeeding the breakdown of the equatorial jets due to barotropic instability. Figure 3.11 clearly demonstrates prominent MRG wave-like structures with strong cross-equatorial flow and asymmetric height perturbations both in the Wjet and in the Ejet simulations. However, the MRG wave signal is stronger in case of Ejet, which is due to the earlier excitation of barotropic instability with respect to simulation time compared to Wjet. It is also found that MRG waves contribute up to

50% and 25% to the Rossby wave field in case of Ejet and Wjet, respectively. This indicates that any equatorial jet undergoing barotropic instability development will produce vortices crossing the equator with sufficiently large projection onto MRG wave structures, thereby MRG wave growth can indicate excitation of barotropic instability in the QBO region.

### 3.3.3 Unstable modes and MRG wave growth in the QBO region

Here I present results following a long-term analysis of the eigenmodes of the shallow water system linearized around the 30 hPa zonal mean flow (i.e. background eigenmodes), which is done by the BGHough software (Section 2). This framework allowed to investigate the barotropic instability of the QBO region, the relation between unstable eigenmodes and MRG wave growth as well as the horizontal scales (i.e., the zonal wavenumbers) sensitive to barotropic instability development of the QBO region.

The unstable eigenmodes were computed for 5-day timesteps within the period of 1990-1999 for zonal wavenumbers  $k = 1 - 12$ . For the analysis, I took into account only the first and second fastest growing modes per zonal wavenumber and per date during the 10-year analysis period, since other unstable background eigenmodes have negligible growth exponents compared to the first two most unstable ones.

The background eigenmodes can contain significant amounts of MRG waves. To quantify the MRG wave content of a growing background eigenmode, the parameter  $E_{MRG}$  is introduced, which is defined as the ratio of the MRG wave energy and the total energy of the background eigenmode. Based on idealised barotropic instability experiments (Section 3.3.2) one would expect a significant growth of MRG waves when the QBO region is barotropically unstable, meaning that eigenmodes representative of barotropically unstable equatorial flow ought to obtain a large  $E_{MRG}$ . Indeed, in some cases  $E_{MRG}$  of the most unstable background eigenmodes is high, for example as in the case shown in Fig. 3.12, which depicts the horizontal structure of the fastest growing mode of  $k = 9$  representative of the westerly QBO phase. Notice that the presented eigenmode is very similar to MRG waves in the tropical region, which is comprised about 60% of MRG waves manifesting that the the QBO region (especially the northern flank of the QBO jet) is barotropically unstable on this date.

Fig. 3.13 depicts the distribution of  $E_{MRG}$  in zonal wavenumber and time for the first two fastest growing modes along with the QBO phases. The most remarkable feature is that during the westerly QBO phase significantly more energy is related to the MRG mode. This means that when barotropic instability is excited during the westerly phase, there will be plentiful energy growth related to MRG waves in stark contrast with the easterly phase. The largest differences of  $E_{MRG}$  between the QBO phases occur at  $k = 11 - 12$  with approximately 13 and 7 times larger

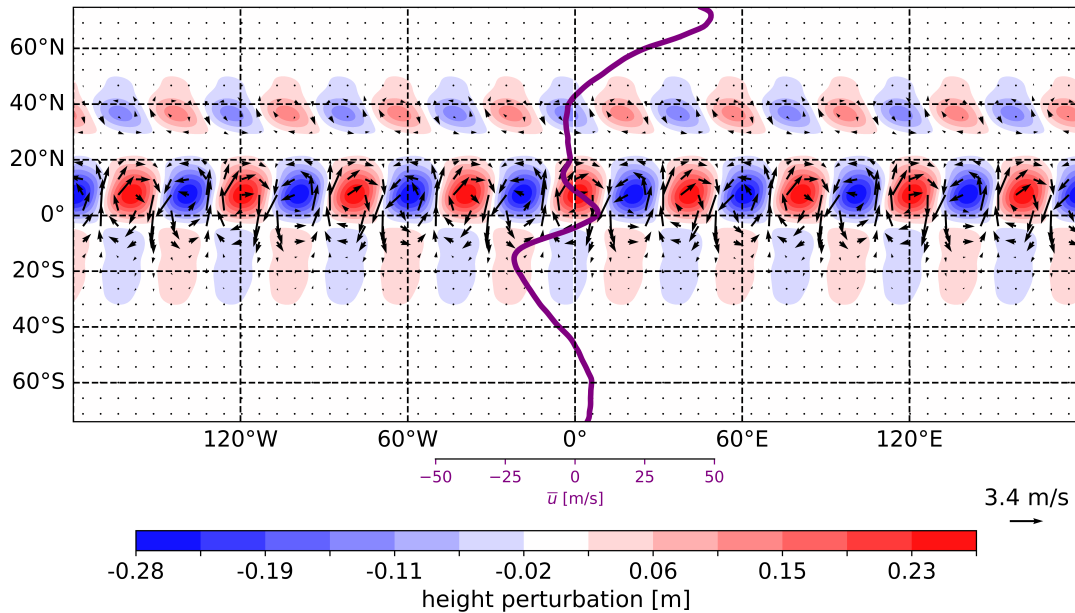


**Figure 3.12.** Horizontal structure of the most unstable background eigenmode of  $k = 9$  in 1990-03-02 (during WQBO). The period of the eigenmode is 3.5 days. The dimensional growth rate is 32 days. The MRG mode contributes about 60% to the background eigenmode. The rest of the eigenmode energy is given by Rossby modes. Shades denote the fluid depth perturbation. The arrows stand for the horizontal wind perturbation. The purple line shows the zonally averaged zonal wind from the same date.

$E_{MRG}$  during the westerly QBO. Furthermore, due to the smallness of  $E_{MRG}$ , the MRG wave development by barotropic instability is expected to be negligible at large scales ( $k = 1 - 5$ ). On the contrary, synoptic and subsynoptic scales ( $k = 6 - 12$ ) are sensitive to barotropic instability of the QBO flow.

The growth exponents ( $\Im[\sigma]$ ), on the other hand, follow the seasonal variations of the mean flow (not shown), therefore they are not related to the QBO phases. The maximum growth occurs during boreal summer (JJA), which concurs with the maximum intensity of the Southern Hemispheric polar night jet that is the fastest zonal circulation at the 30 hPa level. This indicates that the magnitude of the growth exponents are proportional to the absolute strength of the zonal circulation. Regarding the QBO phases, it is found that on average the growth rates are somewhat larger during the easterly QBO, which is due to stronger mean flow in absolute terms compared to the westerly QBO.

There is also a significant difference between the growth rates of eigenmodes with barotropic instability originating in the tropics and outside the tropics. It was found that eigenmodes with large  $E_{MRG}$  (i.e. with strong barotropic instability conditions in the tropics) have growth exponents an order of magnitude smaller than eigenmodes with instability occurring

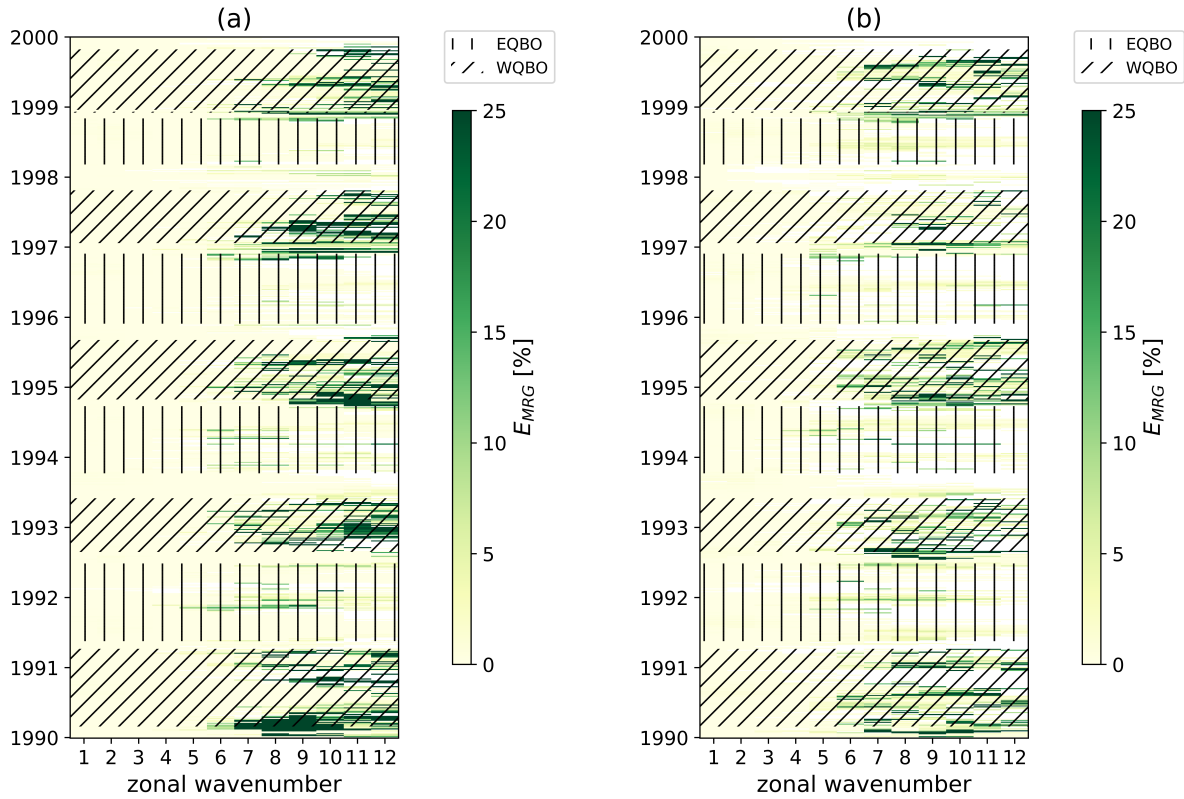


**Figure 3.13.** MRG wave energy ratio ( $E_{MRG}$ , expressed in %) of the (a) first and (b) second fastest growing modes with respect to zonal wavenumber and time. The data corresponding to the QBO easterly and westerly phases are illustrated by the hatches.

primarily in the extratropics, i.e. low values of  $E_{MRG}$ . This is in agreement with the findings of Paldor et al. (2021), who studied the growth rates of barotropically unstable equatorial and midlatitude jets. The smallness of the growth rates related to the QBO flow challenges the diagnosis of MRG wave growth by instability from real data. Another complicating feature is that the most unstable eigenmodes beyond  $k = 4$  have multiple local maxima in their horizontal structure, which means that both the tropical and the extratropical mean flows are barotropically unstable simultaneously. This indicates that when unstable modes are excited, not only MRG waves will grow but also extratropical Rossby waves that can penetrate into the tropics. On the contrary, for large scales ( $k = 1 - 4$ ), barotropic instability is almost exclusive to the extratropics, meaning no large-scale MRG wave growth by instability.

Last, Figure 3.14 presents the percentage of the dates with a non-zero growth exponent for zonal wavenumbers 1-12. The occurrence of positive  $\Im[\sigma]$  gradually decreases with  $k$ , and it is higher during the QBO phases compared to all analysed dates containing dates without a dominant QBO. The difference between the QBO phases is also significant with larger occurrence

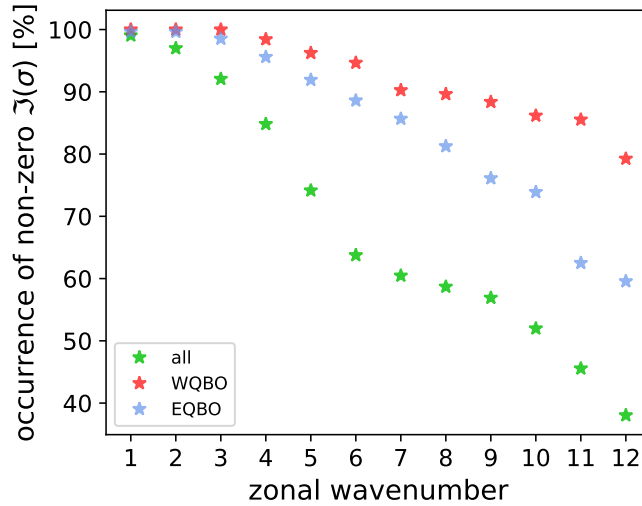


**Figure 3.14.** Percentage of dates with a non-zero growth exponent with respect to zonal wavenumber in case of all considered dates (green), the WQBO phase (red) and the EQBO phase (blue). The analysis period is 1990-1999 with 5-day timesteps.

of non-zero growth rates during the westerly QBO beyond  $k = 2$ , which is in agreement with the instability potential results derived by the RK and R83 stability criteria (Section 3.3.1).

The presented results suggest local MRG wave generation associated with the instability of the QBO. First, the idealised TIGAR simulations proved that MRG waves are sensitive to barotropic instability development of equatorial zonal flows mimicking the circulation of the QBO. It was also demonstrated that there is higher potential for barotropic instability during the westerly QBO phase, as well as the unstable modes representative of the westerly phase contain significantly higher MRG wave energy compared to the easterly phase. This indicates that MRG waves are expected to grow more intensely during the westerly QBO compared to the easterly phase, which explains the MRG wave kinetic energy differences between the two phases depicted in Figure 1.6. It was also shown that synoptic and subsynoptic scale MRG waves are the most sensitive to the barotropic instability development of the QBO jet. However, beyond  $k = 8$  the growth rates become small, which means that the most energetic wavenumbers relevant for the barotropic instability of the QBO are found in range of  $6 \leq k \leq 8$ .

## 4 Conclusions and outlook

This thesis provides new understanding for the generation of mixed Rossby-gravity (MRG) waves in the tropical atmosphere, which are pivotal components of the tropical variability spectrum as they play important roles in many dynamical phenomena observed in the tropics.

There are a number of features of the observed MRG wave variability in the troposphere and the stratosphere that lack physical understanding, for which this thesis offers physical explanation. It is important to highlight that the generation theories proposed for MRG waves do not confidently explain the observed synoptic-scale spectral peak in the upper troposphere. The new mechanism proposed in this thesis, which involves interactions with waves originating from tropical heating perturbations and the asymmetric background flow, provides an alternative explanation for the origin of the synoptic-scale waves in the upper troposphere. The mechanism of wave-mean flow interactions also explains successfully the observed scale separation between upper tropospheric and upper stratospheric MRG waves, which obtain synoptic and planetary scales, respectively. The reason for the scale separation lies in the position of the jet with respect to the equator: midlatitude jets produce large-scale MRG waves (with low zonal wavenumber), whereas jets embedded in the tropics support small-scale (large zonal wavenumber) MRG wave generation, which has not been shown before. The jet positions derived by ERA5 data support the generation theory of MRG waves by wave-mean flow interactions both in the upper troposphere and the upper stratosphere.

Although wave-wave interactions were suggested to be an important process for MRG wave excitation, no proof has been found that they are relevant for MRG wave generation as their contribution to MRG wave growth is negligible compared to tropical heating and wave-mean flow interactions.

In studies concerning middle atmospheric dynamics there has been speculations that MRG waves are produced locally by barotropic instability development of the circulation related to the region of the quasi-biennial oscillation (QBO), which can be more powerful during the westerly QBO phase. For the first time, a long-term analysis proved that the westerly QBO phase has significantly larger potential for barotropic instability compared to the easterly phase. It was also argued that the MRG wave growth is enhanced during the westerly QBO phase,

which is based on the analysis of unstable modes derived by the linearized TIGAR model that incorporated observed background flow conditions. The enhanced potential for barotropic instability development of the westerly QBO phase and the resulting MRG wave growth not only explains the observed MRG wave kinetic energy differences between the QBO phases at synoptic and subsynoptic scales, but also points out that MRG waves are likely to be produced locally in the QBO region instead of propagating from lower levels and providing forcing for the QBO.

The results of the present dissertation have important implications for tropical atmospheric predictability. First of all, the new MRG wave excitation mechanism driven by wave-mean flow interactions highlights the subtropical impact on tropical dynamics and predictability. In particular, the new mechanism suggests that errors related to MRG waves in Numerical Weather Prediction (NWP) systems can stem from the inaccurate background flow representation, particularly the subtropical zonal flow in case of the upper troposphere. The results also help associate different MRG wave scales with different sources of errors. We can assume that in the upper troposphere large-scale MRG wave inaccuracies originate from the incorrect representation of convection, whereas MRG wave-related errors occurring at synoptic scales are likely to be associated with inaccuracies of the subtropical jet. In terms of stratospheric predictability, the MRG wave growth was identified as a useful proxy for the excitation of barotropic instability development of equatorial flows, particularly the QBO region. This thesis also manifests how useful simple atmospheric models and idealised approaches can be for establishing physics-based theories and increasing our understanding of basic atmospheric dynamical features, which is challenging to address with complex atmospheric models that incorporate numerous physical processes. The TIGAR model applied here is a sophisticated tool to investigate atmospheric wave dynamics, as it eliminates complicating factors for wave diagnosis and supports process-based analysis.

Despite the usefulness of the idealised approach for studying MRG wave dynamics in the tropics, a few limiting factors need to be taken into account. First of all, the effect of convection, which has been shown to be coupled to MRG wave dynamics, enters only indirectly into the TIGAR model as external forcing. In more complex models convection and circulation modify each other leading to equatorial wave generation by the so-called wave-convective instability of the second kind (CISK) process that is completely missing in TIGAR. There is also indication that midlatitude wave forcing is important for MRG wave generation, which was not investigated in this thesis. Over the past decades there has been several studies conducted with simplified models to prove the MRG wave excitation by lateral boundary forcing. I am confident that such process could be simulated with TIGAR, however, the condition of quasi-resonance between

the forcing midlatitude wave and the MRG wave is a crude assumption, which the mechanism of wave-mean flow interactions does not require. As TIGAR is a 2D barotropic model, I could not investigate the vertical propagation of MRG waves in realistic 3D atmospheres, which may be important for stratospheric MRG wave variability. The assumption of local MRG wave generation in the stratosphere is only supported by real-time MRG wave forecast data that indicate the lack of MRG wave propagation through the tropopause. Another caveat of the modelling approach is the lack of representation of vertical zonal wind shear, which has been shown to modulate MRG waves (Wang and Xie, 1996). To confirm the assumption of local wave generation and to study the effect of vertical wind shear, 3D atmospheric simulations are needed. Regarding the background eigenmode analysis of the QBO region, an important limitation is the arbitrary choice of the shallow water mean depth (i.e. the barotropic vertical mode) entering into the linearized model. As the QBO is distributed between several vertical modes, and the growth rates are sensitive to the choice of the mean depth (Paldor et al., 2021), this study requires the extension with the inclusion of several vertical modes in the computations of the background eigenmodes.

To overcome the limitations of this thesis and further explore tropical atmospheric dynamics, there are several potential avenues for extending this research. As the direct effect of convection on MRG waves is missing in this thesis, using a moist shallow water model (e.g. Hartney and Bendall, 2024) with the inclusion of moisture budget and interactive convection could be advantageous to study wave-CISK along with other MRG wave excitation mechanisms. It would also be important to study the effect of vertical wind shear and the vertical propagation of MRG waves in a 3D primitive equation model that uses Hough harmonics as spectral expansion basis. Furthermore, the quantification of wave-mean flow interactions projecting onto MRG waves in 3D observational data would be of great interest. As kilometre-scale atmospheric model simulations will be common in the future, investigating the effect of mesoscale phenomena (e.g., fronts, mesoscale convective systems) on MRG waves could yield interesting insights. Last, the extratropical barotropic instability in the stratosphere, which was shown to be a permanent feature, could be interesting to study in terms of sudden stratospheric warming events or extratropical Rossby wave intrusion into the tropics.

# Appendix A: Excitation of mixed Rossby-gravity waves by wave - mean flow interactions on the sphere

This paper has been published in the Quarterly Journal of the Royal Meteorological Society as

- Mahó, S.I., Vasylykevych, S. & Žagar, N. (2024) Excitation of mixed Rossby–gravity waves by wave–mean flow interactions on the sphere. *Quarterly Journal of the Royal Meteorological Society*, 150(762), 2920–2936. Available from: <https://doi.org/10.1002/qj.4742>

## Author contributions

- Mahó S.I. contributed to conceptualization, data curation, formal analysis, investigation, methodology, visualization, writing the original draft and the review.
- Vasylykevych, S. contributed to formal analysis, investigation, methodology, providing the software, supervision, review and editing.
- Žagar, N. contributed to the project administration, conceptualization, methodology, supervision, review, editing and providing the software.

# Excitation of mixed Rossby–gravity waves by wave–mean flow interactions on the sphere

Sándor István Mahó<sup>1</sup>, Sergiy Vasylkevych<sup>1</sup>, Nedjeljka Žagar<sup>1</sup>

<sup>1</sup> Meteorological Institute, Center for Earth System Research and Sustainability,  
Universität Hamburg, Hamburg, Germany

Received: 2 June 2023, Revised: 26 January 2024, Accepted: 24 March 2024

## Abstract

The equatorial mixed Rossby-gravity wave (MRGW) is an important contributor to tropical variability. Its excitation mechanism capable of explaining the observed MRGW variance peak at synoptic scales in the troposphere remains elusive. This study investigates wave-mean flow interactions as a generation process for the MRGWs using the TIGAR model, which employs Hough harmonics as the basis of spectral expansion on the sphere, thereby representing MRGWs as prognostic variables. Idealised numerical simulations reveal the interactions between waves emanating from a symmetric tropical heat source and an asymmetric subtropical zonal jet as an excitation mechanism for the MRGWs. The excited MRG waves have variance spectra resembling the observed MRGWs in the tropical troposphere. The MRG energy spectrum has a maximum at zonal wavenumbers  $k = 4 - 5$  also in the case of an asymmetric forcing that generates MRGWs across large scales. Effects of wave-wave interactions appear of little importance for the MRGW growth compared to wave-mean flow interactions. Application of the zonal-mean zonal wind profiles from ERA5 reaffirms the importance of the asymmetry of the zonal mean flow.

# A1 Introduction

Since Yanai and Maruyama (1966) first discovered mixed Rossby-gravity waves (MRGW or MRG modes) as periodic fluctuations in the meridional wind in the equatorial lower stratosphere, their properties and the associated excitation mechanism have been a subject of numerous studies. Theoretically, the MRGW, also known as the Yanai wave, is a westward-propagating solution of the linearized shallow water equations on the equatorial  $\beta$ -plane (Matsuno, 1966) and on the sphere (Longuet-Higgins, 1968; Paldor et al., 2018). Initially, MRGWs were analysed as free modes (Yanai and Hayashi, 1969; Yanai and Murakami, 1970). Soon however, satellite irradiance data provided evidence that tropospheric MRGWs are coupled to convection (Chang, 1970; Wallace and Chang, 1972; Hendon and Liebmann, 1991; Takayabu, 1994; Bergman and Salby, 1994; Wheeler and Kiladis, 1999). The MRGWs were argued to provide energy for tropical depression type waves over the equatorial Pacific (Takayabu and Nitta, 1993) that can trigger the formation of tropical storms (Dickinson and Molinari, 2002). In addition, their vertical propagation was shown to contribute to the forcing of the easterly phase of the quasi-biennial oscillation (QBO) (Lindzen and Holton, 1968; Alexander et al., 2008). Recent studies also coupled MRGWs with the Hadley cell dynamics (Hoskins and Yang, 2021) and with the initiation of the Madden-Julian Oscillation (MJO) (Takasuka et al., 2019). Observational studies agree about the dominant zonal wavenumbers of 4-5 of the MRGWs and periods of about 5 days (e.g. Yanai and Hayashi, 1969; Yanai and Murakami, 1970; Zangvil and Yanai, 1980).

Early studies on the MRGW excitation in the troposphere applied the adiabatic barotropic or baroclinic models and found that MRGWs are generated by long-period, large-scale tropospheric heating perturbations asymmetric about the equator (Holton, 1972; Silva Dias et al., 1983). While easily demonstrated, this excitation process can not explain the observed scale selection. Other mechanisms that have been studied in depth include the lateral boundary forcing (Mak, 1969), the wave-CISK (conditional instability of the second kind) process (Hayashi, 1970) and the wave interactions (Raupp and Silva Dias, 2005).

The theory proposed by Mak (1969) and refined by Wilson and Mak (1984) states that the scale selection of MRGWs is driven by a linear resonance mechanism that is directly controlled by the properties of the forcing wave exerted at lateral boundaries. Hayashi (1970) argued that instability of the wave-CISK mechanism, which describes interaction between cumulus convection and equatorial wave dynamics, is unstable and can produce MRGWs. However, this mechanism was shown not capable of explaining the scale selection of the MRGWs (Itoh and Ghil, 1988). As an alternative, Itoh and Ghil (1988) suggested a non-linear wave-CISK theory in which the MRGWs are amplified by asymmetric lateral boundary forcing. Nevertheless, the

wave-CISK mechanism and the associated waves were shown to be sensitive to the convection parameterization (Starx, 1976; Hess et al., 1993). Raupp and Silva Dias (2005) suggested equatorial Rossby wave interactions as a generation mechanism for MRGWs. They solved the non-linear shallow-water equations on the equatorial  $\beta$ -plane by a spectral method that used the eigensolutions of the linear problem as the spectral basis. Raupp and Silva Dias (2005) argued that MRGWs were excited by a non-linear mechanism in which first an asymmetric heat source produces a quasigeostrophic basic state, which then supplies energy for the MRGWs with zonal wavenumber 4 and 5.

The present study complements the understanding of MRG waves by showing that they can be excited by interactions of wave perturbations and asymmetric zonal mean flows in the tropics or subtropics. The new excitation mechanism is demonstrated by a hierarchy of numerical simulations using idealised and observed latitudinal profiles of the zonal mean zonal wind. Our modelling system with the recently developed intermediate complexity model TIGAR (Transient Inertia-Gravity And Rossby wave dynamics, Vasylyevych and Žagar, 2021) provides a unique framework for the identification of processes contributing to the MRGW growth.

The remainder of this paper is structured as follows. In Section A2 we describe the model and the hierarchy of numerical experiments. The results are presented in the two sections focusing on the MRG excitation in simulations with idealised (Section A3) and realistic (Section A4) profiles of the background zonal wind. The discussion and conclusions are presented in Section A5.

## **A2 Numerical model formulation and setup**

The recently developed TIGAR model was introduced by Vasylyevych and Žagar (2021). In what follows we recall the model formulation, then we describe the linearized version of TIGAR, which was developed for the purpose of this study. The setup and the list of numerical experiments concludes the section.

### **A2.1 The non-linear TIGAR model**

In the absence of bottom topography, the model equations in spherical coordinates  $(\lambda, \varphi) \in [0, 2\pi) \times (-\pi/2, \pi/2)$  read as follows:

$$\frac{du}{dt} - v \left( 2\Omega \sin \varphi + \frac{u}{a} \tan \varphi \right) + \frac{g}{a \cos \varphi} \frac{\partial h}{\partial \lambda} = -\frac{1}{\tau_R} u, \quad (\text{A2.1a})$$

$$\frac{dv}{dt} + u \left( 2\Omega \sin \varphi + \frac{u}{a} \tan \varphi \right) + \frac{g}{a} \frac{\partial h}{\partial \varphi} = -\frac{1}{\tau_R} v, \quad (\text{A2.1b})$$

$$\frac{dh}{dt} + h \nabla \cdot \mathbf{V} = Q - \frac{1}{\tau_N} (h - D), \quad (\text{A2.1c})$$

where  $d/dt$  is the material derivative,  $\mathbf{V} = [u, v]$  denotes the horizontal velocity vector composed of the zonal ( $u$ ) and the meridional component ( $v$ ),  $h$  is the total fluid depth,  $D$  is the mean depth,  $g$  and  $\Omega$  are the gravity constant and the rotation rate of the Earth respectively,  $a$  is the radius of the Earth. The heat source  $Q$  is modelled as a Gaussian, as explained in Section A2.4. Two other dissipative terms, the so-called Rayleigh friction in the momentum equations and the Newtonian cooling in the continuity equation, are defined by their characteristic time scales  $\tau_R$  and  $\tau_N$ , respectively. Additionally, we apply spectral viscosity similarly as in Gelb and Gleeson (2001) to guarantee realistic energy distribution at the smallest scales while minimally influencing the model physics as discussed in the Supplements.

TIGAR solves Equation A2.1 by applying the Hough harmonics as basis functions for the spectral expansion. The Hough harmonics are the eigensolutions of the linearized rotating shallow-water (RSW) equations (Longuet-Higgins, 1968), and they involve three types of solutions: the eastward propagating inertia-gravity modes (EIG), the westward propagating inertia-gravity modes (WIG), and the low-frequency Rossby modes. The complete set of eigenmodes involves two special equatorial solutions: the westward-propagating mixed Rossby-gravity and the eastward-propagating Kelvin mode, which fill the frequency gap between the slow Rossby and fast inertia-gravity (IG) modes.

The solution of Equation A2.1 in terms of the Hough harmonics was proposed by Kasahara (1977) and TIGAR follows the steps therein. First, we rewrite the RSW equations in dimensionless quantities. The relation between the dimensional and non-dimensional variables is the following:  $\tilde{u} = u/\sqrt{gD}$ ,  $\tilde{v} = v/\sqrt{gD}$  and  $\tilde{h} = h/D - 1$ . The non-dimensional time  $\tilde{t}$  is obtained by multiplying  $t$  by  $2\Omega$ . This is followed by the expansion of  $(\tilde{u}, \tilde{v}, \tilde{h})$  in terms of the Hough harmonics as

$$[\tilde{u}, \tilde{v}, \tilde{h}]^T(\lambda, \varphi, \tilde{t}) = \sum_{|k|=0}^M \sum_{n=0}^{N(|k|)} \sum_{l=1}^3 \chi_{n,l}^k(\tilde{t}) \mathbf{H}_{n,l}^k(\lambda, \varphi), \quad (\text{A2.2})$$

where  $M$  is the truncation limit,  $N(k)$  is defined by the truncation type,  $\chi_{n,l}^k$  is the Hough

expansion coefficient and  $\mathbf{H}_{n,l}^k$  is the Hough harmonic with the zonal wavenumber  $k$ , meridional mode index  $n$  and the type of mode  $l$ . The latter takes values 1, 2 and 3 for the Rossby, EIG and WIG modes, respectively. We remark, that for real fields  $[u, v, h]$ , necessarily  $\chi_{n,l}^{-k} = \left(\chi_{n,l}^k\right)^*$ , thus, in the following, we will consider  $k$  to be non-negative, combining the waves corresponding to  $\pm k$  into one.

The set of Hough harmonics is uniquely (up to a multiplicative constant) defined, except for  $k = 0$  Rossby modes, which are the zonal steady states of the linearized RSW equations. For the latter we use so-called K-modes derived by Kasahara (1978). Among the K-modes we distinguish transient ( $k = 0$  IG) and stationary ( $k = 0$  Rossby) modes. The latter ones have zero eigenfrequencies. The equatorially bounded MRG and the Kelvin waves correspond to  $n = 0$  index for the Rossby ( $l = 1$ ) and EIG ( $l = 2$ ) modes, respectively. The horizontal structures of the MRGW geopotential height and zonal wind field are asymmetric with respect to the equator whereas the equatorially symmetric meridional wind field has the maximum at the equator<sup>1</sup>.

The substitution of the expansion (Equation A2.2) into Equation A2.1 leads to the spectral ODE

$$\frac{d}{d\tilde{t}} \chi_{n,l}^k(\tilde{t}) + i\tilde{\omega}_{n,l}^k \chi_{n,l}^k(\tilde{t}) = f_{n,l}^k(\tilde{t}) \quad (\text{A2.3})$$

for the model prognostic variables  $\chi_{n,l}^k$ . In Equation A2.3  $\tilde{\omega}$  denotes the non-dimensional frequency of the mode  $(k, n, l)$ .

The right-hand side term  $f_{n,l}^k$  in Equation A2.3 contains the contribution of non-linear interactions and forcing as

$$f_{n,l}^k = \frac{1}{2\pi} \int_0^{2\pi} \int_{-\pi/2}^{\pi/2} (\mathbf{N} + \mathbf{Q}) \left( \sum_{k',n',l'} \chi_{n',l'}^{k'} \mathbf{H}_{n',l'}^{k'} \right) \cdot \left( \mathbf{H}_{n,l}^k \right)^* (\lambda, \varphi) d\varphi d\lambda, \quad (\text{A2.4})$$

where

$$\mathbf{N} = -\gamma \begin{bmatrix} \tilde{\mathbf{V}} \cdot \tilde{\mathbf{V}} \tilde{u} - \tilde{u} \tilde{v} \tan(\varphi) \\ \tilde{\mathbf{V}} \cdot \tilde{\mathbf{V}} \tilde{v} + \tilde{u}^2 \tan(\varphi) \\ \tilde{\mathbf{V}} \cdot \tilde{\mathbf{V}} \tilde{h} + \tilde{h} \tilde{\mathbf{V}} \cdot \tilde{\mathbf{V}} \end{bmatrix} \quad \text{and} \quad \mathbf{Q} = \begin{bmatrix} -\frac{1}{\tau_R} \tilde{u} \\ -\frac{1}{\tau_R} \tilde{v} \\ Q - \frac{1}{\tau_N} \tilde{h} \end{bmatrix}. \quad (\text{A2.5})$$

In the shallow water setting, both the properties of linear waves and the scaling ratio between linear terms and non-linearity are controlled by a single non-dimensional quantity  $1/\gamma^2 = (2a\Omega)^2/gD$  (Longuet-Higgins, 1968; Boyd and Zhou, 2008), which is known as Lamb's parameter. Following the so-called U-V formulation by Ritchie (1988), the forcing and non-linear terms,  $\mathbf{Q}$  and  $\mathbf{N}$  respectively, appearing in  $f_{n,l}^k$  are computed pseudo-spectrally, i.e. they are

<sup>1</sup>The horizontal structure of the zonal wavenumber 1 spherical MRGW for the mean depths ranging from 10 km to about 27 meters is shown at <https://modes.cen.uni-hamburg.de/Hough#part2.2>

evaluated in physical space, then transformed to spectral space by applying FFT and Hough expansion in the zonal and meridional directions, respectively. To this end Hough functions and their derivatives are precomputed with high precision from Legendre polynomials; thereby the spectral truncation is the sole source of numerical errors in the evaluation of spectral tendencies. The contribution of interactions between different modes to the spectral tendencies are computed directly in the model by replacing full fields in  $\mathbf{N}$  by the physical space reconstruction of the modes of interest. For further details of the evaluation of the non-linear term  $N$  including the reconstruction of the partial derivatives in gridpoint space the reader is referred to the Supplements.

The above described modelling framework allows us to study the generation of MRG waves on the sphere directly from the model output, since the MRGWs along with other eigenmodes of the linearized system (i.e. the Kelvin waves, inertia-gravity modes and Rossby modes) are prognostic variables represented by a spectral Hough expansion coefficient for each zonal wavenumber. In other words, the MRG wave is defined by the multivariate projection of the geopotential height and horizontal winds onto the spatial structure of the linear mode on the sphere. Another important factor to highlight is the model's ability to separate the dynamical contributions of forcing, linear dynamics, and interactions between separate modes during the model integration. Note that term  $\mathbf{N}$  includes all interactions of the mean state, which correspond to  $k' = 0$ ; thus, we evaluate wave-mean flow interactions from  $\mathbf{N}$ .

## A2.2 The linearized model

The linearized version of TIGAR solves the equations linearized about a prescribed geostrophically balanced mean zonal flow. Separating the model prognostic variables into the zonal mean part (denoted by an overbar) and a perturbation (denoted by ' '),

$$u = \bar{u}(\varphi) + u'(\lambda, \varphi, t), \quad v = v'(\lambda, \varphi, t), \quad h = \bar{h}(\varphi) + h'(\lambda, \varphi, t),$$

the linearized model equations read

$$\frac{\partial u'}{\partial t} - v' 2\Omega \sin \varphi + \frac{g}{a \cos \varphi} \frac{\partial h'}{\partial \lambda} = -\frac{\bar{u}}{a \cos \varphi} \frac{\partial u'}{\partial \lambda} - \frac{v'}{a} \frac{\partial \bar{u}}{\partial \varphi} + \frac{\bar{u}v'}{a} \tan \varphi - \frac{1}{\tau_R} u', \quad (\text{A2.6a})$$

$$\frac{\partial v'}{\partial t} + u' 2\Omega \sin \varphi + \frac{g}{a} \frac{\partial h'}{\partial \varphi} = -\frac{\bar{u}}{a \cos \varphi} \frac{\partial v'}{\partial \lambda} - 2\frac{\bar{u}u'}{a} \tan \varphi - \frac{1}{\tau_R} v', \quad (\text{A2.6b})$$

$$\frac{\partial h'}{\partial t} = -\frac{\bar{u}}{a \cos \varphi} \frac{\partial h'}{\partial \lambda} - \frac{v'}{a} \frac{\partial \bar{h}}{\partial \varphi} - \frac{\bar{h}}{a \cos \varphi} \frac{\partial u'}{\partial \lambda} + \frac{\bar{h}}{a} \frac{\partial v'}{\partial \varphi} + Q - \frac{1}{\tau_N} (h' - D), \quad (\text{A2.6c})$$

which leads to a spectral equation similar to Equation A2.3, where the new terms representing wave-mean flow interactions are incorporated into  $f_{n,l}^k$  that is computed similarly as in the full non-linear model. We remark that we do not apply linear damping to the mean fields in the linearized model, which is why the terms involving  $1/\tau_R \bar{u}$ , and  $1/\tau_R \bar{h}$  are omitted in Equations A2.6. Also,  $Q = Q'$  as we use a localized heat source.

Note that unlike the full non-linear TIGAR, the linearized model does not include wave-wave interactions, which are defined as interactions between the perturbation terms, or in other words interactions between  $k > 0$  Hough modes. In contrast, wave-mean flow interactions account for first order interactions between the mean and the perturbation terms.

The resting state linear model is obtained by setting  $\bar{u} = 0$  and  $\bar{h} = D$  in Equation A2.6. In such a model neither wave-mean flow nor wave-wave interactions are supported. The resting state linear model and the linearized model are referred as LI and LZ, respectively.

### A2.3 Energy diagnostics in modal space

The mechanical energy (in  $J/kg$ ) in mode  $(k, n, l)$  for  $k > 0$  is given by

$$E_{n,l}^k = gD \left| \chi_{n,l}^k \right|^2. \quad (\text{A2.7})$$

The sum of energy components  $E_{n,l}^k$  across all  $k$ ,  $n$  and  $l$  yields the sum of the kinetic and available potential energy of the system linearized around the state of rest (Žagar et al., 2015). Previous studies of the zonal wavenumber energy spectra from reanalyses typically included the MRGW energy among the Rossby wave energy. The comparison of energy levels by MRGWs and other waves by Stephan et al. (2021) showed that the MRGWs contain about 20% of the westward-propagating non-Rossby (i.e. WIG+MRG) wave energy in the troposphere with peak at  $k = 5 - 7$ . Furthermore, the subseasonal variability associated with the MRGWs makes about 1/3 of the subseasonal variability associated with all  $k > 0$  non-Rossby waves (i.e. WIG+EIG+MRG+Kelvin waves). While these numbers are significant, their percentages in the total wave energy (all modes) dominated by the Rossby waves are small. As an example, the energy spectra from the SYMFOR-JJA simulation, shown in Figure A1 demonstrates that TIGAR produces energy spectra that resemble the spectra from more realistic simulations. Notably, the Kelvin wave energy is most energetic at  $k = 1$  (Žagar et al., 2022) whereas the MRGW energy peaks at synoptic scales similar to the spectra from reanalysis data (Stephan et al., 2021).

The second diagnostic is targeted at identifying the role of Hough and K modes' interactions, therefore we evaluate the contribution of the  $\mathbf{N}$  term and the forcing  $\mathbf{Q}$  to the total energy

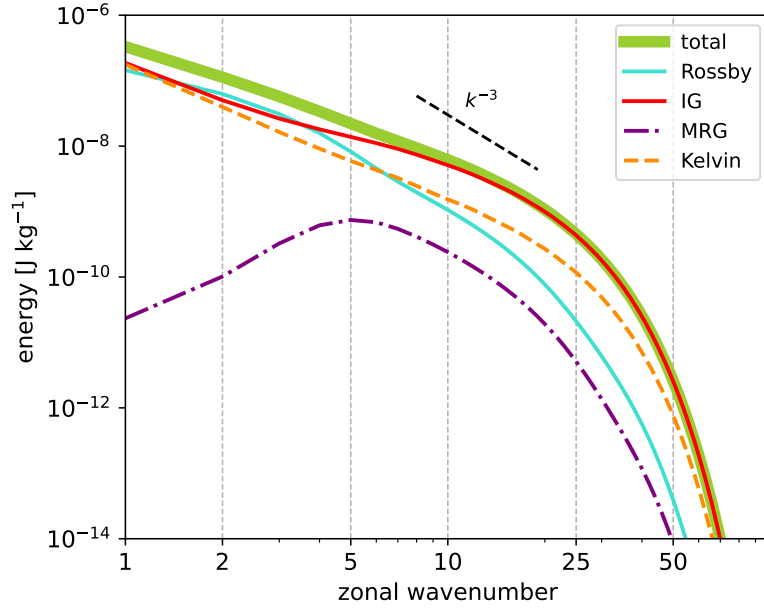


**Figure A1.** Total wave energy spectrum and its partition into contributions from the IG modes, the Rossby modes, the Kelvin mode and the MRG mode. The spectra are a result of SYMFOR-JJA simulation in Table A1 run with the JJA background wind of year 1993. The spectra are averaged over the first 3 days of the simulation.

tendencies. From Equation A2.7, it follows that for  $k \geq 1$ :

$$\frac{d}{dt} E_{n,l}^k \equiv 2gD \Re \left[ \left( \frac{d}{dt} \chi_{n,l}^k \right) (\chi_{n,l}^k)^* \right] = 2gD \Re \left\{ \left( \Psi_{n,l}^k \right) (\chi_{n,l}^k)^* + \left( q_{n,l}^k \right) (\chi_{n,l}^k)^* \right\}, \quad (\text{A2.8})$$

where

$$\Psi_{n,l}^k = \frac{1}{2\pi} \int_0^{2\pi} \int_{-\pi/2}^{\pi/2} \mathbf{N} \cdot (\mathbf{H}_{n,l}^k)^* (\lambda, \varphi) d\varphi d\lambda, \quad (\text{A2.9})$$

and

$$q_{n,l}^k = \frac{1}{2\pi} \int_0^{2\pi} \int_{-\pi/2}^{\pi/2} \mathbf{Q} \cdot (\mathbf{H}_{n,l}^k)^* (\lambda, \varphi) d\varphi d\lambda. \quad (\text{A2.10})$$

Here, the term  $\Psi_{n,l}^k$  and  $q_{n,l}^k$  are the energy tendencies by Hough and K mode interactions (i.e., including both wave-mean flow and wave-wave interactions), and the forcing respectively. Tendencies by  $\Psi_{n,l}^k$  can be further split into interactions between arbitrary wave components, e.g., IG wave - Rossby wave interactions. We evaluate wave-wave interactions between Hough modes for  $k > 0$  and wave-mean flow interactions between  $k > 0$  and  $k = 0$  modes by applying filters in the non-linear energy tendency in modal space. This diagnostics is particularly useful for studying wave excitations as it allows to separate contributions of various factors to the spectral

energy tendency of each mode.

## A2.4 Setup of numerical experiments

Numerical simulations are carried out using geostrophically balanced background zonal flows, which are prescribed either analytically or derived from reanalyses. Additional simulations use the background state of rest. The background flows for the matching pairs of simulations with fully non-linear and linearized models are identical zonal steady states of non-linear RSW Equations A2.1 without damping. TIGAR generates balanced background geopotential height by projecting the prescribed zonal wind field onto  $k = 0$  Rossby modes. The algorithm of the construction is described in the Supplements.

The formulation of the background state accounts for the symmetry and strength of the jet. To compare and quantify the importance of factors such as wave-wave and wave-mean flow interactions, location and symmetry of the wave source and the mean depth, we perform a number of sensitivity experiments, which are summarized in Table A1. Note that the forcing is called symmetric whenever  $Q$  is centred at the equator, otherwise we refer to asymmetric forcing.

**Table A1.** Summary of the numerical experiments. The simulations are defined by the symmetry of the forcing, the shape of the background zonal wind, the TIGAR version and the applied mean depth  $D$ .

Exp label	Forcing symmetry	Background flow	TIGAR version	D
ASYMFOR-NOF	asymmetric	state of rest	non-linear resting state linear	400 m 250 m
SYMFOR-NOF	symmetric	state of rest	non-linear	400 m 250 m
SYMFOR-SYMJET	symmetric	symmetric jet	non-linear	400 m 250 m
SYMFOR-ASYJET	symmetric	asymmetric jet	non-linear, linearized	400 m 250 m
ASYMFOR-ASYJET	asymmetric	asymmetric jet	non-linear	400 m
SYMFOR-MAM SYMFOR-JJA	symmetric	ERA5 mean flows of MAM or JJA	non-linear	400 m
ASYMFOR-MAM ASYMFOR-JJA	asymmetric	ERA5 mean flows of MAM or JJA	non-linear	400 m

First, we apply idealised zonal wind profiles with a steady jet (denoted JET). The JET simulations are further split into SYMJET and ASYJET that include two jets each located outside

the tropics which are either symmetric or asymmetric with respect to the equator. These profiles are shown in Figure A2 along with an example of the balanced height field. The ASYJET zonal wind profile has a weaker jet in the Southern Hemisphere (SH) that is shifted further away from the equator compared to the jet north of the equator. The jets are controlled by the central latitudes ( $30^\circ$  and  $47.5^\circ$  for ASYJET profile), the e-folding half-width ( $10^\circ$ ) and the maximum amplitude. The latter is taken 30 and 21 m/s for the ASYJET profile. Simulations with a motionless initial state are denoted NOF.

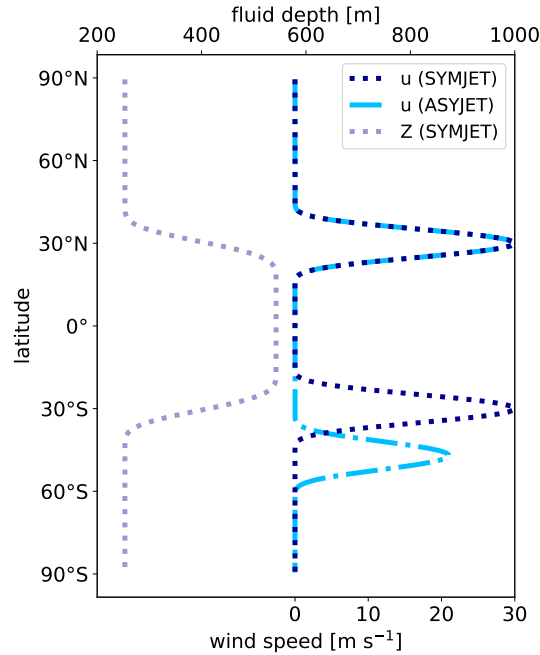


**Figure A2.** Latitudinal profiles of the idealised zonal mean background flows (SYMJET and ASYJET). The balanced height field of SYMJET is added.

idealised simulations are complemented by background zonal wind profiles derived from ERA5 reanalysis data (Hersbach et al., 2020). We use seasonal zonally-averaged zonal wind at 200 hPa in years 1993, 1999, 2009, 2012 and 2016. The profiles are shown in Figure A3 for JJA and MAM seasons. A visual inspection of Figure A3 suggests that the zonally-averaged zonal wind is more asymmetric in JJA than in MAM, irrespective of the state of ENSO. In order to quantify the asymmetry of the background state, we define a zonal asymmetry measure (ZAM) in Hough harmonics space as the ratio between energies in the asymmetric and symmetric linearly

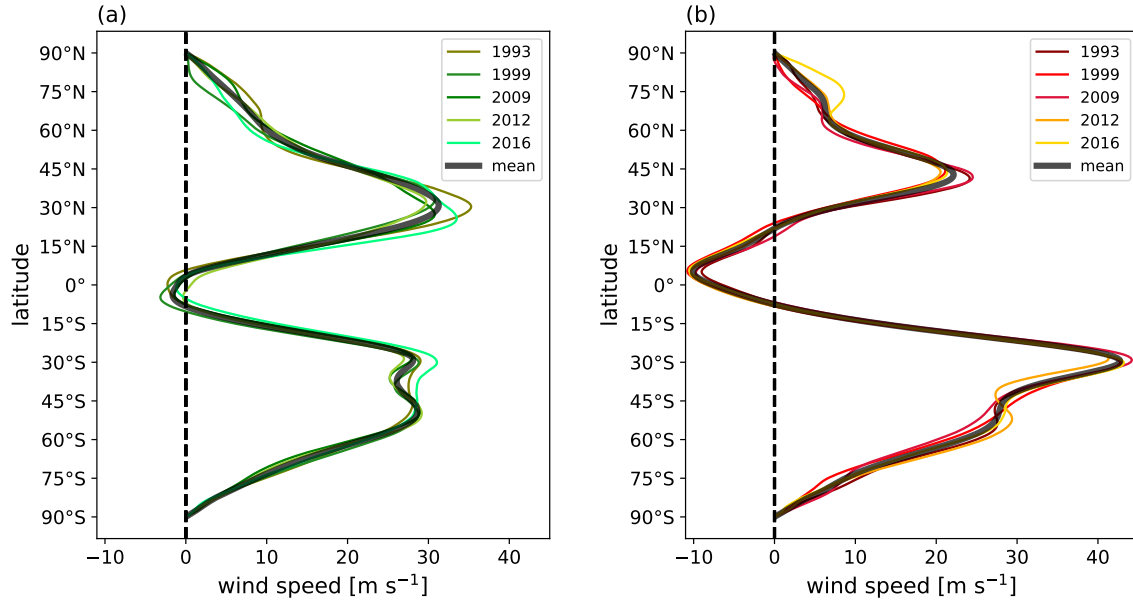


**Figure A3.** Zonally-averaged zonal wind in ERA5 reanalysis at 200 hPa for (a) MAM and (b) JJA seasons. Five selected years are 1993, 1999, 2009, 2012 and 2016. The mean profiles are shown by solid black lines.

balanced background state (i.e., Rossby  $k=0$ ) modes:

$$ZAM \equiv \frac{\left| \sum_{n=0}^M \chi_{2n,l=1}^{k=0} \right|^2}{\left| \sum_{n=0}^M \chi_{2n+1,l=1}^{k=0} \right|^2} = \frac{\left| \sum_{n=0}^M \chi_{l=1}^{k=0} (asym.) \right|^2}{\left| \sum_{n=0}^M \chi_{l=1}^{k=0} (sym.) \right|^2}. \quad (\text{A2.11})$$

The larger the ZAM, the larger the asymmetry. The mean value of ZAM for JJA and MAM seasons is 0.39 and 0.02 respectively. The flow asymmetry is greater for the SON season compared to DJF (0.07 and 0.05 respectively), but we find that the differences among the seasons are the largest between JJA and MAM and limit our simulations to these two seasons.

Furthermore, we evaluate the conditions for barotropic instability of the applied background profiles using the Rayleigh-Kuo criterion (Kuo, 1949) and find that the jet flanks of ASYJET and SYMJET profiles are unstable, however barotropic instability was not excited in any of these experiments. In the case of the profiles derived from ERA5, the tropics and the midlatitude region appears barotropically stable, whereas the poles are moderately unstable. The difference between the stability of the zonally averaged zonal flow in MAM and JJA is negligible.

Simulations are run with two mean depths:  $D = 250$  m and  $D = 400$  m, which belong to the range of characteristic values of the equivalent depth of the tropical atmosphere. The former has been commonly used for studying the tropical response to heating perturbations in adiabatic

barotropic models with a lid at the tropopause (e.g. Kasahara and da Silva Dias, 1986; Raupp and Silva Dias, 2005), whereas the latter is the equivalent depth of vertical mode associated with deep convection when the lid is removed (i.e. moved to the level above the mesopause) (Žagar et al., 2022).

The forcing  $Q$  is represented by a Gaussian function with the zonal and meridional scales  $L_x$  and  $L_y$ , respectively, central location  $(\lambda_0, \varphi_0)$  and amplitude  $A$ :

$$Q = A \exp\left(-\frac{(\lambda - \lambda_0)^2}{2L_x^2} - \frac{(\varphi - \varphi_0)^2}{2L_y^2}\right). \quad (\text{A2.12})$$

Both  $L_x$  and  $L_y$  equal to the equatorial deformation radius  $\alpha_e = (\sqrt{gD}/(2\beta))^{1/2}$ . In our setup,  $\alpha_e$  equals to  $10.54^\circ$  and  $9.37^\circ$  for  $D = 400$  m and  $D = 250$  m respectively. The central location of the asymmetric heating is  $2.5^\circ$ . The amplitude of the forcing is  $A = 1.9$  m/day and  $3.05$  m/day for  $D = 250$  m and  $400$  m, respectively, which corresponds to approximately  $2.5$  K/day heating rate. This is consistent with typical radiative heating rate of convective cells in the tropics (McFarlane et al., 2007). The default linear damping time scale is chosen equal for the Rayleigh friction and the Newtonian cooling,  $\tau_R = \tau_N = 5$  days.

Numerical simulations are performed using the triangular truncation T170 that corresponds to the F128 regular Gaussian grid. The model is integrated in time using the fourth order exponential Runge-Kutta method with time step of 5 minutes.

## A2.5 Sensitivity of MRGWs excited by external forcing to modelling setup

Placing an asymmetric heat source in the tropics leads to direct excitation of MRGWs (e.g. Holton, 1972), as the forcing associated with heating directly projects onto the MRG mode. This experiment is denoted ASYMFOR-NOF in Table A1 and it is performed with the resting state linear (LI) and non-linear (NL) TIGAR both using the state of rest as the initial condition. The asymmetric heat source is centred at  $2.5^\circ\text{N}$ .

Figure A4 shows the evolution of the MRG mode energy (panel (a)) and the energy ratio between MRG mode and the Rossby mode (panel (b)) in the linear and non-linear models. It reveals that the MRGWs are excited instantaneously in both models. The energy ratio between the MRG and the Rossby modes is largest initially and decreases gradually until reaching a quasi-equilibrium state depending on the damping timescale (at approximately 4-5 days of simulation time). It is important to notice that there is no qualitative difference between the linear and non-linear simulations: in both cases we observe rapid MRG excitation. Thus, wave-wave

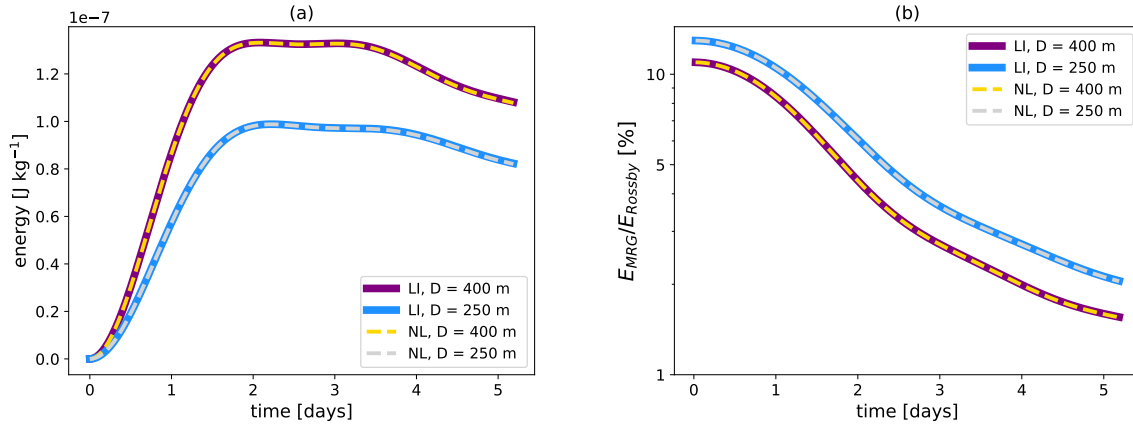


**Figure A4.** (a) Evolution of the MRGW energy and (b) the evolution of the ratio between the MRGW energy and the Rossby mode energy in the ASYMFOR-NOF simulations (Table A1). Solid and dashed lines correspond to the simulations in linear (LI) and non-linear (NL) models, respectively. Purple and gold curves denote solutions from the experiments with the mean depth  $D = 400$  m, whereas blue and silver curves denote the mean depth  $D = 250$  m.

interactions are irrelevant as an excitation mechanism in this setup.

The MRGW energy and the ratio of energies in the MRG and Rossby waves is sensitive to the model setup and forcing parameters. Sensitivity of energy distribution to the spatial scale and the ratio of the zonal and meridional length scales of the forcing was demonstrated by Silva Dias et al. (1983). For example, the growth is the most intense when the heat source is placed at the scale of the equatorial deformation radius (i.e. around  $10^\circ$  in case of  $D = 400$  m). The MRG energy growth is furthermore influenced by the model mean depth, which defines the meridional scale of the MRGWs. While quantitatively different, solutions for two mean depths in Fig. A4 are qualitatively similar illustrating that the underlying dynamical processes are the same.

### A3 Excitation of MRGWs by wave-mean flow interactions

Now we carry out simulations focusing on the role of the background flow in the MRGW generation. First, we provide evidence that wave-mean flow interactions can excite MRGWs. Then we concentrate on the scale selection during the excitation process.

Focusing on wave-mean flow interactions, we exclude the direct excitation of MRGWs due to convection by placing the forcing at the equator. The corresponding simulations in Table A1 are SYMFOR-NOF, SYMFOR-SYMJET and SYMFOR-ASYJET. All simulations are run with the non-linear TIGAR, except SYMFOR-ASYJET, which is also run with the linearized (LZ) model.

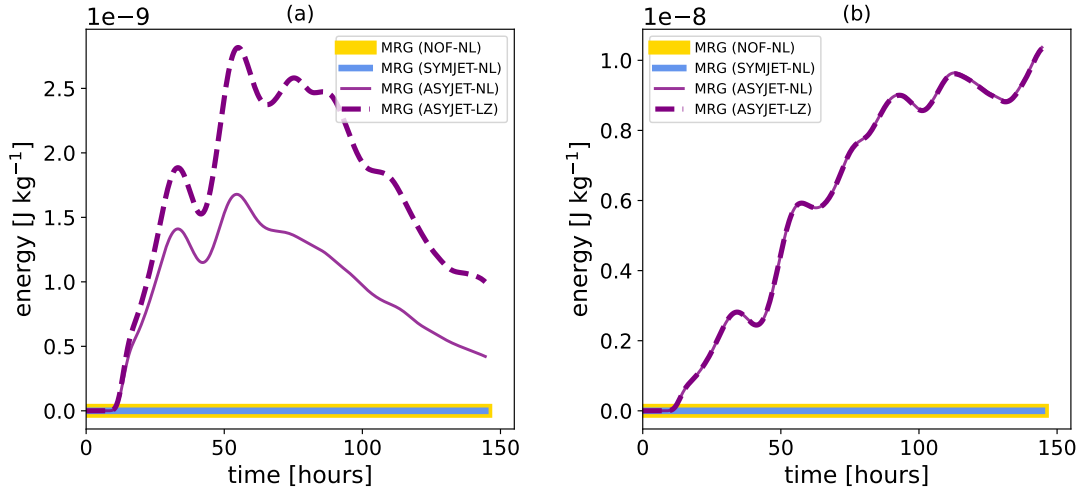


**Figure A5.** Evolution of the MRGW energy in SYMFOR-NOF, SYMFOR-SYMJET and SYMFOR-ASYJET simulations with  $D = 400$  m. (a) linear damping is applied with timescale of 5 days. (b) no linear damping. NL and LZ denotes simulations with non-linear and linearized TIGAR, respectively.

Figure A5 shows the time evolution of the MRGW energy in the first 140 hours of these simulations. MRGWs grow only in simulations using an asymmetric background state. This identifies the interactions between the waves generated by the symmetric heat source and the asymmetric subtropical jet, i.e., wave-mean flow interactions, as the cause of MRGW excitation. The fact that at the start of the ASYJET-NL simulation only symmetric  $k > 0$  modes are present in the system, which cannot produce asymmetric modes by triad interactions, rules out the hypothesis that wave-wave interactions could play a primary role here. We show results only for  $D = 400$  m but the results for  $D = 250$  m are qualitatively very similar.

The excitation timescale in Figure A5 matches the time required for the IG waves excited by the prescribed heat source to reach the jet region. The timescale (about 9 hours in this case) depends on the mean depth  $D$  and it can be estimated using the location of the jet flanks and the gravity wave speed  $\sqrt{gD}$ . Note that using a different depth representative of the troposphere, for example  $D = 250$  m, influences the time scale relatively little compared to the effect of the jet distance from the equator.

It is also apparent in Figure A5 that the MRGW energy oscillates in time, which was also noticed by Raupp and Silva Dias (2005). This vacillation emerges both in the non-linear (NL) and in the linearized (LZ) simulations with similar periods, likely due to non-resonant forcing provided by wave-mean flow interactions. In simulations with asymmetric forcing the vacillation practically disappears. As the transient features of the excited MRGW energy are outside the scope of the study, we have not investigated them further.

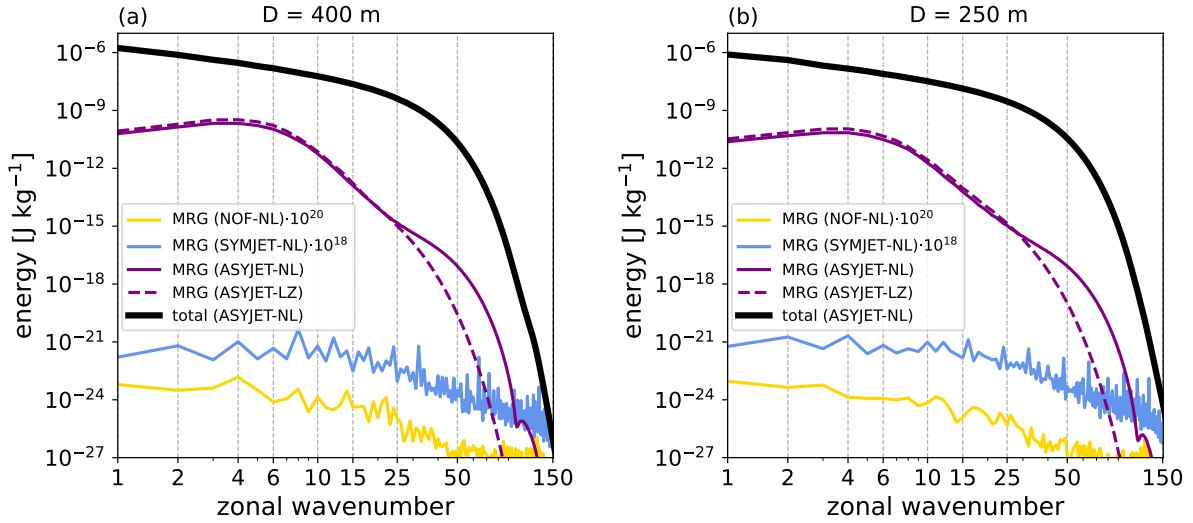


**Figure A6.** MRGW energy spectra of the SYMFOR-NOF, SYMFOR-SYMJET and SYMFOR-ASYJET for (a)  $D = 400$  m, and (b)  $D = 250$  m and the total wave energy in the SYMFOR-ASYJET NL simulation.

Another feature of Figure A5a is a significant difference in energy levels between the NL and LZ simulations after the first 24 hours, which is due to the linear damping. In the NL simulation, the damping acts on both the zonal mean flow and the waves whereas only waves are damped in the LZ experiment resulting in a decreased energy extraction from the system. When no damping is applied (Figure A5b), the excited MRGW energy in the two simulations match.

Time-averaged MRGW energy spectra for the two equivalent depths are shown in Figure A6. The averaging time (3 days) covers the period of the MRGW development and is within the typical lifetime of observed MRG waves (Zangvil and Yanai, 1980). Figure A6 shows a typical red energy spectrum with the total energy continuously decreasing with the zonal wavenumber. In contrast, the MRGW energy spectrum has a peak at zonal wavenumber  $k = 4$ . Similarity between the MRGW spectra in the NL and LZ simulations at large scales indicates the irrelevance of wave-wave interactions for the MRG wave generation process. Large differences between the two simulations are present at subsynoptic scales beyond  $k \approx 25$  where the NL simulations are far more energetic. The energy source in the NL case are interactions between  $k = 0$  IG and  $k > 0$  modes absent in the linearized system (not shown). No significant difference is found between the two equivalent depths.

Analysis in physical space reveals that the advection of mean momentum by the forced gravity waves (i.e., term  $-v' \partial \bar{u} / \partial \varphi$ ) is responsible for the MRGW excitation, however, other terms also have positive contributions after the excitation. Overall the advective terms in the momentum equations contribute the most to the MRG growth in the first 24 hours of simulation

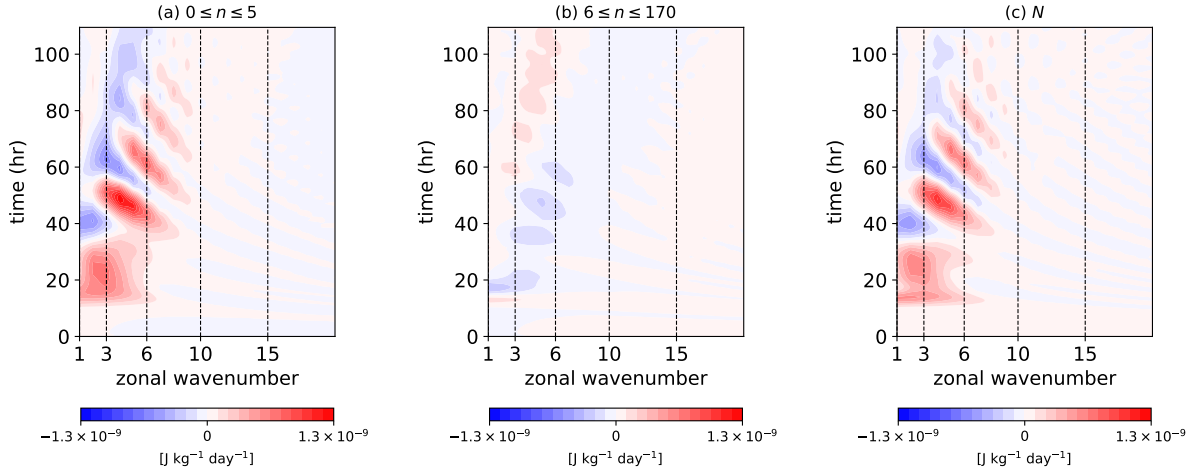


**Figure A7.** Evolution of spectral energy tendencies of the MRGW as a function of zonal wavenumber in the NL SYMFOR-ASYJET experiment with  $D = 400$  m. The MRGW energy tendency is partitioned into the contributions by (a) low meridional modes - mean flow interactions and (b) high meridional modes - mean flow interactions, (c) tendencies due to all interactions including wave-mean flow and wave-wave interactions. For every  $n$ , all  $k > 0$  are included in the summation.

time, whereas the advection and the divergence term in the continuity equation have slight negative and positive contribution, respectively. In addition, the terms involving  $\tan \varphi$ , i.e. the metric terms are practically negligible.

To create conditions favorable to MRGW generation, the westerly jet has to be in relative proximity of the equator i.e. within the meridional length scale of the MRG waves for a given  $D$ . This is easily verified by carrying out simulations in which the jets are moved further away from the tropics (not shown). This also means that a crucial role in the MRGW excitation process is played by interaction of the balanced mean state with waves with low meridional wave indices that have their strongest signal on the equatorward side of the jet. This is illustrated in Figure A7 for the non-linear SYMFOR-ASYJET simulation with  $D = 400$  m by showing separately the MRGW spectral energy tendencies due to wave-mean flow interactions involving low meridional modes  $0 \leq n \leq 5$  and modes with high meridional indices  $5 \leq n \leq 170$ . The largest contribution to the MRGW tendencies are by the  $n = 1$  Rossby mode, although this mode alone cannot explain the energy evolution of MRGWs. While IG modes, being the first to reach the jet, initiate the interactions, the Rossby mode - mean flow interactions become more relevant after about 40 hrs of simulation in case of  $D = 400$  m. Similarly, perturbations from midlatitudes or locally imposed perturbations on the jet can excite an MRGW signal depending on the choice of  $D$ , but the amplitudes of the excited waves are much smaller than in the case of perturbations emanating from tropical heating.

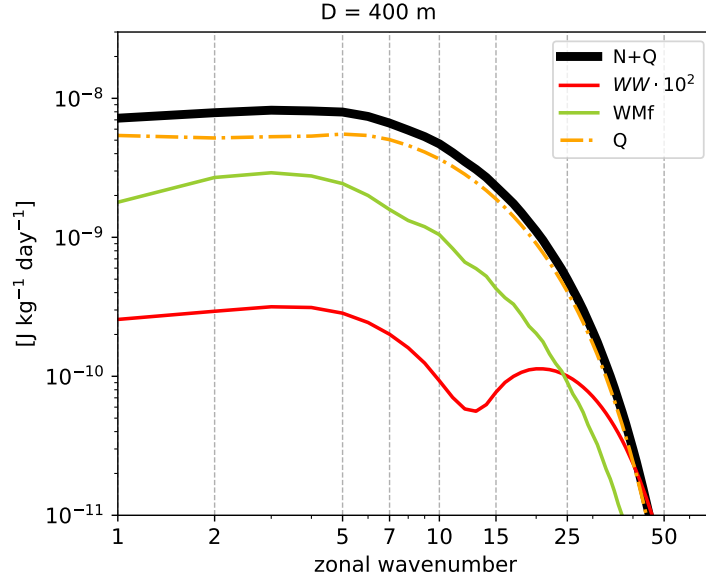


**Figure A8.** Absolute spectral energy tendencies of the MRGW in the NL ASYMFOR-ASYJET simulation. The contributions by the wave-wave, wave-mean flow interactions and external forcing are denoted WW, WMf and Q, respectively. The WW spectrum is multiplied by  $10^2$ . Energy tendencies are averaged over two days. For the definition of the **N** and **Q** terms see Equation A2.5.

The results presented so far show that the generated MRGWs have the peak signal at large synoptic scales. Now we address the scale selection focusing on the processes contributing to the MRG energy growth. For this, we analyse the energy tendency equation (A2.8) in the non-linear simulation. The tendency is partitioned into the contribution by the external forcing, wave-mean flow and wave-wave interactions. The results are shown in Figure A8 as absolute MRG tendency spectra, which confirms that wave-mean flow interactions play a dominant role in the MRGW scale selection as they are characterized by a well-defined spectral peak that is located at  $k = 3 - 5$ . The forcing, which is Gaussian, makes the total spectrum more flat at scales  $k < 15$  and its amplitude for the selected model setup exceeds that of the wave-mean flow interactions. The contribution of wave-wave interactions is approximately 3 orders of magnitude smaller than that of the other two mechanisms. However, tendencies due to wave-wave interactions exceed the wave-mean flow interactions' tendencies at small scales. This happens only for  $k > 70$  scales, which are energetically unimportant compared to large and synoptic scales.

How sensitive are these results to the amplitude and scale of the forcing and to the timescale of the damping? To address this question, we carried out series of simulations varying various model and forcing parameters. Figure A9 shows that wave-wave interactions do not play a significant role, even when the forcing is 10 and 100 times stronger (i.e., equivalent

to 25 and 250 K/day heating rate, respectively) compared to the setup of SYMFOR-ASYJET NL simulation. Although the importance of wave-wave interactions increases with the forcing strength, their amplitude at large scales is two orders of magnitude smaller than the amplitude of wave-mean flow interactions even for 100 times stronger forcing. Increasing the linear damping timescale from 5 to 10 days also does not affect the MRGW excitation and the growth process (not shown). The twice longer damping time changes the ratio between the absolute energy tendencies due to wave-wave and wave-mean flow interactions by a factor of 7.5 for  $k = 5$ . Nevertheless, wave-mean flow interactions still remain 3 orders of magnitude larger even for the increased damping. Furthermore, neither the horizontal scale nor the latitude of the forcing affects the dominant MRGW excitation mechanism, i.e. wave-mean flow interactions and scale selection. Simulations with varying zonal and meridional scales of the forcing showed that both of these scales affect the amplitude of the excited MRG wave. Only a very large zonal scale of the forcing (e-folding scale  $> 60^\circ$ ) such as the ITCZ-like forcing, was found to influence the dominant scale of the excited MRGW by shifting it to smaller zonal wavenumbers.

The observed spectral peak in the MRGW energy spectra is somewhat sensitive to the averaging period and evolves with time (not shown). Nevertheless, we find that local maxima in the MRGW energy spectra are always attributed to the wave-mean flow interactions. Furthermore, as the mean depth rises, the relative importance of these interactions increases and can even exceed the amplitude of energy tendencies due to the forcing at large scales.

## **A4 Excitation of MRGWs in simulations with realistic background flow**

Now we apply the background zonal-mean zonal winds derived from ERA5 for the boreal spring and summer seasons, as listed in Table A1. Our first goal is to verify the conclusions based on the idealised background jet in realistic setting. The second goal is to quantify to what extent the observed asymmetry affects the MRGW excitation process. The input background profiles were shown in Figure A3. As discussed in section A2.4, the JJA season has a higher asymmetry than the MAM season. To quantify the asymmetry of the background zonal flow, we defined in Section A2.4 the measure ZAM (Equation A2.11) that is now applied to discuss the MRGW energy evolution as a function of the background wind in different seasons. Model parameters for these experiments are like in the NL referent case with  $D = 400$  m and damping time scale of 5 days.

The results are summarised in Figure A10. The MRGWs are generated in all simulations just like in the idealised case. As barotropic instability was not excited in any of the realistic

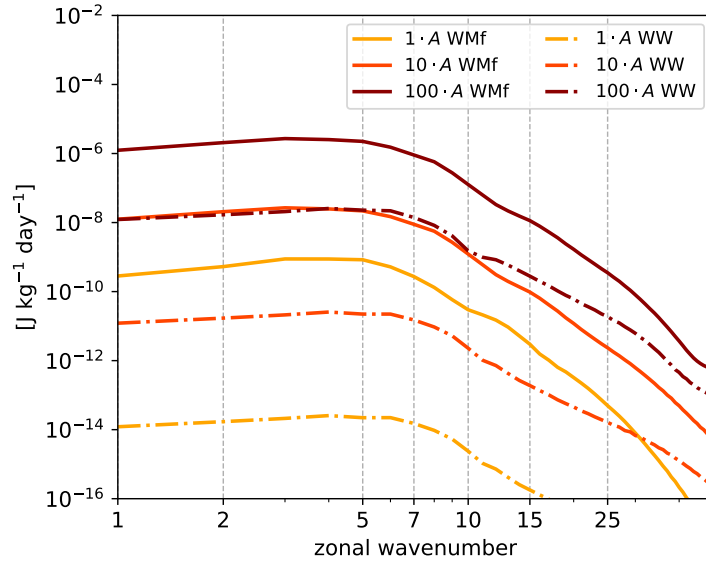


**Figure A9.** Absolute spectral energy tendencies of the MRGW in the NL SYMFOR-ASYJET simulation with  $D = 400$  m and forcing amplitude ( $A$  in Equation A2.12) equal to 3.05, 30.5 and 305 m/day (dark yellow, orange and dark red curve, respectively). The contributions by wave-wave and wave-mean flow interactions are denoted WW and WMf, respectively. Energy tendencies are averaged over three days.

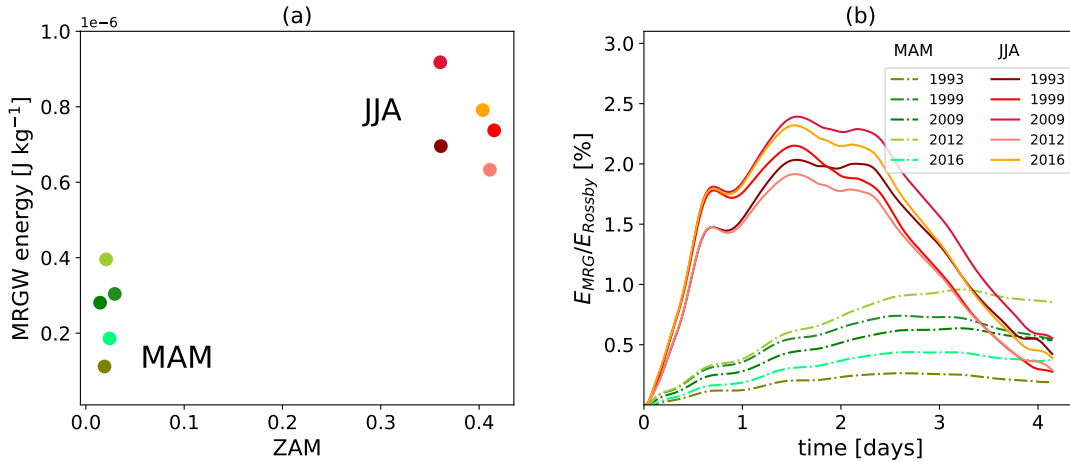


**Figure A10.** (a) The MRGW energy integrated over 3 days and all zonal wavenumbers as a function of the asymmetry of the background flow as defined by Equation A2.11. (b) Evolution of the ratio between the energy of the MRGW and the Rossby mode energy (in %) in the NL simulations with the symmetric forcing and ERA5 background profiles from Figure A3. The shades of red and green stand for the background profiles in JJA and MAM seasons, respectively.

simulations, the MRGW excitation is only a result of wave-mean flow interactions. There is however a significant difference in the evolution of the MRGW energy depending on the

asymmetry of the background zonal wind. First of all, Figure A10a shows that more asymmetric profiles produce more energetic MRGW signals. This applies to all profiles from the JJA season. Figure A10b, which shows the evolution of the MRGW energy as a ratio of the Rossby mode energy, reveals that JJA simulations with significant asymmetry have energy evolution more similar to that in the idealised case. Simulation with MAM profiles, with a nearly zero value of the asymmetry measure ZAM, have slowly growing and smaller MRGW energy levels that appear also less sensitive to the damping.

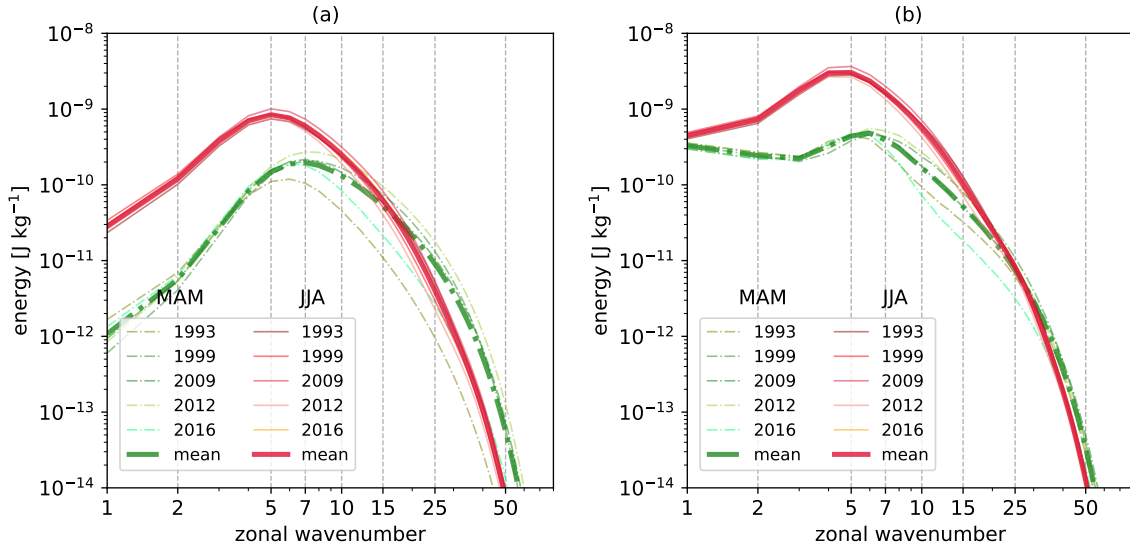


**Figure A11.** Energy spectra of the MRGWs in simulations with realistic background zonal wind and a) symmetric and b) asymmetric forcing. The averaging period is 3 days. Thin and thick curves denote the individual simulations and the means over JJA and MAM cases, respectively.

To compare the effect of wave-mean flow interactions with the direct excitation by the asymmetric forcing, we show in Figure A11 the MRGW energy spectra in the simulations with realistic background flows for the case of both symmetric and asymmetric forcing. As earlier, the spectra are averaged over the first 3 days of simulation time. The main feature of Figure A11 is that the presence of asymmetric forcing greatly increases the large-scale part of the MRGW energy. In this case, the MRGW energy at  $k = 1$  is far less sensitive to the flow asymmetry; that is, the MRGW energy at planetary scales in JJA and MAM is more similar. This is indeed what one would expect since no major difference in the observed MRGW scale was reported for the two seasons. Overall, there is more MRGW energy in the simulations with asymmetric forcing at every  $k$ , and in JJA simulations compared to MAM cases for  $k < 20$ .

Another important feature in Figure A11 is that all spectra have peak energy at synoptic scales similar to the idealised simulations. The forcing symmetry i.e. the season plays little

role for the peak scale of the excited MRGWs. For the symmetric forcing, the dominant MRGW wavenumber is  $k = 5$  in JJA and  $k = 7$  in MAM season. These peak scales are little affected in the simulations with the asymmetric forcing which, as already discussed, leads to the excitation of MRGWs across large scales in both seasons. These findings are robust to the choice of the forcing parameters (e.g., the central latitude, amplitude and the horizontal scales of the forcing) that further underscores the significance of wave-mean flow interactions in excitation of the MRG waves.

## A5 Discussion and Conclusions

We investigated the excitation mechanism of the mixed Rossby-gravity waves (MRGWs) in the tropical troposphere using the TIGAR model, which incorporates the MRGW as a prognostic variable alongside other waves. This approach enabled us to directly quantify processes contributing to the MRGW development in the model, presenting a distinct advantage over conventional equatorial wave filtering techniques. Using this novel framework, we showed that MRGWs are generated by wave-mean flow interactions provided that the mean flow is asymmetric with respect to the equator. The excited MRGWs have the maximal energy at the zonal wavenumbers  $k = 4 - 5$ , in agreement with observations (e.g. Yang and Hoskins, 2017; Stephan et al., 2021).

The wave-mean flow interactions as an excitation and scale selection mechanism was further confirmed by the analysis of the MRG spectral energy tendencies. By comparing the contributions of wave-mean flow and wave-wave interactions and the contribution of the asymmetric forcing, we found that wave-mean flow interactions dominate the MRG energy growth even when the forcing amplitude is made 100 times greater than in the referent simulation with realistic heating rates used to represent the forcing. Similarly, the MRG wave excitation process is not sensitive to the linear damping timescale.

The background flow itself can potentially determine the selected zonal wavenumber of the excited MRG waves through the instability growth associated with linearized dynamics. This hypothesis is verified by studying the eigenmodes of the system linearized about the pertinent background state. The background eigenmodes are determined following the algorithm suggested by Kasahara (1980). We find unstable background eigenmodes with substantial projection onto the MRG modes in range of  $k = 1 - 17$  and  $k = 1 - 19$  for the idealised and realistic background zonal flows, respectively. However, most of these unstable eigenmodes have a small growth exponent, which varies only slightly across nearby scales. For this reason, the selected MRGW scales generally do not coincide with the fastest growing mode of the linearized system, rather

they are determined by the peak in the wave-mean flow interactions. This peak fluctuates in time due to changes in phases of interacting waves, which explains the slight movement of the MRGW spectral peak. For instance, Figure A12 shows the amplitudes of the contributions of the wave-mean flow interactions to the MRGW tendencies over the first 4.5 days of a simulation with a realistic background flow in JJA in 1993. It is apparent that the preferred zonal wavenumber, which is a recipient of most of energy from interactions, changes over time, but remains at zonal wavenumbers between  $k = 3$  and  $k = 6$ , which is consistent with the maximal MRGW signal at  $k = 5$  in the time-averaged energy spectra reported in our paper and previous observational studies.

MRGWs can also alter the background flow as demonstrated by Hua et al. (2008), who showed that MRG waves with short zonal wavelengths can be destabilized by barotropic shear instability leading to the formation of zonal jets. They utilized an intermediate complexity ocean model solving the continuously stratified primitive equations. In our simulations the synoptic-scale MRGWs are stable and in principle they are beyond the short-wave limit described in Hua et al. (2008).

The contribution of the forcing to MRGW tendencies is found to be nearly flat at large scales, whereas the MRGW tendencies due to wave-mean flow interactions, which involve waves produced by the forcing, fluctuate over a small range of  $k$  as the phases of these waves change

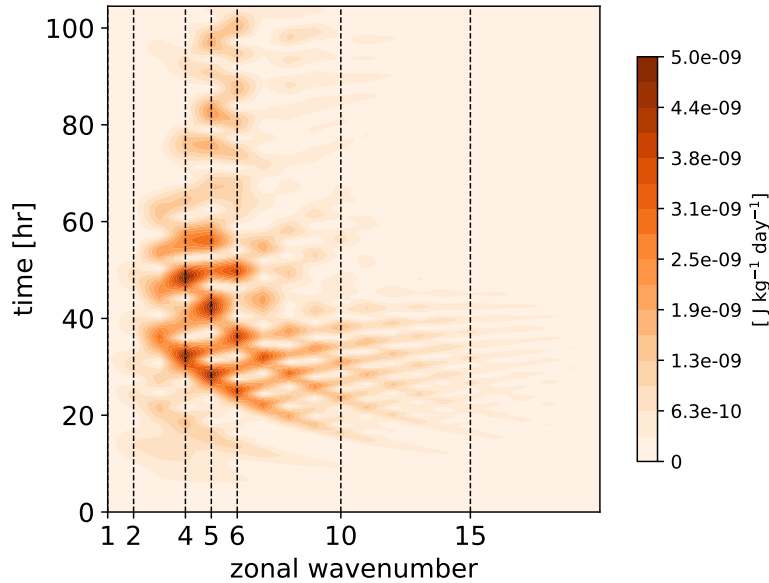


**Figure A12.** Absolute spectral energy tendencies of the MRGW as a function of zonal wavenumber and time in the non-linear ASYMFOR-JJA simulation with the zonal mean zonal wind of JJA 1993.

in time. Should the forcing have a peak zonal wavenumber in the MRGW absolute tendency spectra, wave-mean flow interactions would also peak at the same  $k$ , therefore the scale of the generated MRGWs would be completely predictable. The peak scale of the MRGW excitation is likely sensitive to waves in the background, which is a potential subject of a future study.

Two earlier studies of non-linear excitation mechanism of MRGWs require discussion. First, Itoh and Ghil (1988) showed that asymmetric lateral boundary forcing of the thermodynamic equation reinforces asymmetric tropical modes. They suggested that there may be enhanced MRGW activity in the summer and winter season when the midlatitude westerlies in the winter hemisphere are intensified. They proposed wave-CISK as the MRGW excitation mechanism, which introduces asymmetry through boundary forcing and, therefore requires certain properties of extra-tropical flows to maintain. Here we demonstrate a different mechanism, where MRGW growth is promoted by wave-mean flow interactions that are local to the tropics and do not require any extratropical input.

Second, we could not find a significant evidence of the excitation of MRGWs by wave-wave interactions suggested by Raupp and Silva Dias (2005). In their simulations with an equatorial  $\beta$ -plane shallow water model, the initial state was prepared using an off-equatorial stationary heat source and they observed strong MRGW development, provided IG waves were suppressed in the model. In our experiments, an asymmetric heat source leads to the growth of MRGWs directly regardless of the presence of the IG waves. Moreover, suppressing IG modes in our simulations does not significantly alter the contribution of wave-wave interactions to MRGW tendencies (not shown); i.e. wave-wave interactions are negligible compared to the wave-mean flow interactions and the excitation process by the external forcing.

Although our simulations are performed in a simplified model, quantitatively they are consistent with the MRGW energy estimates in reanalysis data. For instance, a comparison of the MRGW energy levels with other wave types by Žagar et al. (2009) showed that MRGWs comprise about 10% of the non-Rossby wave flow that itself makes about 10% of the total wave flow, bringing the MRGW energy to approximately 1% of the total wave energy. This percentage roughly correspond to the values obtained in simulations with realistic background flows in the present study. We note here that the share of the MRGW signal in the global intraseasonal non-Rossby flow variance is three times greater than in its mean energy contribution Stephan et al. (2021), highlighting the importance of MRGWs for subseasonal prediction.

The atmosphere is never in a symmetric zonal mean state. We demonstrated that the level of asymmetry, defined by a new spectral asymmetry measure (Equation A2.11), determines the amplitude of the MRGW signal. JJA season in ERA5 data is far more zonally asymmetric than the MAM season with respect to this measure. The background asymmetry led to a significantly

stronger MRGW response at large and synoptic scales in simulations with the zonal mean state from the JJA season compared to MAM season. The presence of asymmetric forcing has not shifted the peak scale of the response, despite leading to the MRGW excitation across large scales.

Similarly to the background flow, the real atmosphere is asymmetric also in the distribution of convective forcing with the greatest asymmetry during boreal summer. In addition, the ITCZ structure resulting from the SST distribution also influences the MRG growth by convective instability mechanism as pointed out by Hess et al. (1993). The quantification of the relative importance of the excitation by the external forcing (that mimics convection) and by wave-mean flow interactions in the real atmosphere requires the extension of the present study to the three-dimensional atmosphere.

## **A6 Acknowledgements**

This paper is a contribution to the project W6 (Spectral Energy Fluxes by Wave-Wave interactions) of the Collaborative Research Centre TRR 181 "Energy Transfers in Atmosphere and Ocean" funded by the Deutsche Forschungsgemeinschaft (DFG, German Research Foundation) - Projektnummer 274762653. We thank the two anonymous reviewers for their insightful comments that led to an improved paper, to Rolando Garcia for the discussion and the useful comments, as well as to our colleagues Frank Lunkeit and Katharina M. Holube for many discussions and comments on earlier version of the paper.

## **A7 Conflict of interest**

The authors declare no conflict of interest.

## **A8 Supplements**

### **A8.1 Numerical aspects of TIGAR**

#### **Computation of non-linear terms**

The non-linear contributions to the spectral tendencies in Equation A2.3 are computed using the classic spectral transform method (e.g. Hoskins and Simmons (1975)). First, the wind and height fields, as well as their gradients, are restored in physical space from Hough coefficients using FFT and Hough transform in zonal and meridional directions respectively. Then, the non-linear tendencies in the physical space  $\mathbf{N}$  are obtained according to Equation A2.5.

Finally, projecting the result onto Hough harmonics via Equation A2.8, yields the spectral space tendencies.

The non-linear terms in the RSW equations can be evaluated in multiple ways, which are equivalent analytically, but not necessarily so numerically. We employ so-called  $U - V$ -formulation of Ritchie (1988), where non-linear terms in the physical space are computed as

$$N_u = -\frac{\gamma}{\cos \varphi} \left[ \tilde{u} \frac{\partial \tilde{u}}{\partial \lambda} + \tilde{v} \frac{\partial \mathcal{U}}{\partial \varphi} \right], \quad (\text{A8.13a})$$

$$N_v = -\frac{\gamma}{\cos \varphi} \left[ \tilde{u} \frac{\partial \tilde{v}}{\partial \lambda} + \tilde{v} \frac{\partial \mathcal{V}}{\partial \varphi} \right] - \gamma(\tilde{u}^2 + \tilde{v}^2) \tan \varphi, \quad (\text{A8.13b})$$

$$N_h = -\gamma \left[ \frac{\tilde{u}}{\cos \varphi} \frac{\partial \tilde{h}}{\partial \lambda} + \tilde{v} \frac{\partial \tilde{h}}{\partial \varphi} + \frac{\tilde{h}}{\cos \varphi} \left( \frac{\partial \tilde{u}}{\partial \lambda} + \frac{\partial \mathcal{V}}{\partial \varphi} \right) \right]. \quad (\text{A8.13c})$$

where

$$\mathcal{U} = \tilde{u} \cos \varphi, \quad \mathcal{V} = \tilde{v} \cos \varphi, \quad \text{and} \quad [N_u, N_v, N_h]^T = \mathbf{N}. \quad (\text{A8.14})$$

The non-dimensional wind and height fields are restored from the values of Hough functions according to Equation A2.2 using FFT. Similarly, gradient terms in Equation A8.14 are restored from the derivatives of Hough functions as follows:

$$\left[ \frac{\partial \mathcal{U}}{\partial \varphi}, \frac{\partial \mathcal{V}}{\partial \varphi}, \frac{\partial \tilde{h}}{\partial \varphi} \right]^T = \sum_{k,n,l} e^{ik\lambda} \chi_{n,l}^k \mathcal{D} \Theta_{n,l}^k, \quad (\text{A8.15a})$$

$$\left[ \frac{\partial \tilde{u}}{\partial \lambda}, \frac{\partial \tilde{v}}{\partial \lambda}, \frac{\partial \tilde{h}}{\partial \lambda} \right]^T = \sum_{k,n,l} e^{ik\lambda} \chi_{n,l}^k ik \Theta_{n,l}^k, \quad (\text{A8.15b})$$

$$\text{where} \quad \mathcal{D} \Theta = \left[ \frac{\partial(\Theta_u \cos \varphi)}{\partial \varphi}, \frac{\partial(\Theta_v \cos \varphi)}{\partial \varphi}, \frac{\Theta_h}{\partial \varphi} \right]^T \quad \text{with} \quad \Theta = [\Theta_u, \Theta_v, \Theta_h]^T. \quad (\text{A8.15c})$$

The set of Hough functions  $\Theta_{n,l}^k$  together with their derivatives is computed with machine precision from Legendre polynomials and then stored for repeated use, thereby reducing the model error.

### Numerical dissipation

To enforce red power spectrum at the tail end of inertial range in long simulation, instead of more common hyperdiffusion, TIGAR uses spectral viscosity (see e.g. Gelb and Gleeson (2001)). Spectral viscosity is applied directly in spectral space, by adding a dissipative term on

the right hand side of spectral ODE, so that the model Equations A2.3 become

$$\frac{d}{d\tilde{t}} \chi_{n,l}^k(\tilde{t}) + i\tilde{\omega}_{n,l}^k \chi_{n,l}^k(\tilde{t}) = f_{n,l}^k(\tilde{t}) - d_{n,l}^k \chi_{n,l}^k(\tilde{t}), \quad (\text{A8.16})$$

where

$$d_{n,l}^k = \left\{ \begin{array}{ll} 0, & \text{if } N \leq N_c \\ \varepsilon q^2 N^2 (N+1)^2, & \text{if } N > N_c \end{array} \right\}, \quad (\text{A8.17})$$

$$N = k + n, \quad q = \exp\left(\frac{-(N-M)^2}{2(N-N_c)^2}\right), \quad \varepsilon = \frac{1}{\tau_{SV} M^3}. \quad (\text{A8.18})$$

The damping effect is controlled by the dissipation time  $\tau_{SV}$  in Equation A8.17, which is set to 884 hours and cutoff wave-number  $N_c$ .

By construction, spectral viscosity does not directly affect scales that are larger than cutoff wave-number  $N_c$ . In our simulations, following the recommendation of Gelb and Gleeson (2001), the cutoff  $N_c$  is determined from the truncation limit  $M$  via  $N_c = 2\sqrt[4]{N^3}$ , which yields  $N_c = 94$  for  $T_{170}$  resolution. Thus, our findings are not affected by numerical dissipation.

In the physical space, spectral viscosity corresponds to a high-order differential operator, which is difficult to write down explicitly. The choice of spectral viscosity over stronger types of numerical dissipation is motivated by the desire to exclude the influence of ad-hoc numerical choices on the forecast, as well as ability to do so due to increased stability of the models. For instance, ECMWF IFS model switched to spectral viscosity in cycle 41r2 (ECMWF, 2020).

## A8.2 Formulation of geostrophic zonal steady states on the sphere

Zonal steady states of non-linear RSW equations on the sphere satisfy the equations

$$u \left( 2\Omega \sin \varphi + \frac{u}{a} \tan \varphi \right) = -\frac{g}{a} \frac{\partial h}{\partial \varphi}, \quad (\text{A8.19a})$$

$$v = 0, \quad u = u(\varphi), \quad h = h(\varphi). \quad (\text{A8.19b})$$

The mean state Rossby modes ( $k = 0, l = 1$ ) are the geostrophic steady states of linearized RSW equations, so that

$$\sin \varphi \Theta_u = -\gamma \frac{\partial \Theta_h}{\partial \varphi}, \quad \Theta_v = 0. \quad (\text{A8.20})$$

Given an arbitrary zonal velocity profile  $u(\varphi)$ , the zonal steady state can be constructed

from the set of  $k = 0$  Rossby modes as follows. First, we rewrite Equation A8.19a as

$$\sin \varphi \left( \tilde{u} + \frac{\gamma \tilde{u}^2}{\cos \varphi} \right) = -\gamma \frac{\partial \tilde{h}}{\partial \varphi}. \quad (\text{A8.21})$$

Now, the modified velocity  $\hat{u} = \tilde{u} + \frac{\gamma \tilde{u}^2}{\cos \varphi}$  is expanded over the basis of  $k=0$  Rossby zonal velocity components, as

$$\hat{u} = \sum_n C_n (\Theta_u)_{n,1}^0. \quad (\text{A8.22})$$

Then, it is easy to check, that the set  $[\tilde{u}, 0, \tilde{h}]^T$ , where

$$\tilde{h} = \sum_n C_n (\Theta_h)_{n,1}^0 \quad (\text{A8.23})$$

satisfies Equation A8.21 and, therefore, is the the desired steady state.

# Appendix B: The mechanism of scale selection for mixed Rossby-gravity waves in the upper troposphere and the upper stratosphere

This paper is under revision in the *Geophysical Research Letters* as

- Mahó, S.I., Žagar, N., Lunkeit, F. & Vasylkevych, S. (2024) The mechanism of scale selection for mixed Rossby-gravity waves in the upper troposphere and the upper stratosphere. *Geophysical Research Letters*, under revision.

## Author contributions

- Mahó S.I. contributed to conceptualization, data curation, formal analysis, investigation, methodology, visualization, writing the original draft and the review.
- Žagar, N. contributed to the project administration, conceptualization, methodology, supervision, editing, review and providing the software.
- Lunkeit F. contributed to methodology, supervision, review and editing.
- Vasylkevych, S. contributed to investigation, methodology, providing the software, supervision, review and editing.

# The mechanism of scale selection for mixed Rossby-gravity waves in the upper troposphere and the upper stratosphere

Sándor István Mahó<sup>1</sup>, Nedjeljka Žagar<sup>1</sup>, Frank Lunkeit<sup>1</sup>, Sergiy Vasylykevych<sup>1</sup>

<sup>1</sup> Meteorological Institute, Center for Earth System Research and Sustainability, Universität Hamburg, Hamburg, Germany

Received: 19 June 2024

## Key points

- The mixed Rossby-gravity (MRG) waves in the upper stratosphere and the upper troposphere have peak signals at zonal wavenumbers 2-3 and 6, respectively.
- Observed peak scales are generated by wave-mean flow interactions in numerical simulations with the observed zonal-mean zonal wind profiles.
- The peak MRG scale is associated with the jet position: the closer the jet to the equator, the smaller the scale of the excited waves.

## Abstract

Mixed Rossby-gravity (MRG) waves play a significant role in tropical variability. Their kinetic energy spectra exhibit maximal amplitudes at synoptic scales in the upper troposphere and at planetary scales in the upper stratosphere. The mechanism for different scale selection in the two regions has remained elusive. Here, we use a spherical barotropic model with the background zonal wind profile derived from ERA5 reanalysis to show that the recently introduced MRG wave excitation mechanism – wave-mean flow interactions, produces MRG waves with the observed scale properties in the two regions. Idealised simulations show that the position of the zonal jet determines the MRG scale selection: the closer the jet to the equator, the smaller the scale of the excited MRG waves. Therefore, midlatitude jets, such as found in the upper stratosphere, support the excitation of planetary-scale MRG waves.

## Plain Language Summary

Mixed Rossby-gravity (MRG) waves, which affect greatly tropical weather, concentrate in two distinct atmospheric regions with different spatial scales: in the upper troposphere and in the upper stratosphere. So far, the mechanism responsible for this behaviour is not identified. In this study we propose that interactions between waves originating in the tropics and jets (i.e., wave-mean flow interactions) explain the observed MRG wave scales. We provide evidence by conducting numerical simulations with a simple atmospheric model that resolves MRG waves with high accuracy. With such a model, we are able to identify MRG waves that are generated by wave-mean flow interactions. We also show that the MRG scale can be attributed to the position of the jet in our model simulations. The closer the jet to the equator, the smaller the generated MRG waves. In this study we offer a new mechanism that explains the observed spatial scales of the tropospheric and stratospheric MRG waves. We are also pointing out the importance of the background flow to correctly represent MRG waves in atmospheric model simulations.

## B9 Introduction

Mixed Rossby-gravity (MRG) waves are westward propagating disturbances near the equator Matsuno (1966), which represent a significant portion of tropical circulation variability at large scales (Wallace, 1971; Hendon and Liebmann, 1991; Takayabu and Nitta, 1993; Wheeler et al., 2000; Takasuka et al., 2019; Yang et al., 2023). MRG waves are observed throughout the upper troposphere and the stratosphere with varying spatial scales. Observational studies agree on the prevalence of synoptic-scale (zonal wavenumbers 4-5) MRG waves in the upper troposphere (e.g., Stephan et al., 2021) with periods of about 5 days (e.g., Yanai and Hayashi, 1969; Zangvil and Yanai, 1980). MRG waves with similar properties have been detected in the lower stratosphere implying that tropospheric MRG waves may propagate vertically (Yanai and Hayashi, 1969; Ricciardulli and Garcia, 2000; Alexander et al., 2008). On the other hand, the strongest MRG wave signal in the upper stratosphere has been found at planetary scales (zonal wavenumbers 1-3) associated with a somewhat shorter period (2-3 days) compared to the troposphere (Randel et al., 1990; Hayashi, 1994).

The different zonal scales of the upper tropospheric and upper stratospheric MRG waves are illustrated in Figure B1 that shows climatological kinetic energy (KE) spectra of MRG waves derived from ERA5 reanalysis data (Hersbach et al., 2020) at 1 hPa and 200 hPa. The KE spectra are computed by the 3-dimensional wave filtering by the MODES software package (Žagar

et al., 2015) followed by the level-by-level computation of the MRG wave KE. Details of the computation can be found in Section B15.1.

The upper tropospheric spectra have a distinct energy maximum at zonal wavenumber ( $k$ ) 6 in all seasons with the peak amplitude in boreal winter (DJF) (Figure B1a). In boreal summer, the KE spectra at planetary scales are enhanced compared to other seasons. The upper stratospheric spectra are characterised by a much greater difference between the seasons with 4-5 times more energetic solstice seasons (DJF and JJA) than the transitional seasons (MAM and SON) (Figure B1b). In DJF, the MRG wave KE has a distinct maximum at zonal wavenumber  $k = 3$ , whereas in other seasons the planetary-scale KE spectra are more flat, with less pronounced maxima at  $k = 1 - 2$  (JJA) and  $k = 1$  and  $k = 3$  (MAM and SON).

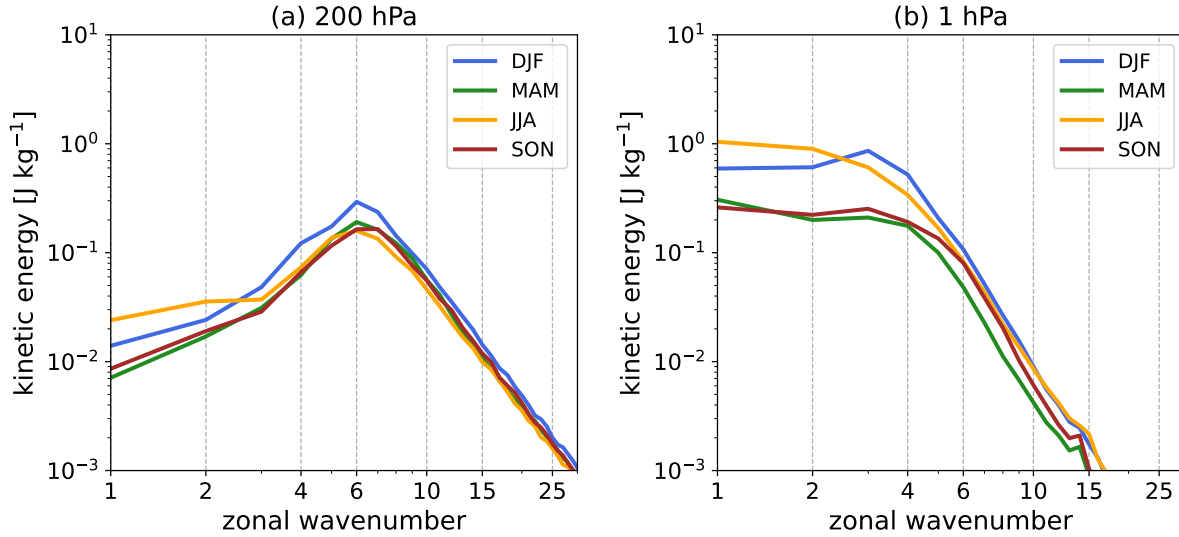


**Figure B1.** MRG wave filtering of ERA5 data (2005-2019) in different seasons. Mean kinetic energy spectra of MRG waves of 200 hPa (a) and 1 hPa (b) levels.

The key question for better understanding MRG wave variability concerns the origin of the different KE spectra in the upper troposphere and upper stratosphere. In this paper, we offer the mechanism behind the observed peak scale differences in the MRG wave KE spectra in the two layers. The mechanism is based on the recently discovered MRG wave excitation by wave-mean flow interactions, which requires asymmetric off-equatorial jets (or a single jet) for the wave growth (Mahó et al., 2024b).

Previous MRG wave excitation theories (Mak, 1969; Holton, 1972; Itoh and Ghil, 1988; Zhang, 1993; Raupp and Silva Dias, 2005) could not fully explain the MRG wave scale selection in the upper troposphere. Furthermore, no theory to our knowledge was proposed to explain the planetary MRG scale selection in the upper stratosphere. For an overview of the MRG wave

excitation theories, we refer the reader to Mahó et al. (2024b).

The wave-mean flow interaction mechanism of Mahó et al. (2024b) explored advantages of a non-linear spherical shallow water model TIGAR (Vasylkevych and Žagar, 2021), which represents MRG waves as prognostic variables and provides a novel framework for diagnosing MRG wave growth. The same modelling framework is applied in the present study with background flows in the upper troposphere and upper stratosphere derived from ERA5 to show that wave-mean flow interactions reproduce MRG wave energy spectra with the observed scales in the two regions. Furthermore, we conduct a series of idealised simulations to elucidate how the latitudinal position of the jet relative to the equator defines the dominant MRG scales. In Section B10, we show how the observed properties of MRG waves are reproduced in numerical simulations. Sensitivity studies exploring how the jet position determines the MRG wave scale selection are presented in Section B11. Finally, in Section B12 we discuss implications of our results after stating the main conclusions.

## **B10 MRG wave scale selection in simulations with realistic zonal wind profiles**

The initial conditions of numerical simulations include a geostrophically balanced zonal background flow and a Gaussian height perturbation acting as a wave source. The source is located at the equator and generates a red spectrum of inertia-gravity (IG) and Rossby waves, but not the MRG waves. The background flow is the ERA5 zonal-mean zonal wind from the DJF season at 200 hPa and 1 hPa averaged for the years 2006-2020. This defines two TIGAR simulations, TROPO and STRATO for 200 hPa and 1 hPa level, respectively. We opted for the DJF season, when the MRG waves have the most prominent variance peaks both in the upper troposphere and the stratosphere (Figure B1). Using the background flows from other seasons leads to essentially the same conclusions regarding the MRG scale selection.

We prescribe the model mean depth  $D = 400$  m and  $D = 10$  km for the TROPO and STRATO simulations respectively. The two depths correspond to vertical modes that are representative for equatorial wave dynamics in the two regions of interest, as we discuss in Section B15.2. The Gaussian initial wave source has a zonal and meridional e-folding scale equal to the equatorial deformation radius, which is  $10.54^\circ$  and  $23.66^\circ$  for the TROPO and STRATO case respectively, and an amplitude of 5% of the applied shallow water mean depth, which guarantees that the perturbation has the same relative strength in all simulations. Such initial perturbations represent waves that are either generated in situ by e.g. a convective forcing (in the case of TROPO simulation) or propagate from lower levels (in the case of STRATO simulation).

The background profiles of TROPO and STRATO simulations are shown in Fig. B2a. Notice that the tropospheric subtropical jet in DJF is weaker and shifted poleward in the summer hemisphere compared to the winter hemisphere. In comparison, the stratosphere is characterised by much stronger circumpolar westerly and easterly jet in the winter and summer hemisphere respectively. Figure B2a also includes the balanced geopotential height profiles, whose computation and the definition of the initial perturbation are described in Section B15.2, along with a summary of the TIGAR model. More detailed description of the mathematical and numerical formulation of the model can be found in Vasylkevych and Žagar (2021).

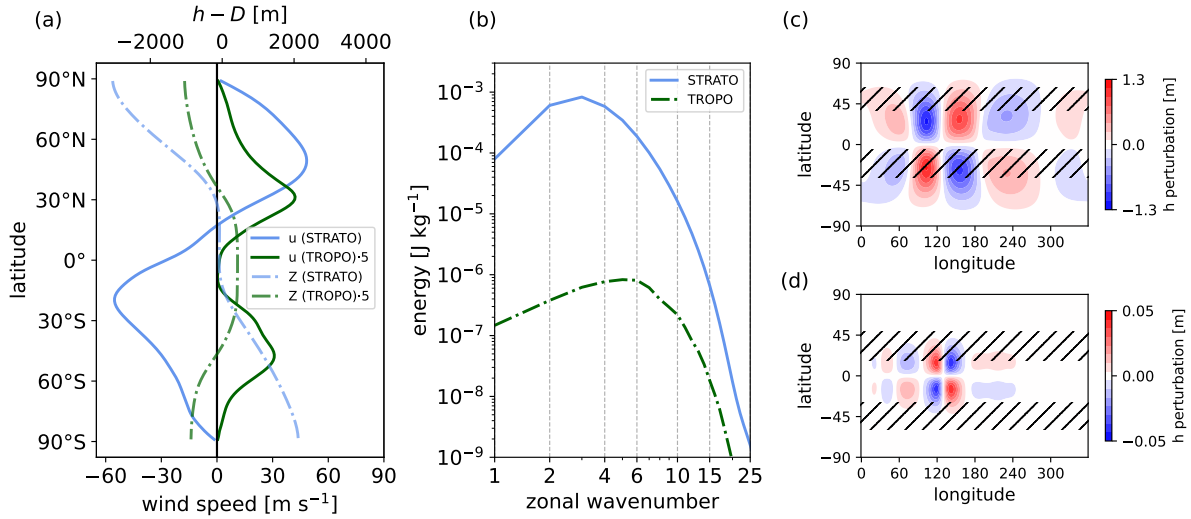


**Figure B2.** Setup and results of numerical simulations using the background zonal wind profiles derived from ERA5 at 200 hPa and 1 hPa, denoted TROPO and STRATO simulations, respectively. (a) Background zonal flows of TROPO and STRATO. The balanced height fields are shown (dashed curves) as fluid depth perturbation from the mean depth  $D$ . TROPO profiles are multiplied by a factor of 5. (b) MRG wave total energy spectra averaged over the first 2 days of simulation time. (c)-(d) Horizontal structure of the MRG wave geopotential height on day 2 (shades) in (c) STRATO and (d) TROPO simulations. Hatches denote the location of the zonal jet amplitude maxima.

The MRG total (kinetic+potential) energy spectra are presented in Figure B2b showing MRG wave energy maxima at planetary scales ( $k = 3$ ) and at synoptic scales ( $k = 6$ ) in the STRATO and TROPO simulations, respectively. These wavenumbers correspond to the peak scales depicted in the ERA5 climatological spectra in Figure B1. Besides the peak scales, simulated spectra also are more energetic in the STRATO case than in the TROPO simulation, which is qualitatively similar to the reanalyses and primarily due to the stronger background flow. The horizontal structure of the excited MRG waves is shown in Figure B2 (c)-(d), which illustrates not only the larger zonal but also the larger meridional scale, i.e., the stratospheric

MRG waves extend further away from the equator compared to their tropospheric counterparts. This is because of different mean depths that define the equatorial deformation radius, i.e., the meridional extent of the MRG wave. It can also be noticed that the jet maxima in both simulations are located within the meridional scales of the MRG waves, which is a necessary requirement for the MRG wave growth by wave-mean flow interactions.

By diagnosing wave-mean flow and wave-wave interactions, we find that the former is the main contributor to the MRG wave growth, as discussed in Mahó et al. (2024b). The wave-mean flow interactions are most active in a relatively small range of  $k$  that is significantly different for TROPO and STRATO (see Section B15.3). During the MRG wave life cycle, energy is transferred from the symmetric Rossby waves to the MRG waves. The symmetric waves mostly originate from the symmetric initial height perturbation. With time, new species of symmetric and asymmetric waves are generated through triad (i.e., non-linear wave-wave) interactions. However, their amplitudes are small within the analyzed time window (2 days), and therefore their contributions to the MRG wave growth are negligible. The mean state is quasi-steady in all simulations, meaning that there is no barotropic instability, which could influence energy flow between the waves and the mean state.

## **B11 Sensitivity of the MRG scale selection to the jet central latitude**

Now we investigate how the position of the jet influences the zonal scale of MRG waves. For this purpose we perform a series of idealised simulations with the background zonal jet centred at various latitudes. The jet profile is prescribed analytically and the balanced geopotential height profile is computed as for the experiments in Section B10. The central latitude of the jet varies between  $10^\circ\text{N}$  and  $50^\circ\text{N}$  (Figure B3a). Every simulation applies the same symmetric initial height perturbation as in Section B10 with the e-folding scales set to  $10^\circ$  and amplitude of 5% of the applied mean depths,  $D = 400$  m and  $D = 10$  km.

The resulting MRG wave energy spectra for  $D = 10$  km are combined in Figure B3b showing that the most energetic scale of the excited MRG waves depends on the jet position such that the peak scale moves to the smaller zonal wavenumber as the jet shifts poleward. For example, the simulation with the jet centred at  $\varphi = 50^\circ\text{N}$  and at  $\varphi = 10^\circ\text{N}$  excites MRG waves with the largest energy at  $k = 2$  and  $k = 9$ , respectively.

Similar scale shifts are found in the case of  $D = 400$  m (Section B15.4), except that the MRG wave energy spectra have smaller amplitudes with respect to  $D = 10$  km, especially in simulations with the jet in midlatitudes (i.e. jets centred in between  $40^\circ$  and  $50^\circ$ ). This is because

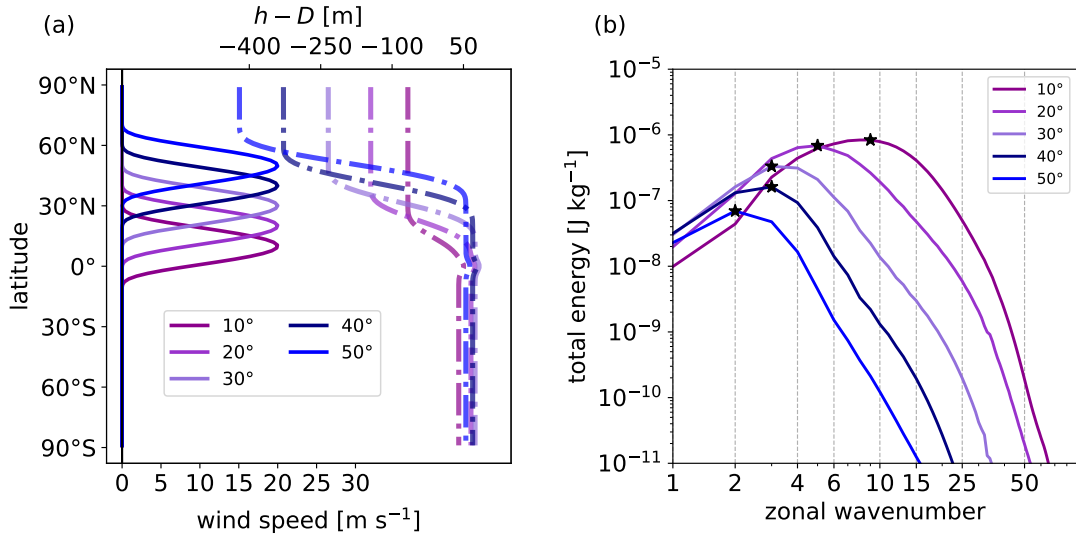


**Figure B3.** (a) Latitudinal profiles of the zonal jets centred at 10°, 20°, 30°, 40°, and 50°N in the idealised TIGAR simulations with  $D = 10$  km. The balanced height fields are also shown (dashed curves) as fluid depth perturbation from the mean depth. (b) MRG wave energy spectra in response to wave-mean flow interactions involving the idealised jets at different latitudes.

the meridional MRG wave scale is more bounded to the equator as  $D$  reduces, meaning that wave-mean flow interactions in midlatitudes occur too far away with respect to the meridional scale of the MRG wave.

More generally, the increase in the zonal scale of the MRG waves with the poleward movement of the jet is associated with the meridional scale of the spherical MRG waves, which depends both on  $k$  and  $D$  (Boyd, 2018; Paldor et al., 2018). In the limit of small values of the Lamb parameter  $\varepsilon = (2a\Omega)^2 / (gD)$ , where  $g$ ,  $a$ , and  $\Omega$  stand for gravity, radius of the Earth and Earth’s rotation rate, the meridional scale of the MRG wave reduces with increasing zonal wavenumber (Paldor et al., 2018) implying a stronger equatorial trapping. This wavenumber effect is especially true for mean depths larger than 400 m (see Section B15.4). Therefore, wave-mean flow interactions cannot project on small-scale MRG waves when the jet is located in midlatitudes, which leads to the dominance of planetary-scale MRG waves. In contrast, when the jet is closer to the equator, the interactions project stronger on smaller-scale MRG waves.

## B12 Discussion and Conclusions

We explained the MRG wave scale selection as being associated with the jet position: the closer the jet to the equator, the larger the zonal wavenumber of the MRG waves excited by wave-mean flow interactions. Our theory and the results of idealised simulations are corroborated

by simulations using the zonal jet profile derived from ERA5 data at levels representative for the upper troposphere (200 hPa) and the stratosphere (1 hPa). To further connect the results of idealised simulations with observational data, we computed the central latitudes of jets from daily ERA5 data during 15 years by finding local maxima in the zonal mean zonal wind field in each hemisphere. Details of the computations are given in Section B15.5. Generally, we find that the position of the stronger jet among the two hemispheres, which controls the MRG excitation scale, is around  $31^\circ$  in the upper troposphere, whereas in the upper stratosphere it is near  $50^\circ$  in DJF and JJA. Thus the climatological positions of the tropospheric and stratospheric jets support the wave-mean flow interaction mechanism as responsible for the planetary-scale ( $k = 2 - 3$ ) MRG waves in the upper stratosphere and the synoptic-scale ( $k = 5 - 6$ ) MRG waves in the upper troposphere.

We have shown that the dependence of the MRG wave meridional scale on the zonal wavenumber is a crucial factor for the MRG scale selection, which is only a feature of spherical MRG waves (Boyd, 2018; Paldor et al., 2018). A relative sparseness of idealised studies of equatorial waves using a spherical approach may explain why the mechanism of the MRG scale selection has remained elusive for so long. Had this study been performed with an equatorial  $\beta$ -plane shallow water model, we would not have detected the jet position as an important factor for the MRG scale selection.

Our simulations require a wave source to produce initial perturbations for the wave-mean flow interaction process. Such perturbations have likely different sources in the upper troposphere and stratosphere. Equatorial waves excited by convective sources in the troposphere have been well studied theoretically (e.g., Salby and Garcia, 1987; Garcia and Salby, 1987), in observations (e.g., Hayashi, 1971; Wheeler and Kiladis, 1999) and models (e.g., Kasahara, 1984; Raupp and Dias, 2009) and they may travel sufficiently far away from the equator to trigger the wave-mean flow interactions. In the upper stratosphere, initial perturbations may arrive as vertically-propagating waves from the troposphere or be generated in situ. For instance, shear instabilities in the stratosphere can lead to gravity wave generation, which can propagate upward (Bühler and McIntyre, 1999; Yasui et al., 2018). Furthermore, we considered only the symmetric source in order to exclude the direct MRG wave excitation by asymmetric forcing (Holton, 1972). As demonstrated in Mahó et al. (2024b), such a forcing leads to a nearly flat MRG wave energy spectrum across large scales and makes it more difficult to identify the part of the wave signal due to wave-mean flow interactions in reanalysis data. More realistic simulations with a 3D version of the TIGAR model, currently under development, might provide a more qualitative insight about contributions to the observed MRG wave spectra from different excitation mechanisms.

Finally, our explanation of the scale selection of MRG waves in the upper troposphere

and the upper stratosphere has important implications for the MRG wave diagnostics and predictability in weather and climate models. The key element of our scale-selection mechanism is the latitude of the zonal jet. Its accurate representation in the initial state for weather forecasts is thus suggested as crucial for the MRG wave predictability.

## **B13 Open research**

ERA5 data were obtained from Copernicus Climate Change Service (C3S, 2017) accessed on 15-JUN-2023. Data distribution by the German Climate Computing Center (DKRZ). The default version of the MODES software is available via <https://modes.cen.uni-hamburg.de/>. The TIGAR simulations presented in this paper are available at <https://doi.org/10.5281/zenodo.11451701> (Mahó et al., 2024a). The description of TIGAR is available at <https://doi.org/10.1002/qj.4006>. All figures were made with Matplotlib version 3.8.0 (Hunter, 2007), available under the Matplotlib license at <https://matplotlib.org/>.

## **B14 Acknowledgements**

This paper is a contribution to the project W6 (Spectral Energy Fluxes by Wave-Wave interactions) of the Collaborative Research Centre TRR 181 "Energy Transfers in Atmosphere and Ocean" funded by the Deutsche Forschungsgemeinschaft (DFG, German Research Foundation) - Projektnummer 274762653. We acknowledge financial support from the Open Access Publication Fund of Universität Hamburg.

## **B15 Supplements**

### **B15.1 Computation of the seasonal climatology of the mixed Rossby-gravity wave energy spectra**

To obtain MRG waves on pressure levels we used the MODES software (Žagar et al., 2015), which computes zonal wind ( $u$ ), meridional wind ( $v$ ) and geopotential height ( $h$ ) perturbations of various Hough harmonics, which are the eigensolutions of the linearized primitive equations on the sphere. The Hough harmonics consist of balanced Rossby and unbalanced inertia-gravity modes, and they also include the equatorial Kelvin and MRG mode. Here, MRG mode and MRG wave are equivalent terms. MODES performs the normal-mode function decomposition (NMD), which has been recently extended to the pressure system as described in Žagar et al. (2023). The NMD procedure is described extensively in Žagar et al. (2015). Here we only

provide details necessary to understand how we produced the MRG wave seasonal climatology data and refer the reader to Žagar et al. (2015) for a full description of the method.

The input data for the NMD procedure is taken from ERA5 reanalysis (Hersbach et al., 2020) consisting of temperature, zonal wind, meridional wind on 137 pressure levels extending up to 0.01 hPa. Furthermore, the input data also includes surface geopotential and mean sea level pressure. We took daily data from 12 UTC for a 15-year period in between 2005 and 2019.

We compute Hough coefficients using the truncation of  $K = 200$  zonal wavenumbers for  $M = 50$  vertical modes. The projection includes  $120 \times 3 = 360$  meridional modes encompassing 120 eastward and westward propagating inertia-gravity, and Rossby modes. Equivalent depths range from 10029.4 m to 8.5 m.

The analysis in grid point space considers a  $400 \times 800$  regular Gaussian grid. The MRG wave signal in grid point space on a single pressure level can be obtained by a summation of single MRG waves of different vertical modes ( $m$ ) and zonal wavenumbers ( $k$ ). A single MRG wave for a particular  $k$  and  $m$  at time  $t$  is obtained by multiplying the Hough harmonic with indices  $k$  and  $m$  by the corresponding Hough coefficient, vertical structure function for the mode  $m$  and the scaling matrix of this vertical mode. The computation of the complete MRG wave signal at time  $t$  for a single point reads as

$$(u, v, h)^T(\lambda, \varphi, p) = \sum_{m=1}^M \sum_{k=-K}^K G_m(p) \mathbf{S}_m \left( u_m^k, v_m^k, h_m^k \right)^T(\lambda, \varphi), \quad (\text{B15.1})$$

where

$$\left( u_m^k, v_m^k, h_m^k \right)^T(\lambda, \varphi) = \chi_m^k \Theta_m^k(\varphi) e^{ik\lambda}. \quad (\text{B15.2})$$

In Equations B15.1 and C20.12  $G_m(p)$  are the pressure ( $p$ ) dependent vertical structure functions (VSFs) of  $m = 1, \dots, M$ . In addition,  $\mathbf{S}_m$  is a scaling diagonal matrix with elements  $(\sqrt{gD_m}, \sqrt{gD_m}, D_m)$ ,  $\chi_m^k$  is the Hough coefficient of the MRG mode and  $\Theta_m^k(\varphi)$  is the meridional MRG Hough function. It is worth mentioning that  $(u_m^k, v_m^k, h_m^k)^T$  contains the MRG mode zonal wind, meridional wind and geopotential height perturbation for a particular  $k$  and  $m$ . The MRG kinetic energy spectra was computed by using the MRG wave  $u$  and  $v$  field in gridpoint space taken from of the 1 hPa and 200 hPa levels. For obtaining the spectral coefficients at different zonal wavenumbers, we used spherical harmonic decomposition.

The horizontal structure of the spherical  $k = 1$  MRG wave is shown by Figure B4. More details about obtaining the 3 dimensional structure of Hough harmonics are given in Žagar et al. (2022) and in Neduhál et al. (2024).

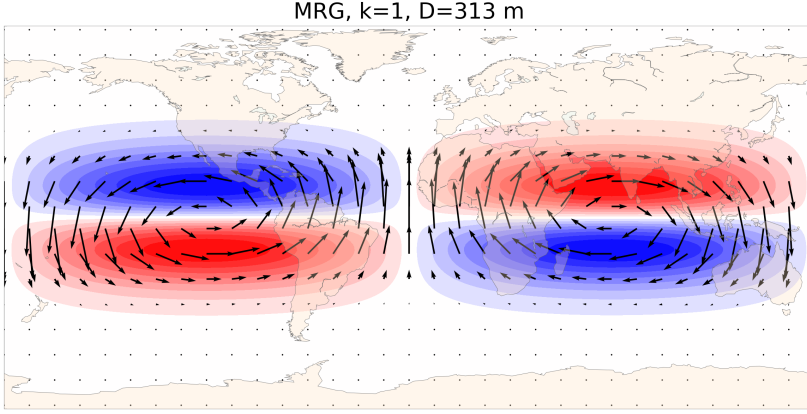


**Figure B4.** The horizontal structure of the spherical MRG wave of  $k = 1$  at an equivalent depth of 313 m. Shading denotes the geopotential height perturbation, with positive and negative values shown as red and blue respectively. The vectors denote the wind vectors related to the MRG wave. Adopted from <https://modes.cen.uni-hamburg.de>

## B15.2 Details of the experimental setup

We employ the TIGAR model (Vasylkevych and Žagar, 2021) that solves the non-linear rotating shallow water equations, which are given by Equation B15.3 in vector format as

$$\frac{\partial}{\partial t} \mathbf{x} + \mathbf{L} \mathbf{x} = \mathbf{N}, \quad (\text{B15.3})$$

where  $\mathbf{x} = [u, v, h]$  is the state variable vector,  $\mathbf{L}$  is the linear operator and  $\mathbf{N}$  includes wave-wave and wave-mean flow interactions. The state variables are the zonal and meridional wind ( $u$  and  $v$  respectively), and the total fluid depth ( $h$ ). Term  $\mathbf{N}$  includes the advection, the metric and the divergence terms.

TIGAR is a spectral model as it uses Hough harmonics as the spectral expansion basis (Equation B15.4). The Hough harmonics are the eigensolutions of the linearized shallow water equations. The solutions form an orthonormal set and they include low-frequency Rossby, high frequency inertia-gravity (IG) waves as well as the Kelvin and the MRG wave. The Hough harmonics are indexed by zonal wavenumber  $k$ , meridional index  $n$  and wave type  $l$ . The former takes the value of 1, 2 or 3 for Rossby, eastward and westward propagating IG waves respectively. Thus,

$$[u, v, h]^T(\lambda, \phi, t) = \sum_{k,n,l} \chi_{n,l}^k(t) \mathbf{H}_{n,l}^k(\lambda, \phi). \quad (\text{B15.4})$$

where,  $\mathbf{H}_{n,l}^k$  is the Hough harmonic defined as  $\mathbf{H}_{n,l}^k(\lambda, \phi) = [U_{n,l}^k, iV_{n,l}^k, Z_{n,l}^k]^T(\phi) e^{ik\lambda}$  where

$U_{n,l}^k$ ,  $V_{n,l}^k$  and  $Z_{n,l}^k$  are the Hough functions for zonal wind, meridional wind and geopotential height. In Equation B15.4,  $\chi_{n,l}^k$  is the time-dependent Hough expansion coefficient of mode  $(k, n, l)$ , which is the model prognostic variable. For the zonal mean state ( $k = 0$ ) the so-called K-modes are used as derived by Kasahara (1978). The MRG wave is the  $n = 0$  Rossby mode.

For  $\chi_{n,l}^k$  TIGAR solves an ODE

$$\frac{d}{d\tilde{t}} \chi_{n,l}^k(\tilde{t}) + i\tilde{\omega}_{n,l}^k \chi_{n,l}^k(\tilde{t}) = f_{n,l}^k(\tilde{t}) \quad (\text{B15.5})$$

where  $\tilde{\omega}_{n,l}^k$  is non-dimensional eigenfrequency and  $f_{n,l}^k(\tilde{t})$  is the projection of term  $\mathbf{N}$  onto the Hough harmonics;

$$f_{n,l}^k = \frac{1}{2\pi} \int_0^{2\pi} \int_{-\pi/2}^{\pi/2} \mathbf{N} \left( \sum_{k',n',l'} \chi_{n',l'}^{k'} \mathbf{H}_{n',l'}^{k'} \right) \cdot \left( \mathbf{H}_{n,l}^k \right)^* (\lambda, \varphi) d\varphi d\lambda. \quad (\text{B15.6})$$

The computation of nonlinear terms is pseudospectral: first  $u$ ,  $v$ , and  $h$  and their derivatives are evaluated in physical space from Hough expansion using FFT in zonal and Hough transform in the meridional direction, then  $\mathbf{N}$  is computed in physical space.

In this formulation, the MRG wave appear as a subset of the prognostic variable over the whole range of zonal wavenumbers. Thus, processes changing the MRG wave tendencies are quantifiable. In our experiments, the MRG waves are not initialized, therefore only the  $f_{n,l}^k$  term can produce such waves. We can further filter term  $f_{n,l}^k$ , which is quadratic, into interactions of arbitrary modes. For example, we can diagnose wave-wave and wave-mean flow interactions contributing to the MRG wave tendencies. Wave-wave interactions are defined as interactions between  $k > 0$  modes, whereas wave-mean flow interactions are between  $k = 0$  Rossby and  $k > 0$  modes. Total (kinetic+available potential) energy in every mode is given by the square of the modulus of its Hough expansion coefficient as described in Žagar et al. (2015, Section 2.5).

As part of the initial conditions we apply a Gaussian height perturbation in all simulations as follows:

$$h' = A \exp \left( -\frac{(\lambda - \lambda_0)^2}{2L_x^2} - \frac{(\varphi - \varphi_0)^2}{2L_y^2} \right), \quad (\text{B15.7})$$

where  $A$ ,  $(\lambda_0, \varphi_0)$ ,  $L_x$  and  $L_y$  are the perturbation's amplitude, central longitude/latitude, zonal and meridional e-folding scale, respectively. In all simulations the height perturbation is symmetric ( $\varphi_0 = 0$ ) and  $A$  is 5% of the mean depth. The scales  $L_x$  and  $L_y$  are equal, and they correspond to the equatorial deformation radius for the TROPO and STRATO case ( $10.54^\circ$  and  $23.66^\circ$  respectively). In the idealised simulations with the analytical jets (Section III),  $L_x$  and  $L_y$  are set

equal to  $10^\circ$ .

We apply  $D = 10$  km for the STRATO simulation and  $D = 400$  m for the TROPO simulation (Section II), whereas we use both mean depths for the idealised jet simulations (Section III).  $D$  is the eigensolution of the vertical structure equation that appears in the normal-mode decomposition of atmospheric data (Žagar et al., 2015). Note that  $D = 10$  km corresponds to the barotropic vertical mode; and  $D = 400$  m is an internal baroclinic mode that is associated with deep convection, thus presumed to represent a significant portion of tropical wave variance as demonstrated by Žagar et al. (2022) for the Kelvin wave. The barotropic or the Lamb mode is relevant for planetary waves observed in the middle atmosphere as shown for example by Salby (1981) and Hirooka and Hirota (1985). In both STRATO and TROPO experiments, the eigenfrequencies of the MRG waves are close to the observed values reported by Zangvil and Yanai (1980) and Randel et al. (1990).

Numerical experiments are performed with a spectral resolution of T85 and timestep of 10 minutes. We use the fourth-order exponential Runge-Kutta method for time integration.

For completeness of the presentation, the formulation of the geostrophic zonal steady states for the model is shown, following Appendix B of Mahó et al. (2024b). The zonal steady states of the spherical non-linear rotating shallow water equations satisfy the equations

$$u \left( 2\Omega \sin \varphi + \frac{u}{a} \tan \varphi \right) = -\frac{g}{a} \frac{\partial h}{\partial \varphi}, \quad (\text{B15.8a})$$

$$\text{where } v = 0, \quad u = u(\varphi), \quad h = h(\varphi). \quad (\text{B15.8b})$$

The mean state Rossby modes ( $k = 0, l = 1$ ) are the geostrophic steady states of linearized RSW equations, meaning that

$$\sin \varphi \Theta_u = -\gamma \frac{\partial \Theta_h}{\partial \varphi}, \quad \Theta_v = 0. \quad (\text{B15.9})$$

Given a zonal velocity profile  $u(\varphi)$  derived from e.g. reanalysis, the zonal steady state can be constructed from the set of  $k = 0$  Rossby modes as follows. First, we rewrite Equation B15.8a as

$$\sin \varphi \left( \tilde{u} + \frac{\gamma \tilde{u}^2}{\cos \varphi} \right) = -\gamma \frac{\partial \tilde{h}}{\partial \varphi}. \quad (\text{B15.10})$$

We expand the modified velocity  $\hat{u} = \tilde{u} + \frac{\gamma \tilde{u}^2}{\cos \varphi}$  over the basis of  $k = 0$  Rossby zonal velocity components, as

$$\hat{u} = \sum_n C_n (\Theta_u)_{n,1}^0. \quad (\text{B15.11})$$

Then, the set  $[\tilde{u}, 0, \tilde{h}]^T$ , where

$$\tilde{h} = \sum_n C_n (\Theta_h)_{n,1}^0 \quad (\text{B15.12})$$

satisfies Equation B15.10 and, therefore, is the the desired zonal steady state.

### B15.3 MRG wave energy tendencies in the TROPO and STRATO simulations

Here we elaborate on interactions between  $k = 0$  Rossby and  $k > 0$  modes projecting onto the MRG mode, i.e. wave-mean flow interactions. We quantify the MRG wave energy tendency modified by wave-mean flow interactions (Figure B5). For details of the computation see Equation 8 in Mahó et al. (2024b). It can be seen that the interactions are the most active in a relatively small range of  $k$ . In case of STRATO, the interactions are strongest at  $k = 2 - 3$ . These wavenumbers correspond to the selected planetary scale MRG waves as shown by Figure B1. In the TROPO simulation the most active zonal wavenumber range of the wave-mean flow interactions is at  $k = 4 - 8$ , which also matches the selected synoptic-scale MRG waves. Note that the interactions are two orders of magnitude more energetic in the STRATO simulation, which matches the difference in wave amplitudes revealed by Figure B2b of the paper.

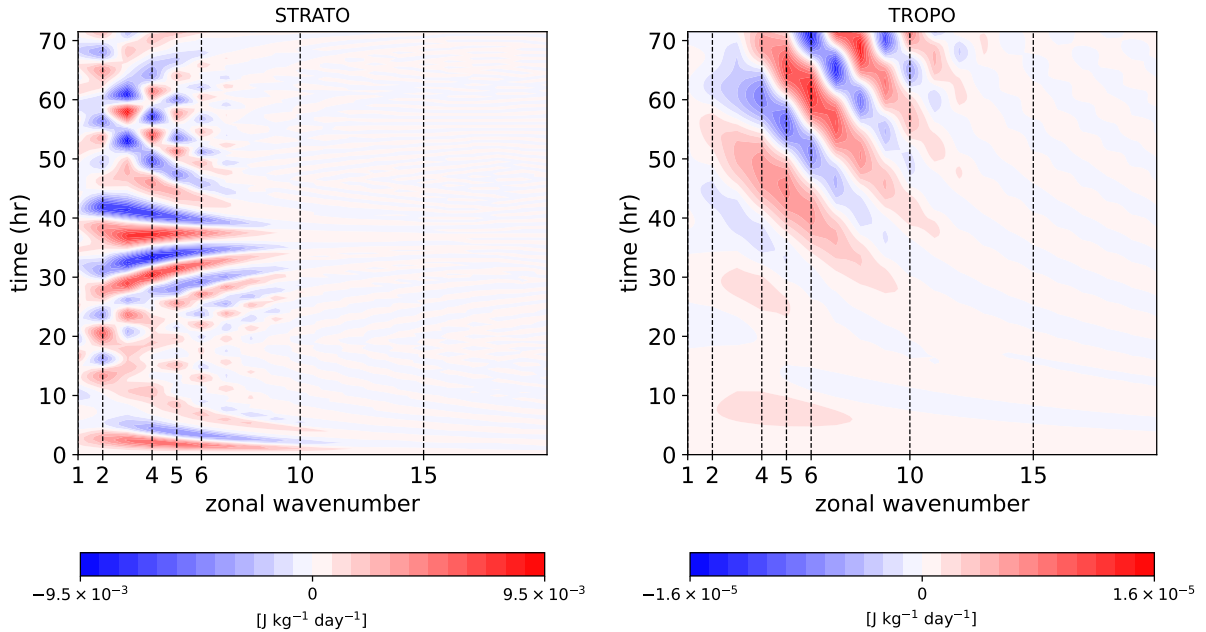


**Figure B5.** MRG wave energy tendencies (expressed in  $\text{J/kg/day}$ ) due to wave-mean flow interactions as a function of zonal wavenumber and time in the (a) STRATO and (b) TROPO simulation.

## B15.4 Further aspects of the MRG wave scale selection in relation to the zonal jet position

MRG energy spectra in the idealised simulations with varying jet position described in the main article are shown in Figure B6 for  $D = 400$  m. This figure can be compared with Figure B3 in the main article. The two figures show a similar shift of the MRG wave peak wavenumber towards smaller scales as the jet is moved closer to the equator. However, the large-scale MRG waves have reduced magnitude for  $D = 400$  m, which is due to the diminished MRG meridional scale for the smaller  $D$ .

The effect of the zonal wavenumber in the MRG meridional scale is summarized by Table B1 for different mean depths following Paldor et al. (2018). We compare latitudes where the MRG meridional wind amplitude is below 5% of its maximum for  $k = 1$  and  $k = 9$  MRG waves, which are the minimum and the maximum zonal scale of the excited waves. For  $D$  smaller than 400 m, the meridional MRG wave scale dependence on zonal wavenumber practically vanishes, meaning that the jet position has no effect on the MRG scale selection. This would be the case for example for convectively coupled MRG waves, which have been reported to have small equivalent depths (Wheeler et al., 2000).

This dependence also explains the flat MRG energy spectra in case of midlatitude jets in Figure B6. In the case of  $D = 400$  m, the  $k = 1$  MRG wave scale extends up to about  $36^\circ$ , which means that jets far beyond this latitude essentially cannot excite the MRG wave with such a small  $D$ .

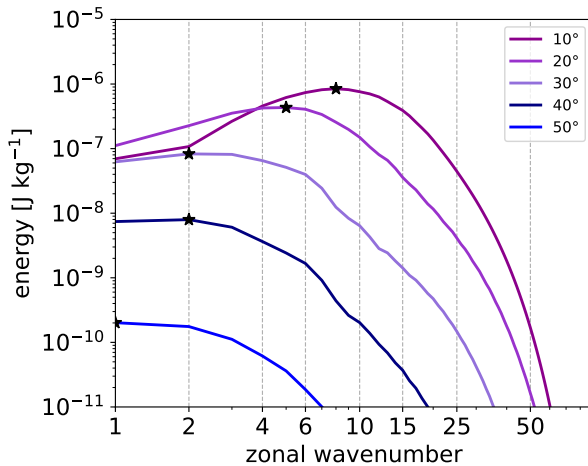


**Figure B6.** MRG wave energy spectra in response to wave-mean flow interactions involving the idealised jets at different latitudes for  $D = 400$  m.

**Table B1.** Dependence of the MRG wave meridional scale on the zonal wavenumber  $k$  and mean depth  $D$ . Columns “ $k = 1$ ” and “ $k = 9$ ” refers to the critical latitude of the MRG wave with the zonal wavenumber  $k = 1$  and  $k = 9$ . The critical latitude is the location where the MRG meridional wind amplitude is below 5% of its maximal value (at the equator). The column  $\Delta^\circ$  contains differences between the critical latitudes for the zonal wavenumbers 1 and 9.

<b>D</b>	<b>k=1</b>	<b>k=9</b>	<b><math>\Delta^\circ</math></b>
<b>25 m</b>	18.60°	18.60°	0°
<b>200 m</b>	30.67°	29.66°	1.01°
<b>400 m</b>	35.7°	33.69°	2.01°
<b>7 km</b>	63.85°	43.74°	20.11°
<b>10 km</b>	67.88°	43.74°	24.14°

### B15.5 Determination of the jet position from zonally-averaged zonal wind data

**Table B2.** Derived jet positions of 200 and 1 hPa for the Northern and the Southern Hemispheres (NH and SH respectively) in different seasons. The values shown with red denote the stronger jet in each season.

	<b>200 hPa</b>		<b>1 hPa</b>	
	<i>NH</i>	<i>SH</i>	<i>NH</i>	<i>SH</i>
<b>JJA</b>	42.2°	<b>30.2°</b>	29.0°	<b>49.3°</b>
<b>DJF</b>	<b>31.7°</b>	40.2°	<b>51.9°</b>	20.9°
<b>SON</b>	38.2°	<b>31.7°</b>		
<b>MAM</b>	<b>31.4°</b>	33.6°		

We derived jet position climatology in the upper troposphere (200 hPa) and stratosphere (1 hPa) by using 15 years of ERA5 daily data (2006-2020). We computed seasonal mean jet locations both for the upper troposphere and the upper stratosphere, however for the latter case we only considered the DJF and JJA seasons, in which an easterly and a westerly jet form on the summer and the winter hemisphere, respectively.

To compute the jet position, first we detected local maxima in the zonal mean zonal wind field separately for the two hemispheres at each timestep. The jet driving the MRG wave excitation is associated with the local zonal wind maximum closest to the equator. We reject local maxima, which are too weak in amplitude or outside of a pre-defined latitude zone. This

latitude zone is in between  $20^\circ$  and  $47^\circ$  for the tropospheric subtropical jet defined to capture the subtropical jet and exclude the polar jet regions. For the stratospheric jets, we searched for local maxima in the region between  $10^\circ$  and  $70^\circ$ . Weak local wind maxima, which were below  $U(t) - 2\sigma(t)$  for the troposphere, and  $U(t) - 0.33\sigma(t)$  for the stratosphere, are also excluded. Here  $U$  and  $\sigma$  are equal to the maximum and the standard deviation of the zonal mean zonal wind at time  $t$ . The difference in the wind amplitude criterion between the two layers is due to the variance of the zonal-mean zonal wind maximum, which is larger in the upper stratosphere by a factor of 6. The results are summarized in Table B2.

# Appendix C: The effect of barotropic instability on mixed Rossby-gravity wave variability during the QBO phases

This paper is prepared for submission to Weather and Climate Dynamics as

- Mahó, S.I., Lunkeit, F., Žagar, N. & Vasylykevych, S. (2024) The effect of barotropic instability on mixed Rossby-gravity wave variability during the QBO phases. *To be submitted to Weather and Climate Dynamics*

Author contributions

- Mahó S.I. contributed to conceptualization, data curation, formal analysis, investigation, methodology, visualization and writing the original draft.
- Lunkeit F. contributed to methodology, data curation, formal analysis, supervision and editing.
- Žagar, N. contributed to the project administration, methodology, supervision, editing, and providing the software.
- Vasylykevych, S. contributed to methodology, providing the software, supervision and editing.

# The effect of barotropic instability on mixed Rossby-gravity wave variability during the QBO phases

Sándor István Mahó<sup>1</sup>, Frank Lunkeit<sup>1</sup>, Nedjeljka Žagar<sup>1</sup>, Sergiy Vasylkevych<sup>1</sup>

<sup>1</sup> Meteorological Institute, Center for Earth System Research and Sustainability, Universität Hamburg, Hamburg, Germany

## Abstract

The quasi-biennial oscillation (QBO), which is the dominant mode of variability in the stratosphere, has been shown to be partially driven by vertically propagating mixed Rossby-gravity (MRG) waves. On the other hand, there is evidence that MRG waves, instead of vertical propagation, are being generated locally in the stratosphere by the barotropic instability development of the QBO-related zonal circulation. However, it is not understood how instability development affect the growth of MRG waves, nor how frequently barotropic instability is satisfied in the stratosphere. By conducting a long-term analysis on the occurrence of instability of the 30 hPa zonal mean flow, we found that the equatorial region, where the QBO is active, satisfies the conditions for barotropic instability about 60% of the total cases with 2 times more instability occurrence during the westerly QBO phase compared to the easterly phase. Analysis of the unstable modes of the shallow water system linearized around the 30 hPa zonal mean flow shows that the instability development of the QBO region favours synoptic and subsynoptic scale MRG wave growth, especially during the westerly QBO phase. We have also found that the zonal wavenumber range of 6 – 8 is the most sensitive for MRG wave growth by barotropic instability. On the contrary, the large scale unstable modes are connected to extratropical barotropic instability, which does not affect MRG wave growth. These unstable modes obtain significantly larger growth rates compared to the modes related to the QBO region. Overall, we argue that the kinetic energy excess of the westerly QBO phase compared to the easterly phase can be explained by barotropic instability development of the QBO circulation at synoptic and subsynoptic scales.

## C16 Introduction

Dynamical instabilities facilitate rapid growth of small amplitude perturbations, thereby acting as wave sources in the atmosphere. Barotropic instability, which is related to the reversal of the meridional gradient of the absolute vorticity of the mean flow, can influence the growth of mixed Rossby-gravity (MRG) waves, which we study in this paper by focusing on the equatorial stratosphere where the quasi-biennial oscillation (QBO) is active.

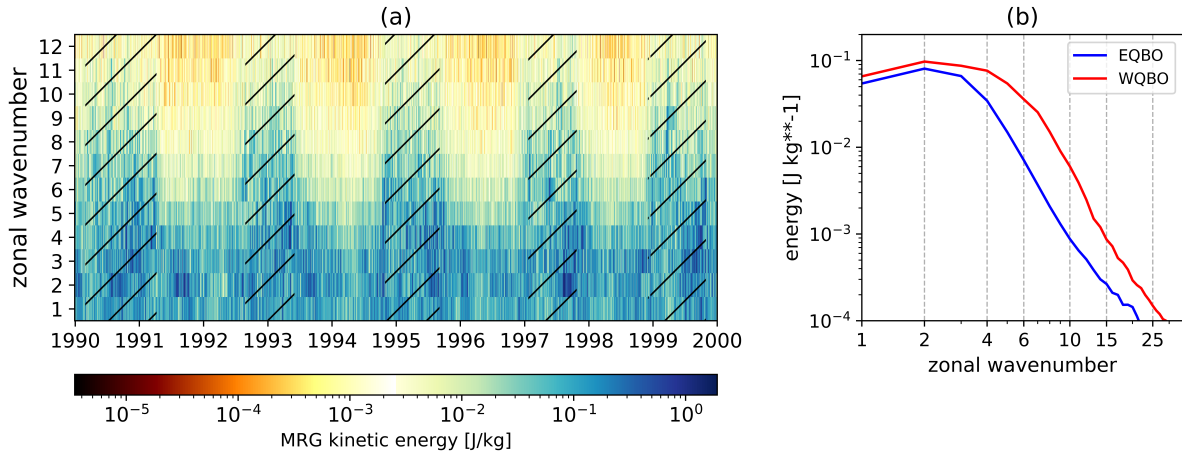


**Figure C1.** (a) 30 hPa MRG wave kinetic energy with respect to time and zonal wavenumber in the period of 1990-1999. The hatches denote the timesteps during the WQBO phase. (b) 30 hPa MRG wave kinetic energy spectra for the EQBO and WQBO phase (blue and red respectively) averaged for 1990-1999.

MRG waves are westward moving low-frequency disturbances in the equatorial atmosphere, which were first derived theoretically by Matsuno (1966) and first observed by Yanai and Maruyama (1966). These waves are present throughout the troposphere and the stratosphere with peak amplitudes in the upper troposphere and the upper stratosphere (Zangvil and Yanai, 1980; Randel et al., 1990; ?). Nevertheless, the MRG wave amplitudes are non-negligible in the QBO region, which reach about 10-30% of the MRG waves present in the upper troposphere (Žagar, 2015). Another important feature of instantaneous MRG waves is the lack of vertical wave propagation between the troposphere and the stratosphere (Žagar, 2015) implying local wave generation in the stratosphere. ? showed that MRG waves at 1 hPa are likely produced by wave-mean flow interactions locally, however, at 30 hPa, which is a representative level for the QBO, the MRG wave variability might be driven by barotropic instability of the QBO region. The 30 hPa MRG wave kinetic energy, which is derived from ERA5 data (Hersbach et al., 2020) by using the MODES software (Žagar et al., 2015) (see Section C20) indeed implies that MRG waves are related to the QBO, since MRG waves of zonal wavenumbers  $k > 5$  correlate well

with the QBO phases (Figure C1a). Notice as well that there is excess of MRG wave activity during the westerly QBO phase across all zonal wavenumbers (Figure C1b), which is consistent with satellite observations (e.g., Ern et al., 2008). Note also that the largest difference between the QBO phases are found in range of synoptic and subsynoptic scales (i.e.  $k = 5 - 15$ ). In the following, we argue that the presented MRG wave kinetic energy differences between the QBO phases can be explained by barotropic instability development of the QBO region.

The QBO is the dominant mode of variability of the equatorial stratosphere at 10-70 hPa with alternating downward propagating easterly and westerly zonal wind regimes with an average period of 28 months (Baldwin et al., 2001). As part of the early theories for the existence of the QBO, Holton and Lindzen (1972) hypothesised that eastward moving Kelvin and westward moving MRG waves contribute to the westerly and the easterly acceleration of the QBO, respectively. However, observations (Alexander and Ortland, 2010; Ern et al., 2014), laboratory-based experiments (Plumb et al., 1978), and QBO-resolving numerical model simulations (Kawatani et al., 2010; Holt et al., 2022; Lee et al., 2024) indicate that a broad spectrum of waves, including equatorially trapped large-scale waves and small-scale gravity waves can provide sufficient forcing for the QBO (Butchart, 2022). Some studies also point out the minor role of MRG waves in forcing the QBO (Kawatani et al., 2010; Holt et al., 2016) and even suggest that these waves may be locally generated by flow instabilities in the stratosphere (Garcia and Richter, 2019).

The barotropic instability of the QBO, which has been raised by numerous studies, appears first in Andrews and McIntyre (1976) who reveals that the meridional profile of the easterly acceleration of the QBO flow can become highly inflected, thereby the resulting mean flow can become barotropically unstable. Hamilton (1984) who utilizes wind observations from 30 and 50 hPa from the tropical region also reports reversal of the absolute vorticity gradient both during the easterly and the westerly QBO phase. By studying ECMWF wind analysis Shuckburgh et al. (2001) argues that eddies centred at  $10^\circ$  with zonal wavenumbers 6-10 are products of barotropic instability development of the westerly QBO jet. Garcia and Richter (2019) simulates the QBO with the Whole Atmosphere Community Climate model and shows that the MRG wave signal is robust where the curvature of the westerly QBO jet is strong arguing that MRG waves are produced by barotropic instability development of the westerly QBO jet. Garcia and Richter (2019) also implies that MRG waves can have an important role in mixing (i.e., redistribution of vorticity) in the equatorial stratosphere, which was also raised by Shuckburgh et al. (2001). Yao and Jablonowski (2015) report occurrence of barotropic instability in QBO simulations with an ensemble of dry GCM dynamical cores, and find increased MRG wave activity in models with strong instability indicators.

In this paper, we argue that the observed MRG wave variability of the QBO region (Figure C1) can be explained by barotropic instability induced wave growth, which is related to the instability of the QBO region. Thereby, the MRG wave generation is local to the stratosphere and not a result of vertical wave propagation. As it is not understood how frequently the QBO circulation satisfy the condition for barotropic instability, we compute statistics on the satisfaction of two instability criteria that are based on the absolute vorticity gradient of the zonal mean flow. We also demonstrate how MRG waves are intensified by barotropic instability in idealised barotropic instability simulations. Finally, we use the linearized shallow water equations to isolate unstable eigenmodes of the 30 hPa flow over a 10-year period to further prove that MRG wave growth is favoured during the westerly QBO phase.

## C17 Data and numerical modelling

In this section, first we discuss the setup of the idealised barotropic instability experiments performed with the TIGAR model (Vasylkevych and Žagar, 2021). Subsequently, we present the barotropic instability analysis of the QBO involving real data. We focus on the 30 hPa level, where the QBO has strong amplitudes. To isolate the QBO phases and to test barotropic instability directly from the absolute vorticity of the background flow, we use the 30 hPa zonally averaged zonal wind data from ERA5 (Hersbach et al., 2020). We also compute eigenmodes of the system linearized around 30 hPa background zonal flow, which is performed by the BGHough software (Holube et al., 2024). From the background eigenmodes, we analyse the instability of the 30 hPa flow in different zonal wavenumbers and the effect of instability on MRG waves. In the following we describe each analysis method and provide the necessary details.

### C17.1 Idealised barotropic instability simulations

To study MRG wave growth by barotropic instability associated with the QBO, we perform idealised barotropic instability experiments including equatorial easterly and westerly jets that mimick the QBO phases. We use the TIGAR model (Vasylkevych and Žagar, 2021) that solves the non-linear rotating shallow water equations on the sphere, which are shown by Equation C17.1 in vector format as

$$\frac{\partial}{\partial t} \mathbf{x} + \mathbf{L}\mathbf{x} = \mathbf{N}, \quad (\text{C17.1})$$

where  $\mathbf{x} = [u, v, h]$  is the vector of the state variables,  $\mathbf{L}$  is the linear operator including the Coriolis effect, the pressure gradient force and the linear part of the divergence term, and  $\mathbf{N}$  includes the horizontal advection terms, the metric terms and the nonlinear part of the divergence

term, thereby incorporating wave-wave and wave-mean flow interactions. The state variables are composed of the zonal and meridional wind ( $u$  and  $v$  respectively), and the total fluid depth ( $h$ ).

TIGAR uses Hough harmonics as the spectral expansion basis, which are the eigensolutions of the linearized shallow water equations (Longuet-Higgins, 1968). The solutions form an orthonormal set and they include low-frequency Rossby, high frequency inertia-gravity (IG) waves as well as the Kelvin and the MRG wave. In this formulation, the MRG wave spectral coefficient acts as a subset of the prognostic variables, meaning that processes changing the MRG wave tendencies can be quantified. More details of the numerical model formulation can be found in Vasylykevych and Žagar (2021) (Sections 2 and 3 therein).

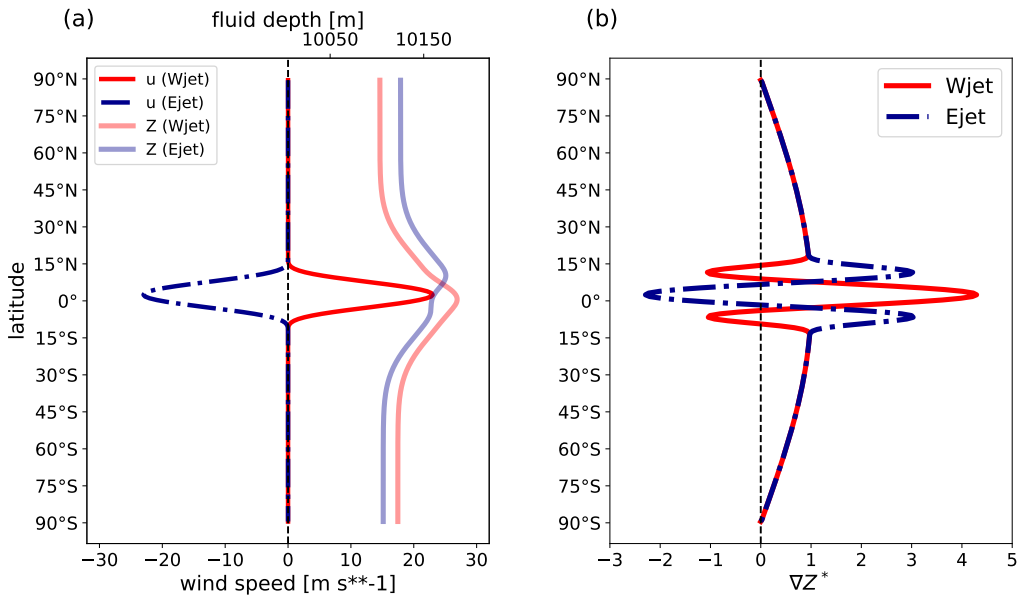


**Figure C2.** Initial balanced zonal background field of the idealised barotropic instability simulations. (a) The zonal wind (bright curves) and the fluid depth field (blurred curves) of the Ejet and Wjet simulations (blue and red, respectively). (b) The non-dimensional barotropic vorticity gradients of Ejet and Wjet flow fields.

We use 10 km as the shallow water mean depth, which corresponds to the barotropic vertical mode. As initial condition, we apply geostrophically balanced jets as background flow (Fig. C2a). Two simulations with different jets are considered: an equatorial easterly and westerly jet named as Ejet and Wjet respectively. Both jets are centred at 2.5°N with a half-width of 10°. As can be followed in Fig. C2b, in case of both jets, the barotropic vorticity gradient (Eq. C17.5) changes sign at the jet flanks, meaning that both flow fields satisfy the criterion for barotropic instability based on Kuo (1949). The balanced zonal height field is computed by projecting the zonal wind onto  $k = 0$  Rossby modes as described in Mahó et al. (2024b). In addition, we apply

an asymmetric Gaussian height perturbation expressed as

$$h' = A \exp \left( -\frac{(\lambda - \lambda_0)^2}{2L_x^2} - \frac{(\varphi - \varphi_0)^2}{2L_y^2} \right), \quad (\text{C17.2})$$

where  $A$ ,  $(\lambda_0, \varphi_0)$ ,  $L_x$  and  $L_y$  are the perturbation's amplitude, central longitude/latitude, zonal and meridional e-folding scale, respectively. In our simulations, the initial perturbation is centred at  $2.5^\circ$  with an amplitude of 500 m, and a zonal and meridional e-folding scale of  $23.6^\circ$  that is close to the equatorial deformation radius. The initial perturbation acts as a wave source, which excites barotropic instability development of the jets, i.e., energy inflow from the mean flow to the waves.

## C17.2 ERA5 zonal wind data

We use daily data of zonally averaged zonal wind from ERA5 from 30 hPa in years 1990-1999 at 0 UTC. To separate the easterly and the westerly QBO phase, we use a similar methodology as in ?. First, the zonal mean zonal wind is averaged in between  $-5^\circ$  and  $5^\circ$  to obtain the equatorial zonal mean wind ( $\bar{u}_{eq}$ ). From  $\bar{u}_{eq}$  we determine the mean ( $\mu$ ) and the standard deviation ( $\sigma$ ), which we use to isolate the westerly QBO phase (WQBO) when

$$\bar{u}_{eq} > \mu + 0.5 \cdot \sigma, \quad (\text{C17.3})$$

and the easterly QBO phase (EQBO), when

$$\bar{u}_{eq} < \mu - 0.5 \cdot \sigma. \quad (\text{C17.4})$$

We apply the Rayleigh-Kuo (RK) (Kuo, 1949) and Ripa's (R83) criterion (Ripa, 1983) for stability conditions of zonal barotropic flows to determine how frequently the 30 hPa zonal mean flow favours the conditions for (barotropic) instability in years 1990-1999. According to the RK criterion, the zonal mean flow is barotropically stable when the meridional absolute vorticity gradient expressed by Eq. (C17.5) obtains the same sign in the whole domain.

$$\nabla Z^* = \frac{1}{2\Omega} \frac{\partial}{\partial \varphi} \left[ f - \frac{1}{a} \frac{\partial \bar{u}}{\partial \varphi} \right] \quad (\text{C17.5})$$

In Eq. (C17.5),  $Z^*$  is the non-dimensional absolute vorticity,  $\bar{u}$  is the zonal mean zonal wind taken from ERA5,  $\Omega$  is the rotation rate of Earth,  $f$  is the Coriolis parameter and  $a$  is the Earth radius. We also use the R83 stability condition, which is derived on the sphere by using the rotating shallow water equations and reads as

$$\frac{1}{a} \frac{\partial Q}{\partial \varphi} \geq 0 \text{ for all } \varphi \text{ and } \max \left( \frac{\bar{u}}{\cos \varphi} \right) \leq \min \left( \frac{\bar{u} + (g\bar{h})^{1/2}}{\cos \varphi} \right), \quad (\text{C17.6})$$

where

$$Q = (\bar{h})^{-1} \left( f - \frac{1}{a \cos \varphi} \frac{\partial \bar{u} \cos \varphi}{\partial \varphi} \right). \quad (\text{C17.7})$$

In Eq. (C17.6) and (C17.7)  $g$  is the Earth's gravity constant and we note that the zonal mean fluid depth  $\bar{h}$  is assumed to be in geostrophic balance with  $\bar{u}$ . The R83 condition basically states that the meridional potential vorticity gradient of the shallow water fluid needs to be non-negative and the maximum of zonal velocity has to be smaller than the local phase speed of long gravity waves in order that the zonal flow maintains stability. To study this stability criterion we used  $D = 10$  km as the shallow water mean depth when computing  $\bar{h}$  from the  $\bar{u}$  field taken from ERA5. We note that using smaller  $D$  for the projection (up to  $D = 1$  km) does not change significantly our results.

### C17.3 Determining unstable background eigenmodes

We carry out a long-term analysis of the eigenmodes of the shallow water system linearized around the 30 hPa zonal mean flow, which enables us to reflect on the barotropic instability of the QBO region and the relation between unstable eigenmodes and MRG wave growth. This analysis also helps us isolate the horizontal scales (i.e., the zonal wavenumbers) sensitive to barotropic instability development of the QBO region.

As the first step, the spherical shallow water equations (i.e. horizontal components of the Laplace tidal equations) are linearized around the 30 hPa zonal mean zonal wind for 5-day timesteps within the period of 1990-1999, which is followed by the computation of the eigenmodes of the linearized equation system (from now on background eigenmodes) by using the BGHough software. Although the description of the software can be found in Holube et al. (2024) (Appendix A therein), for completeness we give here the essential details of the computations. The procedure of BGHough is based on the algorithm proposed by Kasahara (1980). Before running BGHough the balanced zonal mean state  $(\bar{u}(\varphi), \bar{h}(\varphi))$  needs to be prescribed. For the zonal mean wind ( $\bar{u}$ ), we use the 30 hPa zonally averaged zonal mean wind from 1990-1999 taken from ERA5 data (Section C17.2) with 5-day timesteps. Each zonal wind profile is composed of 256 latitudinal grid points. The associated fluid depth ( $\bar{h}$ ) field, which is in geostrophic balance with  $\bar{u}$ , is obtained by projecting  $\bar{u}$  onto  $k = 0$  Rossby modes similarly

as in Mahó et al. (2024b) (Appendix B therein). We apply 10 km as equivalent depth, which corresponds to the barotropic vertical mode. By substituting the wave ansatz

$$\mathbf{W} = [u, v, h]^T = \hat{\mathbf{W}}(\varphi) e^{i(k\lambda - \sigma t)} \quad (\text{C17.8})$$

into the linearized spherical shallow water equations, we obtain

$$(\mathbf{L} - i\sigma\mathbf{I})\hat{\mathbf{W}} + i\mathbf{B}\hat{\mathbf{W}} = 0, \quad (\text{C17.9})$$

where  $\sigma$  is the non-dimensional complex eigenfrequency,  $\mathbf{L}$  is the linear operator,  $\mathbf{I}$  is the identity matrix, and matrix  $\mathbf{B}$  contains the mean state and its derivatives. For more details of the model see Kasahara (1980) (Section 2 therein). We reduce Eq. (C17.9) into an eigenvalue problem by expressing  $\hat{\mathbf{W}}$  with a series of Hough vector functions  $\Theta_r^k$  for a specific zonal wavenumber ( $k$ ) as

$$\hat{\mathbf{W}}^k = \sum_r C_r \Theta_r^k, \quad (\text{C17.10})$$

where  $C_r$  is the Hough expansion coefficient for meridional mode  $r$  running from 1 to  $R$  that is the truncation limit chosen to be 25. We solve the eigenvalue problem separately for zonal wavenumbers 1-12 by the DGEEV routine of the Lapack package.

The outputs of BGHough are the background eigenmodes' horizontal structures  $\mathbf{W}_r^k = [u'(\varphi, \lambda), v'(\varphi, \lambda), h'(\varphi, \lambda)]_k^r$  and the associated eigenfrequency  $\sigma_r^k$ , whose imaginary part gives the modal growth exponent by barotropic instability provided that  $\Im[\sigma_r^k] > 0$ . In each timestep BGHough computes  $25 \times 3$  background eigenmodes classified into westward IG, eastward IG or the Rossby category, therefore for each timestep we analyse  $75 \times 12$  modes. Among these eigenmodes we take into account only the two most unstable ones, i.e. the modes with the largest  $\Im[\sigma]$ , since we found that for each date there is a maximum of two unstable background eigenmodes with significant magnitude of growth exponents.

In the results section we present growth exponents and energetics of unstable background eigenmodes of the 30 hPa flow, which we analyse separately for the easterly and the westerly QBO phases.

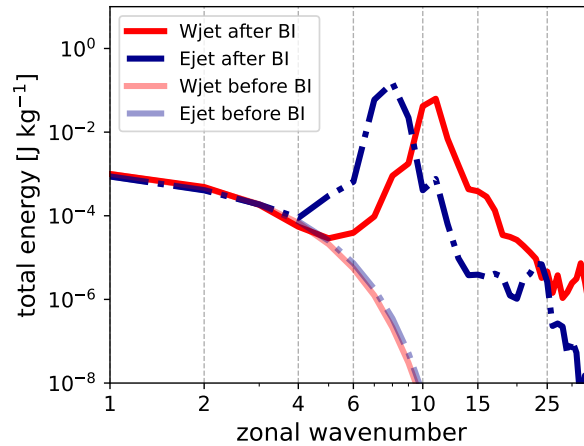


**Figure C3.** MRG wave energy spectra of idealised barotropic instability simulations with an equatorial westerly and easterly jet (Wjet and Ejet respectively). Dull and bright curves represent the spectra before and after the barotropic instability (BI) development of the jets respectively. BI increases the energy of MRG waves and causes the MRG wave spectra to develop peaks in synoptic and subsynoptic scales (i.e. zonal wavenumbers 6-17).

## C18 Results

### C18.1 MRG wave intensification by barotropic instability in idealised simulations

Here we present numerical results from the idealised Wjet and Ejet experiments conducted with a simple atmospheric model, TIGAR (Vasylyevych and Žagar, 2021), which enabled us to study the hypothesized barotropic instability development of the QBO region.

The MRG wave energy spectra before and after the barotropic instability development of Ejet and Wjet are shown by Fig. C3. First of all, MRG waves are instantly excited by the initial perturbation, which is asymmetric, however, we observe rapid growth of MRG waves as a result of barotropic instability development both in case of Ejet and Wjet. The instability development causes the initial red MRG wave energy spectrum to increase by 2-3 orders of magnitude and to develop peaks in synoptic scales. The zonal wavenumbers characteristic to the instability development are at  $k = 8 - 13$  for Wjet and at  $k = 6 - 9$  for Ejet, which are also matching with the most unstable (i.e. the fastest growing) eigenmodes of the shallow water system linearized around Wjet and Ejet (not shown).

To demonstrate the strength of the MRG wave signal caused by instability, Figure C4 shows the Rossby wave field including all Rossby and MRG modes with  $k > 0$  succeeding the breakdown of the equatorial jets due to barotropic instability. Figure C4 clearly demonstrates

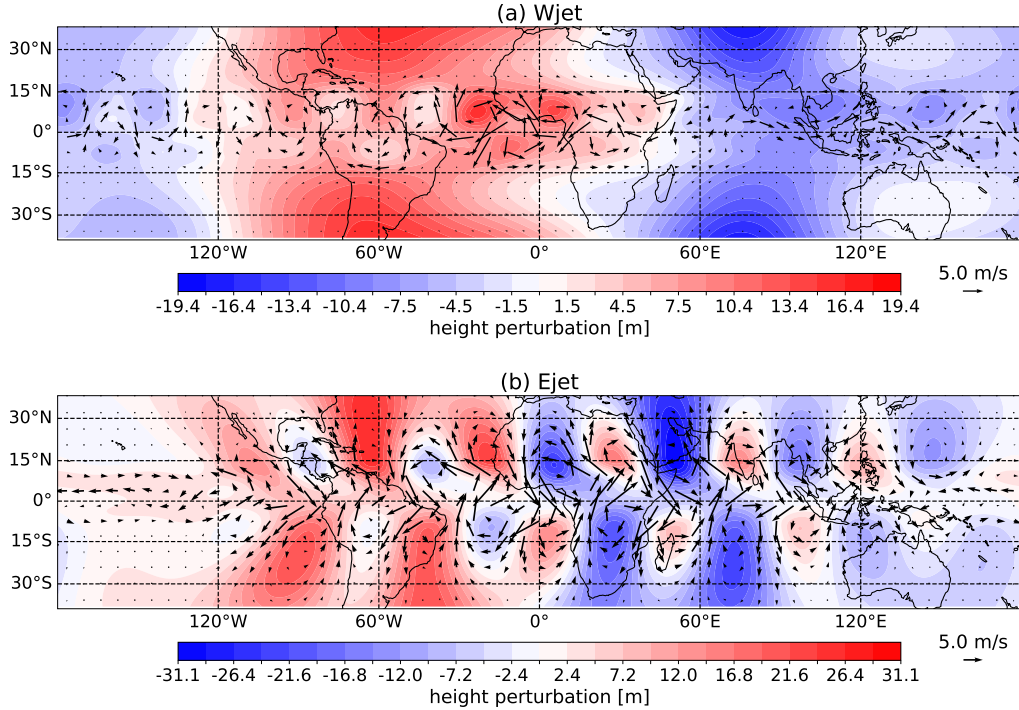


**Figure C4.** Rossby wave field (including MRG waves) in the TIGAR simulation after barotropic instability development of (a) Wjet and (b) Ejet. The shading and the arrows denote the height and the horizontal wind perturbation due to all Rossby waves.

prominent MRG wave-like structures with strong cross-equatorial flow and asymmetric height perturbations both in the Wjet and the Ejet simulations. However, the MRG wave signal is stronger in case of Ejet, which is due to the earlier excitation of barotropic instability with respect to simulation time compared to Wjet. It is also found that MRG waves contribute up to 50% and 25% to the Rossby wave field in case of Ejet and Wjet, respectively. This indicates that any equatorial jet undergoing barotropic instability development will produce vortices crossing the equator with sufficiently large projection onto MRG wave structures, thereby MRG wave growth can indicate excitation of barotropic instability in the QBO region.

## C18.2 Instability of the QBO region

By applying the RK and the R83 criterion for barotropic instability, we produced statistics on the violation of both stability conditions of the 30 hPa zonal mean flow in the tropical region ( $\pm 30^\circ$ ) during all timesteps, the easterly QBO (EQBO) and the westerly QBO (WQBO), and in the extratropics ( $30 - 75^\circ$ ), which is shown by Table C1. As the instability of the QBO-related circulation is connected to the flanks of equatorial jets, the tropical region was chosen to be wide enough to capture instability of the QBO. This is especially important for the circulation related

to the easterly QBO, which often obtains a meridionally extended jet in the tropics (i.e. up to  $30^\circ$ ).

As expected, applying the two stability criteria deliver similar results. It is also noticeable that the tropics are barotropically stable in nearly 40% of the cases, whereas the extratropics are almost always barotropically unstable. There exist also a significant difference between the QBO phases with 2 times more occurrence of barotropic instability in the tropics during the westerly QBO phase.

**Table C1.** Occurrence of barotropic instability (in %) at 30 hPa in 1990-1999 based on the RK and R83 criterion in the tropics ( $\pm 30^\circ$ ) in all analysed dates, during the EQBO and the WQBO phase, and in the extratropics (in latitude zones of  $30 - 75^\circ$ ).

	tropics	tropics EQBO	tropics WQBO	extratropics
<b>RK</b>	60.6%	36.4%	82.1%	99.2%
<b>R83</b>	62.2%	34.9%	74.5%	96.6%

### C18.3 Barotropically unstable modes of the system linearized around the 30 hPa zonal mean flow

Here we present background eigenmodes that are relevant for instability growth of the 30 hPa mean flow. We consider only the first and second fastest growing modes per zonal wavenumber and per timestep during the 10-year analysis period, since other unstable background eigenmodes have negligible growth exponents compared to the first two most unstable ones.

The background eigenmodes can contain significant amounts of MRG waves. To quantify the MRG wave content of a growing background eigenmode, the parameter  $E_{MRG}$  is introduced, which is defined as the ratio of the MRG wave energy and the total energy of the background eigenmode. Based on idealised barotropic instability experiments (see Section C18.1) one would expect a significant growth of MRG waves when the QBO region is barotropically unstable (Fig. C3), meaning that unstable background eigenmodes ought to obtain a large  $E_{MRG}$ . Indeed, in some cases  $E_{MRG}$  of the most unstable background eigenmodes is high, for example as in the case shown in Fig. C5, which depicts the horizontal structure of the fastest growing mode of  $k = 9$  representative of the WQBO phase. Notice that the presented eigenmode is very similar to MRG waves in the tropical region, which is comprised about 60% of MRG waves manifesting that the the QBO region (especially the northern flank of the QBO jet) is barotropically unstable on this date.

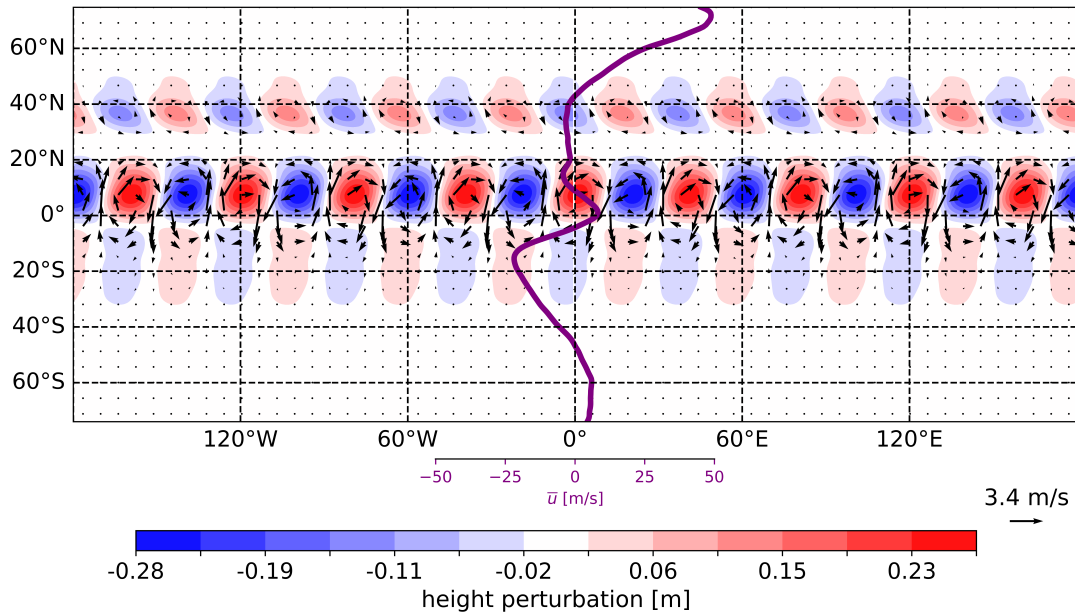


**Figure C5.** Horizontal structure of the most unstable background eigenmode of  $k = 9$  in 1990-03-02 (during WQBO). The period of the eigenmode is 3.5 days. The dimensional growth rate is 32 days. The MRG mode contributes about 60% to the background eigenmode. The rest of the eigenmode energy is given by Rossby modes. Shades denote the fluid depth perturbation. The arrows stand for the horizontal wind perturbation. The purple line shows the zonally averaged zonal wind from the same date.

Figure C6 depicts the distribution of  $E_{MRG}$  in zonal wavenumber and time for the first two fastest growing modes along with the QBO phases. The most remarkable feature is that during the westerly QBO phase significantly more energy is related to the MRG mode. This means that when barotropic instability is excited during the westerly phase, there will be plentiful energy growth related to MRG waves in stark contrast with the easterly phase. The largest differences of  $E_{MRG}$  between the QBO phases occur at  $k = 11 - 12$  with approximately 13 and 7 times larger  $E_{MRG}$  during the WQBO. Note also that the magnitude of  $E_{MRG}$  jumps an order of magnitude beyond  $k = 6$ . This means that the MRG wave development by barotropic instability is expected to be negligible at large scales ( $k = 1 - 5$ ) due to the smallness of  $E_{MRG}$ . On the contrary, synoptic and subsynoptic scales ( $k = 6 - 12$ ) are sensitive to barotropic instability of the QBO flow.

Figure C7a illustrates the seasonal mean growth exponents of the most unstable background eigenmode with respect to zonal wavenumber. Since the second fastest growing modes behave similarly, they are not shown. The exponents follow a yearly cycle with maximum growth occurring during boreal summer (JJA), which concurs with the maximum intensity of the Southern Hemispheric (SH) polar night jet that is the fastest zonal circulation at the 30 hPa

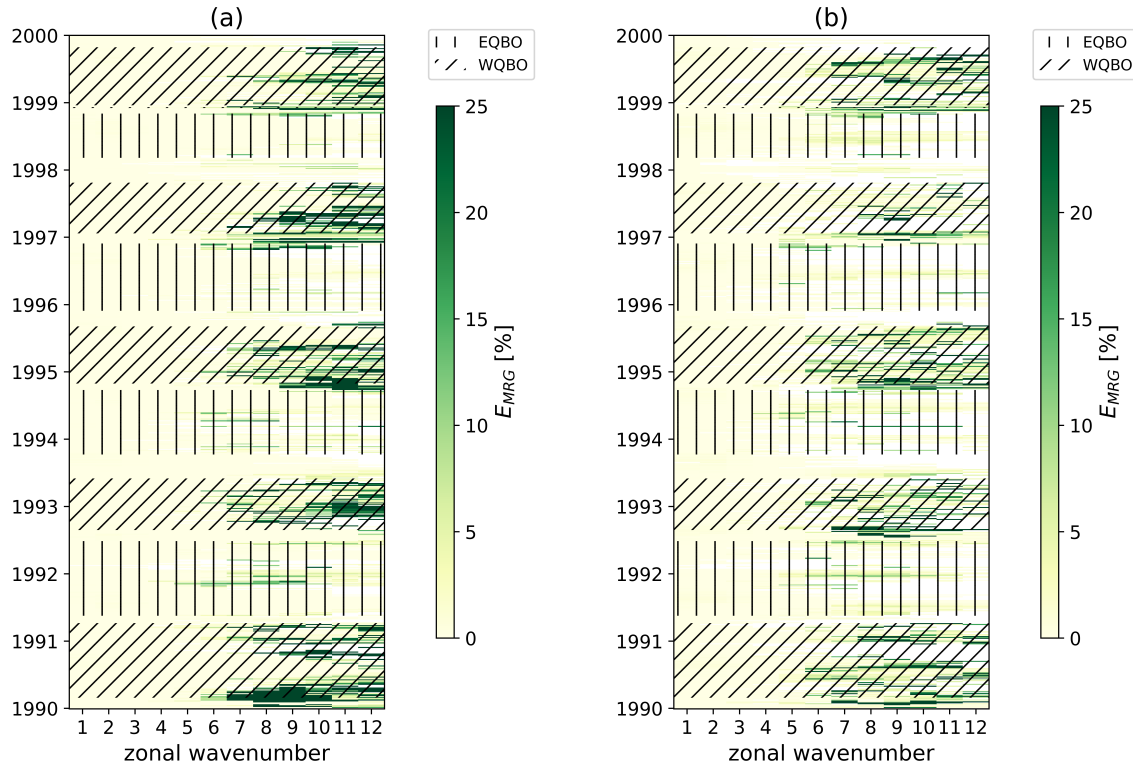


**Figure C6.** MRG wave energy ratio ( $E_{MRG}$ , expressed in %) of the (a) first and (b) second fastest growing modes with respect to zonal wavenumber and time. The data corresponding to the QBO easterly and westerly phases are illustrated by the hatches.

level. The growth rates are also large in the SON season, which is also due to the SH polar night jet that remains strong in early SON despite the mean flow transition from westerly towards weak easterly flow in the SH. In DJF, when the growth rates are small, the Northern Hemispheric westerly polar jet is only about a quarter of the magnitude of the SH polar jet. This indicates that the magnitude of the growth exponents are proportional to the absolute strength of the zonal circulation. The zonal wavenumber of the maximum growth also shifts in between the different season, which is likely influenced by the latitude of the zonal mean jets. Regarding the QBO phases, we find that on average the growth rates are somewhat larger during EQBO beyond  $k = 4$  (not shown). Note that during EQBO the zonal mean flow in the tropics is also stronger in absolute amplitude compared to the WQBO phase.

There is also a significant difference between the growth rates of eigenmodes with barotropic instability originating in the tropics and outside the tropics. Figure C7b shows that eigenmodes with large  $E_{MRG}$  (i.e. with strong barotropic instability conditions in the tropics) have growth exponents an order of magnitude smaller than eigenmodes with instability occurring primarily in the extratropics, i.e. low values of  $E_{MRG}$ . To distinguish between background

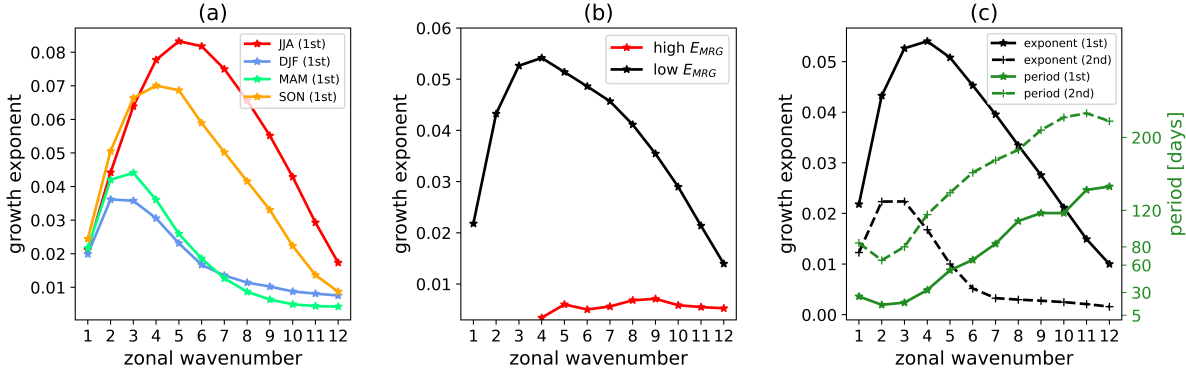


**Figure C7.** (a) Seasonal mean growth exponents of the fastest growing mode with respect to zonal wavenumber. (b) Mean growth exponents of unstable eigenmodes with high and low  $E_{MRG}$  (red and black respectively). The limit for high  $E_{MRG}$  is 2%. (c) 10-year mean growth exponents (black) and e-folding timescales of instability growth (green) of the fastest (solid) and second fastest (dashed) growing mode with respect to zonal wavenumber.

eigenmodes with low and high  $E_{MRG}$  we chose a value of 2%, which is 10 times larger than the climatological mean ratio of MRG and total wave energy at 30 hPa. Figure C7b also demonstrates that barotropic instability of the QBO flow excites essentially no MRG waves with  $k < 5$ , since  $E_{MRG}$  takes only about 0.05% at these scales.

The growth rates of the fastest growing modes are approximately double in magnitude compared to the second fastest growing modes at the peak zonal wavenumbers as illustrated by Fig. C7c. Overall, we find that planetary and large synoptic scales grow the fastest by barotropic instability at 30 hPa, which are related to extratropics, not the QBO flow. The e-folding timescale of the instability growth are on average 10 days for  $k = 2 - 3$ , and of seasonal timescales for  $k = 1$  and  $k = 6 - 7$ . For  $k = 8 - 12$  the timescales are even higher reaching inter-seasonal timescales, which means that instability growth would be barely detectable beyond  $k = 8$ , since the growth rates are too small for subsynoptic scales. The Doppler-shifted periods ( $\Re[\sigma]$ ) of the background eigenmodes are on average 1-4 days for  $k = 2 - 12$ , however, for  $k = 1$ , the average period is approximately 7 days (not shown). This tells us that the unstable modes primarily fall into the low-frequency Rossby mode category.

Figure C8 presents the percentage of the dates with a non-zero growth exponent for zonal wavenumbers 1-12. We find that the occurrence of positive  $\Im[\sigma]$  gradually decreases with  $k$ . It is also important to note that this occurrence is higher during the QBO phases compared to all analysed dates containing dates without a dominant QBO. The difference between the QBO phases is also significant with larger occurrence of non-zero growth rates during WQBO beyond  $k = 2$ , which is in agreement with our instability occurrence results derived by the RK and R83

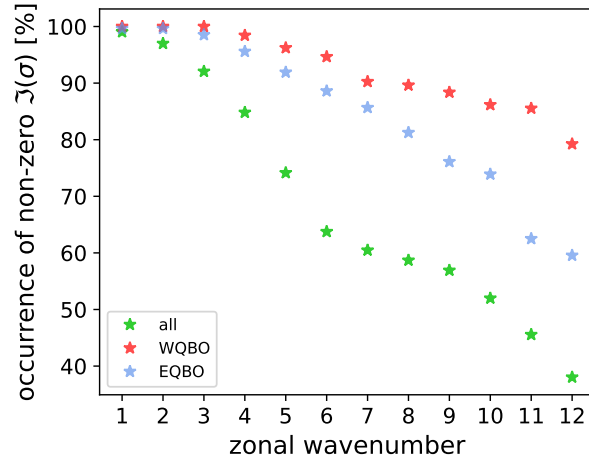


**Figure C8.** Percentage of dates with a non-zero growth exponent with respect to zonal wavenumber in case of all considered dates (green), the WQBO phase (red) and the EQBO phase (blue). The analysis period is 1990-1999 with 5-day timesteps.

stability criteria (see Section C18.2).

On the whole, our results show that zonal wavenumber of 6 acts as a limit beyond which MRG wave growth by the barotropic instability of the QBO is relevant. The instability growth is clearly favoured during the WQBO phase as the structure of the most unstable background eigenmodes suggests. However, beyond  $k = 8$  the growth rates become small. Therefore, we claim that the most energetic wavenumbers relevant for the barotropic instability of the QBO are found in range of  $6 \leq k \leq 8$ . We have also shown that the large scales show the fastest growth by barotropic instability, however, these unstable modes have very low  $E_{MRG}$ , meaning that barotropic instability is related to the extratropics for unstable modes of  $k < 6$ .

## C19 Discussion and summary

In this study we argued that the larger MRG wave kinetic energy at 30 hPa during the westerly QBO phase relative to the easterly phase at synoptic and subsynoptic scales can be explained by local MRG wave generation by barotropic instability of the QBO flow. First, we proved through idealised simulations that MRG waves grow intensively following barotropic instability development of equatorial zonal flows mimicking the circulation of the QBO. By studying the potential for barotropic instability of the 30 hPa equatorial zonal mean flow over 1990-1999, we showed that the condition for barotropic instability in the tropics is 2 times more frequently satisfied during the westerly QBO phase ( $\sim 80\%$  of the total number of cases) compared to the easterly QBO phase. The instability of the westerly QBO jet has also been

highlighted both in modelling and observational studies (Shuckburgh et al., 2001; Garcia and Richter, 2019), however, this is the first study providing a long-term analysis for the potential of barotropic instability of the QBO region.

We also computed unstable eigenmodes of the shallow water system linearized around the 30 hPa zonal mean zonal wind in years 1990-1999 for the zonal wavenumber range of 1-12 by the BGHough software following Kasahara (1980). When the QBO region is barotropically unstable, it was shown that zonal wavenumbers 6 – 12 are likely to grow. Such unstable eigenmodes contain large amounts of MRG wave energy often reaching more than 20% of the total energy of the mode, especially during the westerly QBO phase. Nevertheless, the fastest growing wavenumbers ( $k = 3 - 5$ ) can be connected to the extratropical circulation (i.e., the polar night jets), which are barotropically unstable throughout almost the whole analysis period and such modes do not contain significant amounts of MRG wave energy. Since barotropic instability of the extratropical stratosphere is not the main focus of this paper, additional analysis is left for a future study.

We have also demonstrated that the modes with instability originating from the equatorial region have much lower growth exponents, compared to those unstable modes that are related to instabilities outside the tropics. For example, the shortest e-folding timescale for instability growth for tropical unstable modes is 20 days, whereas it is 4.4 days for extratropical modes. This is in agreement with the findings of Paldor et al. (2021), who studied the growth rates of barotropically unstable equatorial and midlatitude jets. One reason for small growth exponents in the tropics potentially stems from the strength of the mean flow, since the magnitude of the growth exponents is proportional to the zonal mean zonal winds, which are weaker in the QBO region compared to the extratropics. The smallness of the growth rates related to the QBO flow and the unstable modes challenges the diagnosis of MRG wave growth by instability from real data. As Fig. C9 demonstrates, some of the most unstable eigenmodes beyond  $k = 4$  have multiple local maxima in their horizontal structure, which means that both the tropical and the extratropical mean flows are barotropically unstable simultaneously. This indicates that when unstable modes are excited, not only MRG waves will grow but also extratropical Rossby waves. On the contrary, for large scales ( $k = 1 - 4$ ), barotropic instability is almost exclusive to the extratropics, meaning no large-scale MRG wave growth by instability.

We note that the choice of the equivalent depth influences the growth exponents and the zonal wavenumbers of the fastest growing modes, especially when one considers a mean depth at the order of 100 m or lower, which is in agreement with Winter and Schmitz (1998), and Paldor et al. (2021) who found convergence of the growth exponents derived from the linearized shallow water equations, the non-divergent barotropic vorticity equation and the

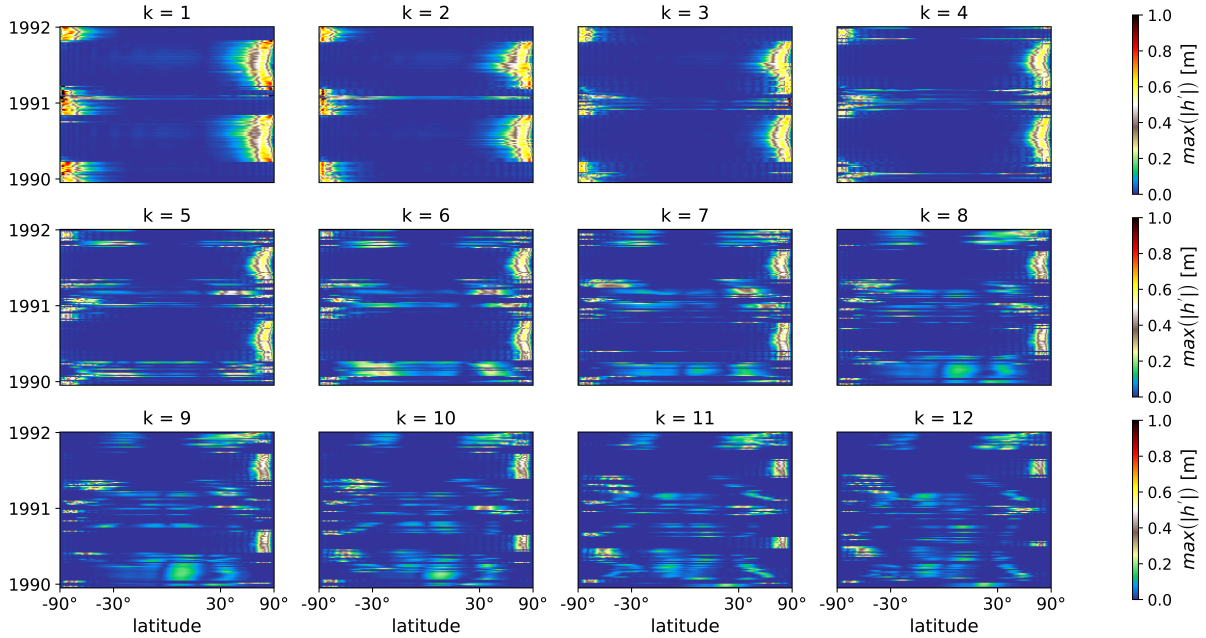


**Figure C9.** Absolute maximum of the unstable eigenmodes' height perturbation with respect to latitude and time in different zonal wavenumbers ( $k$ ). When there was no unstable eigenmode available at a certain date and zonal wavenumber, a value of 0 is assigned. The locations of the maxima represent the latitudes where the zonal mean flow is barotropically unstable. The QBO region can generate disturbances with  $k > 4$  through barotropic instability.

quasi-geostrophic vorticity equation towards large mean depths. We chose the barotropic mode (i.e. the mean depth of  $D = 10$  km) for our analysis since the observed MRG wave frequencies and meridional scales at 30 hPa are close to the theoretical MRG waves of  $D = 10$  km. Using the barotropic mode also eliminates negative fluid heights when computing the eigenmodes of the linearized system. Nevertheless, we note that this research would benefit from extending the background eigenmode analysis by including multiple vertical modes in the computations, since the QBO is distributed between several vertical modes, and the growth rates are sensitive to the choice of the mean depth.

Winter and Schmitz (1998) demonstrated that inertially unstable flows can excite divergent waves in the tropics as well as MRG wave-like structures. As inertial and barotropic instability may co-exist (Winter and Schmitz, 1998; ?), we tested the 30 hPa zonal mean flow for inertial instability,  $f(f - \bar{u}_\phi) < 0$ , and found weak instability in about 80% of the cases within the tropical ( $\pm 30^\circ$ ) region in 1990-1999. Since no major difference was found in the satisfaction of inertial instability between the QBO phases, we conclude that barotropic instability is more likely to influence MRG wave growth than inertial instability at 30 hPa.

We found that the growth exponents for the easterly QBO phase are significantly higher,

which contradicts the claim that MRG wave growth is enhanced during the westerly phase. However, by studying the MRG wave kinetic energy spectra averaged for dates with high and low growth exponents, we notice that the kinetic energy is significantly lower for dates with high growth rates. This means that the energetics of the background eigenmodes are more important for the MRG wave growth than the growth rates. Since the unstable modes contain significantly larger MRG wave energy and instability is more frequent during the westerly QBO phase, MRG waves are expected to grow more intensely compared to the easterly phase.

Garcia and Richter (2019) hints on the potential importance of the horizontal resolution of the flow field to simulate well MRG waves in the stratosphere. Indeed, coarse resolution can erase fine structures of the zonal mean flow, which may affect barotropic instability and the associated unstable modes. Interestingly, we did not find significant discrepancies between the growth rates, the fastest growing wavenumbers and the MRG wave energy ratios of the unstable eigenmodes when we performed the computation with BGHough prescribed with zonal mean flows with 64, 128, and 256 latitudinal grid points.

We computed the kinetic energy related to the most unstable background eigenmode per date and per zonal wavenumber by using the ERA5 total wave field of the zonal and meridional wind of 30 hPa in 1990-1999. By assuming that these modes grow exponentially controlled by their growth exponents (i.e.,  $\Im[\sigma]$ ), we calculated their exponential growth in time weighted by  $E_{MRG}$  and compared with the timeseries of MRG wave kinetic energy. Overall, we found little correlation between MRG wave kinetic energy change and the predicted MRG wave growth by the unstable eigenmodes. This is due to that only a small portion of the observed wave energy projects onto the most unstable mode and the growth rates become small at subsynoptic scales ( $k > 8$ ). It is also likely that not the fastest growing mode, but a combination of unstable modes grow in nature, which then cause MRG wave energy to rise. Since the background eigenmodes are not orthogonal (Holube et al., 2024), it is challenging to establish a predictive model for the MRG wave growth with the inclusion of multiple unstable modes.

To conclude, we demonstrated through idealised simulations that MRG wave growth rapidly intensifies due to barotropic instability development of equatorial jets. The westerly QBO phase was also found to be much more sensitive to instability growth than the easterly phase. In particular, we have shown that synoptic and subsynoptic scale MRG waves are likely to grow by barotropic instability development of the QBO jet. However, our results also indicate that the most effective growth is limited to the zonal wavenumber range of 6 – 8. Overall, the MRG wave barotropic instability growth could explain the kinetic energy difference between the westerly and easterly QBO phase at synoptic and subsynoptic scales, which promotes the supposition that MRG waves can be generated locally in the stratosphere.

## C20 Supplement

### Computation of mixed Rossby-gravity wave kinetic energy at 30 hPa

The MRG wave kinetic energy is obtained by 3-dimensional normal mode decomposition by using the MODES software (Žagar et al., 2015). The dataset used here is similar as in Žagar et al. (2022), who analysed the 3-dimensional structure of Kelvin waves over a climatological period. MODES diagnoses various Hough harmonics from meteorological data, which are the eigensolutions of the linearized primitive equations on the sphere. The Hough harmonics are composed of low-frequency Rossby and high frequency IG waves as well as the Kelvin and the MRG wave of different zonal wavenumbers ( $k$ ) and vertical mode index ( $m$ ). As input we supplied ERA5 data comprising of temperature, zonal wind, meridional wind, surface geopotential and mean sea level pressure for MODES, which computed the MRG wave wind ( $u, v$ ) and geopotential height ( $h$ ) perturbations as global 3D fields reading as

$$(u, v, h)^T(\lambda, \varphi, \zeta) = \sum_{m=1}^M \sum_{k=-K}^K G_m(\zeta) \mathbf{S}_m \left( u_m^k, v_m^k, h_m^k \right)^T(\lambda, \varphi). \quad (\text{C20.11})$$

In Eq. (C20.11)  $\varphi$ ,  $\lambda$  and  $\zeta$  are the latitude, longitude and the vertical sigma level respectively. Furthermore,  $G_m(\zeta)$  are the vertical structure functions (VSFs) of  $m = 1, \dots, M$ ,  $\mathbf{S}_m$  is a scaling diagonal matrix with elements  $(\sqrt{gD_m}, \sqrt{gD_m}, D_m)$  and  $(u_m^k, v_m^k, h_m^k)^T$  are the MRG wave zonal wind, meridional wind and geopotential height components of distinct  $m$  and  $k$ , which are expanded in terms of Hough harmonics as

$$\left( u_m^k, v_m^k, h_m^k \right)^T(\lambda, \varphi) = \chi_m^k \Theta_m^k(\varphi) e^{ik\lambda}, \quad (\text{C20.12})$$

where  $\chi_m^k$  is the Hough coefficient of the MRG mode and  $\Theta_m^k(\varphi)$  is the meridional MRG Hough function.

Daily data from 43 sigma levels extending up to 0.4 hPa from 12 UTC in years 1990-1999 are analysed on a T85 Gaussian grid. For the Hough harmonics computation we used the zonal truncation limit of 100 for 27 vertical structure functions (VSF). The corresponding mean depths range from 10060 to 8 m. We use the global MRG wave  $u$  and  $v$ -wind fields at 30 hPa for the computation of the MRG wave kinetic energy for different  $k$  by applying spherical harmonics decomposition. For more details of the normal mode decomposition and the wave filtering in sigma system the reader is advised to view Žagar et al. (2022) and Žagar et al. (2015).

## **C21 Acknowledgements**

This paper is a contribution to the project W6 (Spectral Energy Fluxes by Wave-Wave interactions) of the Collaborative Research Centre TRR 181 "Energy Transfers in Atmosphere and Ocean" funded by the Deutsche Forschungsgemeinschaft (DFG, German Research Foundation) - Projektnummer 274762653.

## References

- Aiyyer, A. R. and Molinari, J. (2003). Evolution of mixed Rossby–gravity waves in idealized MJO environments. *Journal of the Atmospheric Sciences*, 60(23):2837–2855. [https://doi.org/10.1175/1520-0469\(2003\)060;2837:EOMRWI;2.0.CO;2](https://doi.org/10.1175/1520-0469(2003)060;2837:EOMRWI;2.0.CO;2).
- Alexander, M. and Ortland, D. (2010). Equatorial waves in high resolution dynamics limb sounder (HIRDLS) data. *Journal of Geophysical Research: Atmospheres*, 115(D24). <https://doi.org/10.1029/2010JD014782>.
- Alexander, S., Tsuda, T., Kawatani, Y., and Takahashi, M. (2008). Global distribution of atmospheric waves in the equatorial upper troposphere and lower stratosphere: COSMIC observations of wave mean flow interactions. *Journal of Geophysical Research: Atmospheres*, 113:D24. <https://doi.org/10.1029/2008JD010039>.
- Andrews, D. and McIntyre, M. E. (1976). Planetary waves in horizontal and vertical shear: The generalized Eliassen-Palm relation and the mean zonal acceleration. *Journal of the Atmospheric Sciences*, 33(11):2031–2048. [https://doi.org/10.1175/1520-0469\(1976\)033;2031:PWIHAV;2.0.CO;2](https://doi.org/10.1175/1520-0469(1976)033;2031:PWIHAV;2.0.CO;2).
- Baldwin, M. P., Gray, L., Dunkerton, T., Hamilton, K., Haynes, P., Randel, W., Holton, J., Alexander, M., Hirota, I., Horinouchi, T., et al. (2001). The quasi-biennial oscillation. *Reviews of Geophysics*, 39(2):179–229. <https://doi.org/10.1029/1999RG000073>.
- Barpanda, P., Tulich, S. N., Dias, J., and Kiladis, G. N. (2023). The role of subtropical Rossby waves in amplifying the divergent circulation of the Madden–Julian Oscillation. *Journal of the Atmospheric Sciences*, 80(10):2377–2398. <https://doi.org/10.1175/JAS-D-22-0259.1>.
- Bechtold, P., Köhler, M., Jung, T., Doblas-Reyes, F., Leutbecher, M., Rodwell, M. J., Vitart, F., and Balsamo, G. (2008). Advances in simulating atmospheric variability with the ECMWF model: From synoptic to decadal time-scales. *Quarterly Journal of the Royal Meteorological Society*, 134(634):1337–1351. <https://doi.org/10.1002/qj.289>.
- Bergman, J. W. and Salby, M. L. (1994). Equatorial wave activity derived from fluctuations in observed convection. *Journal of the Atmospheric Sciences*, 51:3791–3806. [https://doi.org/10.1175/1520-0469\(1994\)051;3791:EWADFF;2.0.CO;2](https://doi.org/10.1175/1520-0469(1994)051;3791:EWADFF;2.0.CO;2).
- Boyd, J. P. (2018). Kelvin, Yanai, Rossby and gravity Waves. *Dynamics of the Equatorial Ocean*, pages 35–67.
- Boyd, J. P. and Zhou, C. (2008). Kelvin waves in the nonlinear shallow water equations on the sphere: nonlinear travelling waves and the corner wave bifurcation. *Journal of Fluid Mechanics*, 617:187–205. <https://doi.org/10.1017/S0022112008003959>.

- Bühler, O. and McIntyre, M. E. (1999). On shear-generated gravity waves that reach the mesosphere. Part II: Wave propagation. *Journal of the Atmospheric Sciences*, 56(21):3764–3773. [https://doi.org/10.1175/1520-0469\(1999\)056<3764:OSGGWT>2.0.CO;2](https://doi.org/10.1175/1520-0469(1999)056<3764:OSGGWT>2.0.CO;2).
- Butchart, N. (2022). The stratosphere: A review of the dynamics and variability. *Weather and Climate Dynamics*, 3(4):1237–1272. <https://doi.org/10.5194/wcd-3-1237-2022>.
- C3S (2017). ERA5: Fifth generation of ECMWF atmospheric reanalyses of the global climate [Dataset]. <https://doi.org/10.24381/cds.143582cf>.
- Chang, C.-P. (1970). Westward propagating cloud patterns in the tropical Pacific as seen from time-composite satellite photographs. *Journal of the Atmospheric Sciences*, 27:133–138. [https://doi.org/10.1175/1520-0469\(1970\)027<0133:WPCPIT>2.0.CO;2](https://doi.org/10.1175/1520-0469(1970)027<0133:WPCPIT>2.0.CO;2).
- Chrisler, B. and Stachnik, J. P. (2023). Tropical-wave activity and Madden–Julian oscillation termination. *Quarterly Journal of the Royal Meteorological Society*, 149(750):61–83. <https://doi.org/10.1002/qj.4393>.
- Dias, J. and Kiladis, G. N. (2016). The relationship between equatorial mixed Rossby–gravity and eastward inertio-gravity waves. Part II. *Journal of the Atmospheric Sciences*, 73(5):2147–2163. <https://doi.org/10.1175/JAS-D-15-0231.1>.
- Dias, J., Silva Dias, P. L., Kiladis, G. N., and Gehne, M. (2013). Modulation of shallow-water equatorial waves due to a varying equivalent height background. *Journal of the Atmospheric Sciences*, 70(9):2726–2750. <https://doi.org/10.1175/JAS-D-13-04.1>.
- Dickinson, M. and Molinari, J. (2002). Mixed Rossby–gravity waves and western Pacific tropical cyclogenesis. Part I: Synoptic evolution. *Journal of the Atmospheric Sciences*, 59:2183–2196. [https://doi.org/10.1175/1520-0469\(2002\)059<2183:MRGWAW>2.0.CO;2](https://doi.org/10.1175/1520-0469(2002)059<2183:MRGWAW>2.0.CO;2).
- ECMWF (2020). *Documentation – Cy48r1, Operational implementation 27 June 2023, Part III: Dynamics and numerical procedures*. ECMWF.
- Ern, M., Ploeger, F., Preusse, P., Gille, J., Gray, L., Kalisch, S., Mlynczak, M., Russell III, J., and Riese, M. (2014). Interaction of gravity waves with the QBO: A satellite perspective. *Journal of Geophysical Research: Atmospheres*, 119(5):2329–2355. <https://doi.org/10.1002/2013JD020731>.
- Ern, M., Preusse, P., Krebsbach, M., Mlynczak, M., and Russell Iii, J. (2008). Equatorial wave analysis from SABER and ECMWF temperatures. *Atmospheric Chemistry and Physics*, 8(4):845–869. <https://doi.org/10.5194/acp-8-845-2008>.
- Feng, X., Yang, G.-Y., Hodges, K. I., and Methven, J. (2023). Equatorial waves as useful precursors to tropical cyclone occurrence and intensification. *Nature Communications*, 14(1):511.

<https://doi.org/10.1038/s41467-023-36055-5>.

- Garcia, R. R. and Richter, J. H. (2019). On the momentum budget of the quasi-biennial oscillation in the Whole Atmosphere Community Climate Model. *Journal of the Atmospheric Sciences*, 76(1):69–87. <https://doi.org/10.1175/JAS-D-18-0088.1>.
- Garcia, R. R. and Salby, M. L. (1987). Transient response to localized episodic heating in the tropics. Part II: Far-field behavior. *Journal of the Atmospheric Sciences*, 44(2):499–532. [https://doi.org/10.1175/1520-0469\(1987\)044<0499:TRTLEH>2.0.CO;2](https://doi.org/10.1175/1520-0469(1987)044<0499:TRTLEH>2.0.CO;2).
- Gehne, M. and Kleeman, R. (2012). Spectral analysis of tropical atmospheric dynamical variables using a linear shallow-water modal decomposition. *Journal of the Atmospheric Sciences*, 69(7):2300–2316. <https://doi.org/10.1175/JAS-D-10-05008.1>.
- Gelb, A. and Gleeson, J. P. (2001). Spectral viscosity for shallow water equations in spherical geometry. *Monthly Weather Review*, 129:2346–2360. [https://doi.org/10.1175/1520-0493\(2001\)129<2346:SVFSWE>2.0.CO;2](https://doi.org/10.1175/1520-0493(2001)129<2346:SVFSWE>2.0.CO;2).
- Gill, A. E. (1980). Some simple solutions for heat-induced tropical circulation. *Quarterly Journal of the Royal Meteorological Society*, 106(449):447–462. <https://doi.org/10.1002/qj.49710644905>.
- Grimm, A. M. and Dias, P. L. S. (1995). Analysis of tropical-extratropical interactions with influence functions of a barotropic model. *Journal of the Atmospheric Sciences*, 52(20). [https://doi.org/10.1175/1520-0469\(1995\)052<3538:AOTIWI>2.0.CO;2](https://doi.org/10.1175/1520-0469(1995)052<3538:AOTIWI>2.0.CO;2).
- Hamilton, K. (1984). Mean wind evolution through the quasi-biennial cycle in the tropical lower stratosphere. *Journal of the Atmospheric Sciences*, 41(13):2113–2125. [https://doi.org/10.1175/1520-0469\(1976\)033<2031:PWIHAV>2.0.CO;2](https://doi.org/10.1175/1520-0469(1976)033<2031:PWIHAV>2.0.CO;2).
- Hartney, N. and Bendall, T. (2024). A unifying moist shallow water framework and test cases for moist shallow water models. Technical report, Copernicus Meetings. <https://doi.org/10.5194/egusphere-egu24-12501>.
- Hayashi, Y. (1970). A theory of large-scale equatorial waves generated by condensation heat and accelerating. *Journal of the Meteorological Society of Japan. Ser. II*, 48:140–160. [10.2151/jmsj1965.48.2\\_140](https://doi.org/10.2151/jmsj1965.48.2_140).
- Hayashi, Y. (1971). A generalized method of resolving disturbances into progressive and retrogressive waves by space Fourier and time cross-spectral analyses. *Journal of the Meteorological Society of Japan. Ser. II*, 49(2):125–128. [https://doi.org/10.2151/jmsj1965.49.2\\_125](https://doi.org/10.2151/jmsj1965.49.2_125).
- Hayashi, Y. (1994). Kelvin and mixed Rossby-gravity waves appearing in the GFDL” SKYHI” general circulation model and the FGGE dataset: Implications for their generation mechanism

- and role in the QBO. *Journal of the Meteorological Society of Japan. Ser. II*, 72(6):901–935. [https://doi.org/10.2151/jmsj1965.72.6\\_901](https://doi.org/10.2151/jmsj1965.72.6_901).
- Hendon, H. H. and Liebmann, B. (1991). The structure and annual variation of antisymmetric fluctuations of tropical convection and their association with Rossby–gravity waves. *Journal of the Atmospheric Sciences*, 48(19):2127–2140. [https://doi.org/10.1175/1520-0469\(1991\)048;2127:TSAAVO;2.0.CO;2](https://doi.org/10.1175/1520-0469(1991)048;2127:TSAAVO;2.0.CO;2).
- Hersbach, H., Bell, B., Berrisford, P., Hirahara, S., Horányi, A., Muñoz-Sabater, J., Nicolas, J., Peubey, C., Radu, R., Schepers, D., et al. (2020). The ERA5 global reanalysis. *Quarterly Journal of the Royal Meteorological Society*, 146:1999–2049. <https://doi.org/10.1002/qj.3803>.
- Hess, P. G., Hendon, H. H., and Battisti, D. S. (1993). The relationship between mixed Rossby-gravity waves and convection in a general circulation model. *Journal of the Meteorological Society of Japan. Ser. II*, 71:321–338. [https://doi.org/10.2151/jmsj1965.71.3\\_321](https://doi.org/10.2151/jmsj1965.71.3_321).
- Hirooka, T. and Hirota, I. (1985). Normal mode Rossby waves observed in the upper stratosphere. Part II: Second antisymmetric and symmetric modes of zonal wavenumbers 1 and 2. *Journal of Atmospheric Sciences*, 42(6):536–548. [https://doi.org/10.1175/1520-0469\(1984\)041;1253:NMRWOI;2.0.CO;2](https://doi.org/10.1175/1520-0469(1984)041;1253:NMRWOI;2.0.CO;2).
- Holt, L. A., Alexander, M. J., Coy, L., Molod, A., Putman, W., and Pawson, S. (2016). Tropical waves and the quasi-biennial oscillation in a 7-km global climate simulation. *Journal of the Atmospheric Sciences*, 73(9):3771–3783. <https://doi.org/10.1175/JAS-D-15-0350.1>.
- Holt, L. A., Lott, F., Garcia, R. R., Kiladis, G. N., Cheng, Y.-M., Anstey, J. A., Braesicke, P., Bushell, A. C., Butchart, N., Cagnazzo, C., et al. (2022). An evaluation of tropical waves and wave forcing of the QBO in the QBOi models. *Quarterly Journal of the Royal Meteorological Society*, 148(744):1541–1567. <https://doi.org/10.1002/qj.3827>.
- Holton, J. R. (1972). Waves in the equatorial stratosphere generated by tropospheric heat sources. *Journal of the Atmospheric Sciences*, 29:368–375. [10.1175/1520-0469\(1972\)029;0368:WITESG;2.0.CO;2](https://doi.org/10.1175/1520-0469(1972)029;0368:WITESG;2.0.CO;2).
- Holton, J. R. (2004). Tropical Dynamics. In *An introduction to dynamic meteorology*, pages 371–407. Elsevier Academic Press, fourth edition.
- Holton, J. R. and Lindzen, R. S. (1972). An updated theory for the quasi-biennial cycle of the tropical stratosphere. *Journal of the Atmospheric Sciences*, 29(6):1076–1080. [https://doi.org/10.1175/1520-0469\(1972\)029;1076:AUTFTQ;2.0.CO;2](https://doi.org/10.1175/1520-0469(1972)029;1076:AUTFTQ;2.0.CO;2).
- Holube, K. M., Lunkeit, F., Vasylykevych, S., and Žagar, N. (2024). Resonant excitation of Kelvin waves by interactions of subtropical Rossby waves and the zonal mean flow. *Journal of the Atmospheric Sciences*. <https://doi.org/10.1175/JAS-D-24-0033.1>.

- Hoskins, B. and Yang, G.-Y. (2021). The detailed dynamics of the Hadley cell. Part II: December–February. *Journal of Climate*, 34(2):805–823. <https://doi.org/10.1175/JCLI-D-20-0504.1>.
- Hoskins, B. J. and Simmons, A. J. (1975). A multi-layer spectral model and the semi-implicit method. *Quarterly Journal of the Royal Meteorological Society*, 101(429):637–655. <https://doi.org/10.1002/qj.49710142918>.
- Hua, B. L., d’Orgeville, M., Fruman, M. D., Menesguen, C., Schopp, R., Klein, P., and Sasaki, H. (2008). Destabilization of mixed Rossby gravity waves and the formation of equatorial zonal jets. *Journal of Fluid Mechanics*, 610:311–341. <https://doi.org/10.1017/S0022112008002656>.
- Hung, M.-P., Lin, J.-L., Wang, W., Kim, D., Shinoda, T., and Weaver, S. J. (2013). MJO and convectively coupled equatorial waves simulated by CMIP5 climate models. *Journal of Climate*, 26(17):6185–6214. <https://doi.org/10.1175/JCLI-D-12-00541.1>.
- Hunter, J. D. (2007). Matplotlib: A 2D graphics environment. *Computing in science & engineering*, 9(03):90–95.
- Itoh, H. and Ghil, M. (1988). The generation mechanism of mixed Rossby-gravity waves in the equatorial troposphere. *Journal of the Atmospheric Sciences*, 45:585–604. [10.1175/1520-0469\(1988\)045;0585:TGMOMR;2.0.CO;2](https://doi.org/10.1175/1520-0469(1988)045<0585:TGMOMR>2.0.CO;2).
- Jin, F. and Hoskins, B. J. (1995). The direct response to tropical heating in a baroclinic atmosphere. *Journal of the Atmospheric Sciences*, 52(3). [https://doi.org/10.1175/1520-0469\(1988\)045;1228:TGOGRF;2.0.CO;2](https://doi.org/10.1175/1520-0469(1988)045<1228:TGOGRF>2.0.CO;2).
- Jung, H. and Knippertz, P. (2023). Link between the time-space behavior of rainfall and 3d dynamical structures of equatorial waves in global convection-permitting simulations. *Geophysical Research Letters*, 50(2):e2022GL100973. <https://doi.org/10.1029/2022GL100973>.
- Kasahara, A. (1977). Numerical integration of the global barotropic primitive equations with Hough harmonic expansions. *Journal of the Atmospheric Sciences*, 34:687–701. [https://doi.org/10.1175/1520-0469\(1977\)034;0687:NIOTGB;2.0.CO;2](https://doi.org/10.1175/1520-0469(1977)034<0687:NIOTGB>2.0.CO;2).
- Kasahara, A. (1978). Further studies on a spectral model of the global barotropic primitive equations with Hough harmonic expansions. *Journal of the Atmospheric Sciences*, 35:2043–2051. [https://doi.org/10.1175/1520-0469\(1978\)035;2043:FSOASM;2.0.CO;2](https://doi.org/10.1175/1520-0469(1978)035<2043:FSOASM>2.0.CO;2).
- Kasahara, A. (1980). Effect of zonal flows on the free oscillations of a barotropic atmosphere. *Journal of the Atmospheric Sciences*, 37. [https://doi.org/10.1175/1520-0469\(1980\)037;0917:EOZFOT;2.0.CO;2](https://doi.org/10.1175/1520-0469(1980)037<0917:EOZFOT>2.0.CO;2).
- Kasahara, A. (1984). The linear response of a stratified global atmosphere to a tropical thermal forcing. *Journal of the Atmospheric Sciences*, 41(14):2217–2237. [https://doi.org/10.1175/1520-0469\(1984\)041;2217:LRSGA;2.0.CO;2](https://doi.org/10.1175/1520-0469(1984)041<2217:LRSGA>2.0.CO;2).

0469(1984)041;2217:TLROAS;2.0.CO;2.

Kasahara, A. and da Silva Dias, P. L. (1986). Response of planetary waves to stationary tropical heating in a global atmosphere with meridional and vertical shear. *Journal of the Atmospheric Sciences*, 43:1893–1912. [10.1175/1520-0469\(1986\)043;1893:ROPWTS;2.0.CO;2](https://doi.org/10.1175/1520-0469(1986)043;1893:ROPWTS;2.0.CO;2).

Kasahara, A. and Puri, K. (1981). Spectral representation of three-dimensional global data by expansion in normal mode functions. *Monthly Weather Review*, 109(1):37–51. [https://doi.org/10.1175/1520-0493\(1981\)109;0037:SROTDG;2.0.CO;2](https://doi.org/10.1175/1520-0493(1981)109;0037:SROTDG;2.0.CO;2).

Kawatani, Y., Watanabe, S., Sato, K., Dunkerton, T. J., Miyahara, S., and Takahashi, M. (2010). The roles of equatorial trapped waves and internal inertia–gravity waves in driving the quasi-biennial oscillation. Part I: Zonal mean wave forcing. *Journal of the Atmospheric Sciences*, 67(4):963–980. <https://doi.org/10.1175/2009JAS3222.1>.

Knippertz, P., Gehne, M., Kiladis, G. N., Kikuchi, K., Rasheeda Satheesh, A., Roundy, P. E., Yang, G.-Y., Žagar, N., Dias, J., Fink, A. H., et al. (2022). The intricacies of identifying equatorial waves. *Quarterly Journal of the Royal Meteorological Society*, 148(747):2814–2852. <https://doi.org/10.1002/qj.4338>.

Kuo, H.-I. (1949). Dynamic instability of two-dimensional nondivergent flow in a barotropic atmosphere. *Journal of the Atmospheric Sciences*, 6:105–122. [https://doi.org/10.1175/1520-0469\(1949\)006;0105:DIOTDN;2.0.CO;2](https://doi.org/10.1175/1520-0469(1949)006;0105:DIOTDN;2.0.CO;2).

Lee, H.-K., Chun, H.-Y., Richter, J. H., Simpson, I. R., and Garcia, R. R. (2024). Contributions of parameterized gravity waves and resolved equatorial waves to the QBO period in a future climate of CESM2. *Journal of Geophysical Research: Atmospheres*, 129(8):e2024JD040744. <https://doi.org/10.1029/2024JD040744>.

Lindzen, R. S. and Holton, J. R. (1968). A theory of the quasi-biennial oscillation. *Journal of the Atmospheric Sciences*, 25:1095–1107. [https://doi.org/10.1175/1520-0469\(1968\)025;1095:ATOTQB;2.0.CO;2](https://doi.org/10.1175/1520-0469(1968)025;1095:ATOTQB;2.0.CO;2).

Longuet-Higgins, M. S. (1968). The eigenfunctions of Laplace’s tidal equation over a sphere. *Philosophical Transactions of the Royal Society of London. Series A, Mathematical and Physical Sciences*, 262:511–607. <https://doi.org/10.1098/rsta.1968.0003>.

Magaña, V. and Yanai, M. (1995). Mixed Rossby–gravity waves triggered by lateral forcing. *Journal of the Atmospheric Sciences*, 52(9):1473–1486. [https://doi.org/10.1175/1520-0469\(1995\)052;1473:MRWTBL;2.0.CO;2](https://doi.org/10.1175/1520-0469(1995)052;1473:MRWTBL;2.0.CO;2).

Maher, P., Gerber, E. P., Medeiros, B., Merlis, T. M., Sherwood, S., Sheshadri, A., Sobel, A. H., Vallis, G. K., Voigt, A., and Zurita-Gotor, P. (2019). Model hierarchies for understanding atmospheric circulation. *Reviews of Geophysics*, 57(2):250–280.

<https://doi.org/10.1029/2018RG000607>.

Mahó, S. I., Lunkeit, F., Vasylkevych, S., and Žagar, N. (2024a). Studying the scale selection of mixed Rossby-gravity waves: Idealized simulations with the TIGAR model [Dataset]. <https://doi.org/10.5281/zenodo.11451701>.

Mahó, S. I., Lunkeit, F., Vasylkevych, S., and Žagar, N. (2024b). The mechanism of scale selection for mixed Rossby-gravity waves in the upper troposphere and the upper stratosphere. under revision in *Geophysical Research Letters*.

Mahó, S. I., Vasylkevych, S., and Žagar, N. (2024c). Excitation of mixed Rossby-gravity waves by wave-mean flow interactions on the sphere. *Quarterly Journal of the Royal Meteorological Society*. <https://doi.org/10.1002/qj.4742>.

Mak, M.-K. (1969). Laterally driven stochastic motions in the tropics. *Journal of the Atmospheric Sciences*, 26:41–64. [10.1175/1520-0469\(1969\)026;0041:LDSMIT;2.0.CO;2](https://doi.org/10.1175/1520-0469(1969)026<0041:LDSMIT;2.0.CO;2).

Matsuno, T. (1966). Quasi-geostrophic motions in the equatorial area. *Journal of the Meteorological Society of Japan. Ser. II*, 44:25–43. [https://doi.org/10.2151/jmsj1965.44.1\\_25](https://doi.org/10.2151/jmsj1965.44.1_25).

McFarlane, S. A., Mather, J. H., and Ackerman, T. P. (2007). Analysis of tropical radiative heating profiles: A comparison of models and observations. *Journal of Geophysical Research: Atmospheres*, 112. <https://doi.org/10.1029/2006JD008290>.

Neduhal, V., Žagar, N., Lunkeit, F., Polichtchouk, I., and Zaplotnik, Ž. (2024). Decomposition of the horizontal wind divergence associated with the Rossby, mixed Rossby-gravity, inertia-gravity, and Kelvin waves on the sphere. *Journal of Geophysical Research: Atmospheres*, 129(9):e2023JD040427. <https://doi.org/10.1029/2023JD040427>.

Paldor, N., Fouxon, I., Shamir, O., and Garfinkel, C. I. (2018). The mixed Rossby–gravity wave on the spherical Earth. *Quarterly Journal of the Royal Meteorological Society*, 144:1820–1830. <https://doi.org/10.1002/qj.3354>.

Paldor, N., Shamir, O., and Garfinkel, C. I. (2021). Barotropic instability of a zonal jet on the sphere: From non-divergence through quasi-geostrophy to shallow water. *Geophysical & Astrophysical Fluid Dynamics*, 115(1):15–34. <https://doi.org/10.1080/03091929.2020.1724996>.

Pikovnik, M., Zaplotnik, Ž., Boljka, L., and Žagar, N. (2022). Metrics of the Hadley circulation strength and associated circulation trends. *Weather and Climate Dynamics*, 3(2):625–644. <https://doi.org/10.5194/wcd-3-625-2022>.

Plumb, R., McEwan, A., et al. (1978). The instability of a forced standing wave in a viscous stratified fluid- A laboratory analogue of the quasi-biennial oscillation. *Journal of the Atmospheric Sciences*, 35(10):1827–1839. <https://doi.org/10.1175/1520->

0469(1978)035;1827:TIOAFS;2.0.CO;2.

Randel, W. J., Boville, B. A., and Gille, J. C. (1990). Observations of Planetary Mixed Rossby–Gravity Waves in the Upper Stratosphere. *Journal of the Atmospheric Sciences*, 47(24):3092–3099. [https://doi.org/10.1175/1520-0469\(1990\)047;3092:OOPMRW;2.0.CO;2](https://doi.org/10.1175/1520-0469(1990)047;3092:OOPMRW;2.0.CO;2).

Raupp, C. and Dias, P. S. (2009). Resonant Wave Interactions in the Presence of a Diurnally Varying Heat Source. *Journal of the Atmospheric Sciences*, 66(10):3165–3183. <https://doi.org/10.1175/2009JAS2899.1>.

Raupp, C. F. and Silva Dias, P. L. (2005). Excitation mechanism of mixed Rossby–gravity waves in the equatorial atmosphere: Role of the nonlinear interactions among equatorial waves. *Journal of the Atmospheric Sciences*, 62:1446–1462.

Ricciardulli, L. and Garcia, R. R. (2000). The excitation of equatorial waves by deep convection in the NCAR Community Climate Model (CCM3). *Journal of the Atmospheric Sciences*, 57(21):3461–3487. [https://doi.org/10.1175/1520-0469\(2000\)057;3461:TEOEWB;2.0.CO;2](https://doi.org/10.1175/1520-0469(2000)057;3461:TEOEWB;2.0.CO;2).

Ripa, P. (1983). General stability conditions for zonal flows in a one-layer model on the  $\beta$ -plane or the sphere. *Journal of Fluid Mechanics*, 126:463–489. <https://doi.org/10.1017/S0022112083000270>.

Ritchie, H. (1988). Application of the semi-Lagrangian method to a spectral model of the shallow water equations. *Monthly Weather Review*, 116:1587–1598. [https://doi.org/10.1175/1520-0493\(1988\)116;1587:AOTSLM;2.0.CO;2](https://doi.org/10.1175/1520-0493(1988)116;1587:AOTSLM;2.0.CO;2).

Roundy, P. E. and Frank, W. M. (2004). A climatology of waves in the equatorial region. *Journal of the Atmospheric Sciences*, 61(17):2105–2132. [https://doi.org/10.1175/1520-0469\(2004\)061;2105:ACOWIT;2.0.CO;2](https://doi.org/10.1175/1520-0469(2004)061;2105:ACOWIT;2.0.CO;2).

Roundy, P. E., Schreck, C. J., and Janiga, M. A. (2009). Contributions of convectively coupled equatorial Rossby waves and Kelvin waves to the real-time multivariate MJO indices. *Monthly Weather Review*, 137(1):469–478. <https://doi.org/10.1175/2008MWR2595.1>.

Salby, M. L. (1981). The 2-day wave in the middle atmosphere: Observations and theory. *Journal of Geophysical Research: Oceans*, 86:9654–9660. <https://doi.org/10.1029/JC086iC10p09654>.

Salby, M. L. and Garcia, R. R. (1987). Transient response to localized episodic heating in the tropics. Part I: Excitation and short-time near-field behavior. *Journal of the Atmospheric Sciences*, 44(2):458–498.

Sardeshmukh, P. D. and Hoskins, B. J. (1988). The generation of global rotational flow by steady idealized tropical divergence. *Journal of the Atmospheric Sciences*, 45(7):1228–1251. [https://doi.org/10.1175/1520-0469\(1988\)045;1228:TGOGRF;2.0.CO;2](https://doi.org/10.1175/1520-0469(1988)045;1228:TGOGRF;2.0.CO;2).

- Shuckburgh, E., Norton, W., Iwi, A., and Haynes, P. (2001). Influence of the quasi-biennial oscillation on isentropic transport and mixing in the tropics and subtropics. *Journal of Geophysical Research: Atmospheres*, 106(D13):14327–14337. <https://doi.org/10.1029/2000JD900664>.
- Silva Dias, P. L., Schubert, W. H., and DeMaria, M. (1983). Large-Scale Response of the Tropical Atmosphere to Transient Convection. *Journal of the Atmospheric Sciences*, 40:2689–2707. [https://doi.org/10.1175/1520-0469\(1983\)040<2689:LSROTT>2.0.CO;2](https://doi.org/10.1175/1520-0469(1983)040<2689:LSROTT>2.0.CO;2).
- Starx, T. (1976). Wave-CISK and cumulus parameterization. *Journal of the Atmospheric Sciences*, 33(12):2383–2391. [https://doi.org/10.1175/1520-0469\(1976\)033<2383:WCACP>2.0.CO;2](https://doi.org/10.1175/1520-0469(1976)033<2383:WCACP>2.0.CO;2).
- Stephan, C. C., Žagar, N., and Shepherd, T. G. (2021). Waves and coherent flows in the tropical atmosphere: New opportunities, old challenges. *Quarterly Journal of the Royal Meteorological Society*, 147(738):2597–2624. <https://doi.org/10.1002/qj.4109>.
- Stevens, D. E. and Ciesielski, P. E. (1986). Inertial instability of horizontally sheared flow away from the equator. *Journal of the Atmospheric Sciences*, 43(23):2845–2856. [https://doi.org/10.1175/1520-0469\(1986\)043<2845:IIOHSF>2.0.CO;2](https://doi.org/10.1175/1520-0469(1986)043<2845:IIOHSF>2.0.CO;2).
- Suhas, E., Neena, J., and Jiang, X. (2020). Exploring the factors influencing the strength and variability of convectively coupled mixed Rossby–gravity waves. *Journal of Climate*, 33(22):9705–9719. <https://doi.org/10.1175/JCLI-D-20-0218.1>.
- Sweeney, A., Fu, Q., Pahlavan, H. A., and Haynes, P. (2023). Seasonality of the QBO impact on equatorial clouds. *Journal of Geophysical Research: Atmospheres*, 128(7):e2022JD037737. <https://doi.org/10.1029/2022JD037737>.
- Takasuka, D. and Satoh, M. (2020). Dynamical roles of mixed Rossby–gravity waves in driving convective initiation and propagation of the Madden–Julian oscillation: General views. *Journal of the Atmospheric Sciences*, 77(12):4211–4231. <https://doi.org/10.1175/JAS-D-20-0050.1>.
- Takasuka, D., Satoh, M., and Yokoi, S. (2019). Observational evidence of mixed Rossby-gravity waves as a driving force for the MJO convective initiation and propagation. *Geophysical Research Letters*, 46:5546–5555. <https://doi.org/10.1029/2019GL083108>.
- Takayabu, Y. N. (1994). Large-scale cloud disturbances associated with equatorial waves Part I: Spectral features of the cloud disturbances. *Journal of the Meteorological Society of Japan. Ser. II*, 72(3):433–449. [https://doi.org/10.2151/jmsj1965.72.3\\_433](https://doi.org/10.2151/jmsj1965.72.3_433).
- Takayabu, Y. N. and Nitta, T. (1993). 3-5 day-period disturbances coupled with convection over the tropical Pacific Ocean. *Journal of the Meteorological Society of Japan. Ser. II*, 71:221–246. [https://doi.org/10.2151/jmsj1965.71.2\\_221](https://doi.org/10.2151/jmsj1965.71.2_221).
- Vasylkevych, S. and Žagar, N. (2021). A high-accuracy global prognostic model for the simula-

- tion of Rossby and gravity wave dynamics. *Quarterly Journal of the Royal Meteorological Society*, 147(736):1989–2007. <https://doi.org/10.1002/qj.4006>.
- Wallace, J. (1971). Spectral studies of tropospheric wave disturbances in the tropical western Pacific. *Reviews of Geophysics*, 9(3):557–612. <https://doi.org/10.1029/RG009i003p00557>.
- Wallace, J. and Chang, L. (1972). On the application of satellite data on cloud brightness to the study of tropical wave disturbances. *Journal of the Atmospheric Sciences*, 29:1400–1403. [https://doi.org/10.1175/1520-0469\(1972\)029<1400:OTAOSD>2.0.CO;2](https://doi.org/10.1175/1520-0469(1972)029<1400:OTAOSD>2.0.CO;2).
- Wang, B. and Xie, X. (1996). Low-frequency equatorial waves in vertically sheared zonal flow. Part I: Stable waves. *Journal of Atmospheric Sciences*, 53(3):449–467. [https://doi.org/10.1175/1520-0469\(1996\)053<0449:LFEWIV>2.0.CO;2](https://doi.org/10.1175/1520-0469(1996)053<0449:LFEWIV>2.0.CO;2).
- Webster, P. J. (2020a). Climatology of the Tropical Atmosphere and Upper Ocean. In *Dynamics of the tropical atmosphere and oceans*, pages 1–36. John Wiley & Sons, first edition. <https://doi.org/10.1002/9781118648469>.
- Webster, P. J. (2020b). Fundamental processes. In *Dynamics of the tropical atmosphere and oceans*, pages 77–106. John Wiley & Sons, first edition. <https://doi.org/10.1002/9781118648469>.
- Webster, P. J. and Holton, J. R. (1982). Cross-equatorial response to middle-latitude forcing in a zonally varying basic state. *Journal of the Atmospheric Sciences*, 39(4):722–733. [https://doi.org/10.1175/1520-0469\(1982\)039<0722:CERTML>2.0.CO;2](https://doi.org/10.1175/1520-0469(1982)039<0722:CERTML>2.0.CO;2).
- Wheeler, M. and Kiladis, G. N. (1999). Convectively coupled equatorial waves: Analysis of clouds and temperature in the wavenumber–frequency domain. *Journal of the Atmospheric Sciences*, 56:374–399. [https://doi.org/10.1175/1520-0469\(1999\)056<0374:CCEWAO>2.0.CO;2](https://doi.org/10.1175/1520-0469(1999)056<0374:CCEWAO>2.0.CO;2).
- Wheeler, M., Kiladis, G. N., and Webster, P. J. (2000). Large-scale dynamical fields associated with convectively coupled equatorial waves. *Journal of the Atmospheric Sciences*, 57(5):613–640. [https://doi.org/10.1175/1520-0469\(2000\)057<0613:LSDFAW>2.0.CO;2](https://doi.org/10.1175/1520-0469(2000)057<0613:LSDFAW>2.0.CO;2).
- Wilson, J. D. and Mak, M. (1984). Tropical response to lateral forcing with a latitudinally and zonally nonuniform basic state. *Journal of the Atmospheric Sciences*, 41:1187–1201. [10.1175/1520-0469\(1984\)041<1187:TRTLFW>2.0.CO;2](https://doi.org/10.1175/1520-0469(1984)041<1187:TRTLFW>2.0.CO;2).
- Winter, T. and Schmitz, G. (1998). On divergent barotropic and inertial instability in zonal-mean flow profiles. *Journal of the Atmospheric Sciences*, 55(5):758–776. [https://doi.org/10.1175/1520-0469\(1998\)055<0758:ODBAII>2.0.CO;2](https://doi.org/10.1175/1520-0469(1998)055<0758:ODBAII>2.0.CO;2).
- Wong, M. L. (2009). Wavelet analysis of the convectively coupled equatorial waves in the wavenumber–frequency domain. *Journal of the Atmospheric Sciences*, 66(1):209–212.

<https://doi.org/10.1175/2008JAS2839.1>.

Yanai, M. and Hayashi, Y. (1969). Large-scale equatorial waves penetrating from the upper troposphere into the lower stratosphere. *Journal of the Meteorological Society of Japan. Ser. II*, 47:167–182. [https://doi.org/10.2151/jmsj1965.47.3\\_167](https://doi.org/10.2151/jmsj1965.47.3_167).

Yanai, M. and Maruyama, T. (1966). Stratospheric wave disturbances propagating over the equatorial Pacific. *Journal of the Meteorological Society of Japan. Ser. II*, 44:291–294. [https://doi.org/10.2151/jmsj1965.44.5\\_291](https://doi.org/10.2151/jmsj1965.44.5_291).

Yanai, M. and Murakami, M. (1970). A further study of tropical wave disturbances by the use of spectrum analysis. *Journal of the Meteorological Society of Japan. Ser. II*, 48:185–197. [https://doi.org/10.2151/jmsj1965.48.3\\_185](https://doi.org/10.2151/jmsj1965.48.3_185).

Yang, G.-Y., Feng, X., and Hodges, K. (2023). Seasonal and interannual variation of equatorial waves in ERA5 and GloSea5. *Quarterly Journal of the Royal Meteorological Society*, 149(752):1109–1134. <https://doi.org/10.1002/qj.4460>.

Yang, G.-Y., Hoskins, B., and Slingo, J. (2003). Convectively coupled equatorial waves: A new methodology for identifying wave structures in observational data. *Journal of the Atmospheric Sciences*, 60(14):1637–1654. [https://doi.org/10.1175/1520-0469\(2003\)060<1637:CCEWAN>2.0.CO;2](https://doi.org/10.1175/1520-0469(2003)060<1637:CCEWAN>2.0.CO;2).

Yang, G.-Y. and Hoskins, B. J. (2017). The equivalent barotropic structure of waves in the tropical atmosphere in the Western Hemisphere. *Journal of the Atmospheric Sciences*, 74:1689–1704. <https://doi.org/10.1175/JAS-D-16-0267.1>.

Yao, W. and Jablonowski, C. (2015). Idealized quasi-biennial oscillations in an ensemble of dry GCM dynamical cores. *Journal of the Atmospheric Sciences*, 72(6):2201–2226.

Yasui, R., Sato, K., and Miyoshi, Y. (2018). The momentum budget in the stratosphere, mesosphere, and lower thermosphere. Part II: The in situ generation of gravity waves. *Journal of the Atmospheric Sciences*, 75(10):3635–3651. <https://doi.org/10.1175/JAS-D-17-0337.1>.

Yokoyama, C. and Takayabu, Y. N. (2012). Relationships between rain characteristics and environment. Part II: Atmospheric disturbances associated with shallow convection over the eastern tropical Pacific. *Monthly Weather Review*, 140(9):2841–2859. <https://doi.org/10.1175/MWR-D-11-00251.1>.

Žagar, N. (2015). Modal decomposition of ECMWF deterministic forecasts. (accessed: 05.08.2024).

Žagar, N. (2017). A global perspective of the limits of prediction skill of NWP models. *Tellus A: Dynamic Meteorology and Oceanography*, 69(1):1317573.

<https://doi.org/10.1080/16000870.2017.1317573>.

- Žagar, N., Kasahara, A., Terasaki, K., Tribbia, J., and Tanaka, H. (2015). Normal-mode function representation of global 3-D data sets: open-access software for the atmospheric research community. *Geoscientific Model Development*, 8:1169–1195. <https://doi.org/10.5194/gmd-8-1169-2015>.
- Žagar, N., Lunkeit, F., Sielmann, F., and Xiao, W. (2022). Three-Dimensional Structure of the Equatorial Kelvin Wave: Vertical Structure Functions, Equivalent Depths, and Frequency and Wavenumber Spectra. *Journal of Climate*, 35(7):2209–2230. <https://doi.org/10.1175/JCLI-D-21-0342.1>.
- Žagar, N., Neduhal, V., Vasylykevych, S., Zaplotnik, Ž., and Tanaka, H. L. (2023). Decomposition of vertical velocity and its zonal wavenumber kinetic energy spectra in the hydrostatic atmosphere. *Journal of the Atmospheric Sciences*, 80(11):2747–2767. <https://doi.org/10.1175/JAS-D-23-0090.1>.
- Žagar, N., Tribbia, J., Anderson, J., and Raeder, K. (2009). Uncertainties of estimates of inertia-gravity energy in the atmosphere. Part II: Large-scale equatorial waves. *Monthly Weather Review*, 137:3858–3873. <https://doi.org/10.1175/2009MWR2816.1>.
- Zangvil, A. and Yanai, M. (1980). Upper tropospheric waves in the tropics. Part I: Dynamical analysis in the wavenumber-frequency domain. *Journal of the Atmospheric Sciences*, 37:283–298.
- Zhang, C. (1993). Laterally forced equatorial perturbations in a linear model. Part II: Mobile forcing. *Journal of the Atmospheric Sciences*, 50(6):807–821. [https://doi.org/10.1175/1520-0469\(1993\)050<0807:LFEPiA>2.0.CO;2](https://doi.org/10.1175/1520-0469(1993)050<0807:LFEPiA>2.0.CO;2).
- Zhang, C. and Webster, P. J. (1989). Effects of zonal flows on equatorially trapped waves. *Journal of the Atmospheric Sciences*, 46(24):3632–3652. [https://doi.org/10.1175/1520-0469\(1989\)046<3632:EOZFOE>2.0.CO;2](https://doi.org/10.1175/1520-0469(1989)046<3632:EOZFOE>2.0.CO;2).
- Zhang, C. and Webster, P. J. (1992). Laterally forced equatorial perturbations in a linear model. Part I: Stationary transient forcing. *Journal of the Atmospheric Sciences*, 49(7):585–607. [https://doi.org/10.1175/1520-0469\(1992\)049<0585:LFEPiA>2.0.CO;2](https://doi.org/10.1175/1520-0469(1992)049<0585:LFEPiA>2.0.CO;2).
- Zhou, X. and Wang, B. (2007). Transition from an eastern Pacific upper-level mixed Rossby-gravity wave to a western Pacific tropical cyclone. *Geophysical Research Letters*, 34(24). <https://doi.org/10.1029/2007GL031831>.